University College London

The gas sensitive material

$Cr_{(2-x)}\ Ti_{(x)}\ O_3$

by

Dirk Niemeyer

PhD, 2001

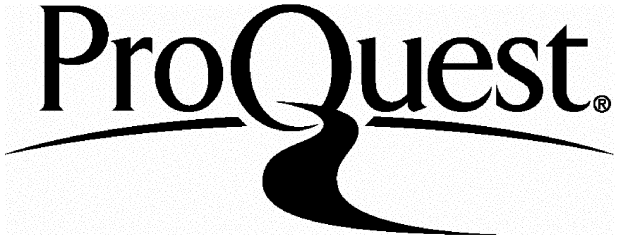

Abstract

Chromium titanium oxide (CTO) is a recently discovered gas sensor material that is capable of detecting small concentrations of toxic or flammable gases in air with stability of performance over the short and long-term and minor influences of variations of humidity. CTO is the first new material to be successfully commercialised in large-volume manufacture for sensing of hydrocarbons, VOCs, hydrogen and carbon monoxide at low (ppm) concentrations in air since the introduction of SnO_2 for this purpose in the 1960s. The main focus of this thesis lies in the systematic investigation of this material in order to develop a detailed theoretical understanding of the gas response mechanism.

CTO was prepared by solid-state reaction of Cr_2O_3 and TiO_2 in air at 1000°C. It crystallises in a solid solution with the general formula $Cr_{2-x}Ti_xO_3$. The phase limit is at $x \simeq 0.3$-0.4. Above the phase limit a 2-phase mixture with $CrTiO_3$ is found. Substitution of Ti strongly decreases the electrical conductivity of the porous bodies studied. This effect, and the surface segregation of Ti, controls the gas sensor behaviour. Atomistic simulations have been performed on the (0001) and $(10\bar{1}2)$ face to assess defect models for pure- and titanium doped Cr_2O_3. In the absence of titanium, one stable defect is a Cr^{VI} - $V_{Cr}^{'''}$ pair, which segregates to the (0001) surface and contributes to the relatively high p-type conductivity shown by finely porous bodies of Cr_2O_3 at elevated temperature; with titanium addition, a stable defect, segregated on both of the investigated surfaces, is the complex $(Ti^{IV})_3V_{Cr}^{'''}$. The proportion of surface Cr^{VI} is decreased.

Surface studies of Cr_2O_3 have been performed extensively in the literature because it adsorbs oxygen and catalyses combustion of hydrocarbons. Whilst Cr_2O_3 shows a good combustion rate of CO to CO_2 but only a small gas response, titanium doped Cr_2O_3 behaves the opposite way. X-ray photoelectron spectroscopy of the chromium $2p_{3/2}$ core states show a multiplet

splitting, proposed to originate from local magnetic moments at the Cr site. A Cr^{VI} state is also detected. Substituting titanium decreases the proportion of surface Cr^{VI} and reduces the splitting of the Cr $2p_{3/2}$ state. A reappearance of the splitting at higher Ti concentrations was observed, speculatively attributed to ordering of the surface structure.

Although currently used solely in oxygen-containing environments CTO can also detect gases in a nitrogen atmosphere. Decreasing oxygen partial pressure caused a large decline in conductivity that is explained by removal of oxygen surface acceptor states. Whilst carbon monoxide and ethanol react with the few remaining acceptor states causing a large gas response, H_2S sulphates the surface. The stable gas response to H_2S is caused by reversible adsorption of H_2S molecules on a Cr^{III} site, forming a new surface trap state.

Replacing titanium in CTO by vanadium, iron, magnesium or manganese resulted in a significantly reduced gas response to carbon monoxide. These elements did not form a solid solution with the Cr_2O_3 lattice. However, if introduced as additional elements in CTO manganese and iron dopants crystallised as $MnCr_2O_4$ and $(Cr_{0.4}Fe_{0.6})_2O_3$ impurity phases and reduced the amount of chromium. A significantly reduced response to water vapour relative to the response to carbon monoxide was observed with these materials.

Table of Contents

Table of Figures

Table of Tables

Table of Abbreviations

VOC	Volatile organic compound
LPG	Liquefied petroleum gas
XRD	X-ray powder diffraction
XPS	X-ray photoelectron spectroscopy
IR	Infra red spectroscopy
FTIR	Fourier transform infra red spectroscopy
LEED	Low energy electron diffraction
TPD	Temperature programmed desorption
EDAX	Energy dispersive analysis of x-rays
eV	Electron volts
mol	Moles
ppm	Parts per million
s	Seconds
K	Degrees Kelvin
°C	Degrees Celsius
σ	Conductivity
σ_0	Conductivity in the absence of gas
R	Resistivity
R_0	Resistivity in the absence of gas
P_{gas}	Partial pressure of a gas
mm	Millimetres (10^{-3} metres)
□m	Micrometres (10^{-6} metres)
nm	Nanometres (10^{-9} metres)
Å	Ångstroms (10^{-10} metres)
pm	Picometres (10^{-12} metres)

Acknowledgements

- ✓ **I like to thank my supervisor David E. Williams for providing and supporting this interesting project.**

- ✓ **Many thanks also to Ben Slater for much advice concerning the computational part of my thesis.**

- ✓ **My sincere gratitude goes to Darren Caruana and Keith Pratt for continuous advice in practical and theoretical matters.**

- ✓ **A big cheers for the support I got from all my friends and colleagues and for the very pleasant working atmosphere in room G15, G16 and G 25**

- ✓ **Last but not least I thank my wife Angela for all her support during the difficult times of my Ph.D.**

- ✓ **This project was sponsored by the Engineering and Physical Science Research Council and Capteur Sensors Ltd.**

1 Introduction

1.1 General introduction

Carbon monoxide is the most commonly encountered poison in our environment. It is formed by incomplete combustion of fossil fuels like coal, charcoal, wood or gasoline. Being inhaled, CO combines with the haemoglobin present in the blood and forms carboxyhaemoglobin (COHb). This stable compound is incapable of transporting oxygen to the vital organs like the heart or the brain. So low levels of CO can slowly starve body tissues and organs of oxygen and lead to death.

Annually, due to CO exposure [1]:

- Tens of thousands of people in the United States seek medical attention or lose several days, weeks, months of normal activity
- More than 500 people die through unintentional exposure
- As many as 2000 people commit suicide using CO

Carbon monoxide is particular dangerous because it has no colour, odour or taste and can therefore not be detected by human beings. Every fuel-burning place in homes is a source of carbon monoxide and therefore causes an important risk to personal safety. As a consequence research has been driven to develop sensor devices that provide a cost effective and reliable way to detect carbon monoxide and to ensure a healthy environment.

1.1.1 Development of solid state gas sensors

Brattain and Bardeen [2] demonstrated about forty years ago that the conductivity of semiconducting oxides could be altered by small concentrations of adsorbed gases. These observations led to the development of zinc oxide as the first solid-state gas sensor. Shortly after, tin dioxide (SnO_2) was discovered to be a gas sensing material and commercialised in the 1960s.[3] Tin dioxide offered a bigger sensitivity than ZnO at a lower operating temperature and easier fabrication into sensor devices. Although able to detect quantitatively amounts of polluting gases in air, sensors based on tin dioxide suffered from poor baseline stability and a large interference of water vapour. As a consequence, research has focussed on developing better sensor materials. A large range of oxides has been studied systematically in order to examine their changes in conductivity in the presence of small traces of gases. These studies revealed that the response to any kind of gas is a common phenomenon for oxides. [8]

From the survey of the gas sensing behaviour of a large range of oxides, titanium-doped chromium oxide (CTO) was discovered as an alternative and commercialised by Capteur Sensors & Analysers Ltd. This gas sensing material detects carbon monoxide and volatile organic compounds (VOCs). A good baseline stability and only small water vapour interference made this compound a real breakthrough in sensor technology. The gas response to several concentrations of carbon monoxide in the presence of various water vapour concentrations is illustrated in Figure 1.1. First one notes that the material shows an increase in resistivity in the presence of carbon monoxide, in contrast to the behaviour of tin dioxide, which shows a decrease. Secondly, it can be observed that the increase in the resistivity caused by the water vapour is very small compared with the gas response to carbon monoxide.

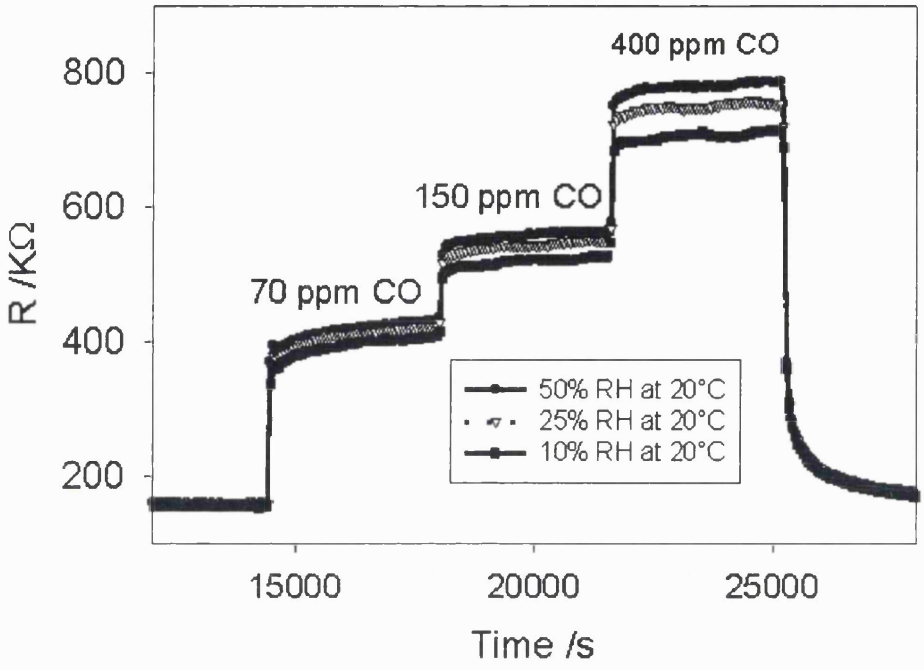

Figure 1.1 Gas response of a CTO sensor device at 400°C

Due to its good stability and low water response the commercial carbon monoxide sensor utilising CTO has been approved by Underwriters Laboratories Inc. (ULI) under the UL 2034 Conformity Assessment. This approval states that the key enabling sensing technology has been fully assessed and tested specifically for use within home safety products and will carry the UL Recognition Mark.[4]

1.1.2 Applications for gas sensors

Resistive adsorption based sensors are a simple and cost effective way to determine gas components in the atmosphere. These gas sensors can be used for characterisation of the atmosphere concerning air quality or potential hazards, and the assessment of air. The aim is often not to quantify gas components in the atmosphere completely but rather to detect and approximate the quantification of a class of gases or gas mixtures present in the air. It is often the case that normal conditions have to be monitored by

measuring any deviation from an acceptable air quality or from the usual ambience of a process. There is a wide range of uses, for example in car heating-system controls or in self–regulating ovens, or to control waste gases by monitoring for harmful compounds or to monitor high–quality air, low in pollution and odours. There are also certain conditions that are crucial for products to be a success on the mass market, such as prices appropriate to the market, a high degree of reliability at little maintenance cost, small dimensions and low energy consumption.

1.1.3 The aim of this research work

The present work is an attempt to enhance the basic scientific understanding of the material chromium titanium oxide and its gas response to carbon monoxide and water. This aim has been achieved by a combination of experimental and surface analysing techniques with modern computational simulations. A review of the standard gas response model and the main analysing techniques is given in the next section. The results obtained have founded the basis of a deeper theoretical understanding and can be used for development of new sensor materials.

1.2 Gas sensor properties

The current consensus [5,6] is that the conductivity of porous bodies of semiconducting oxides in air is determined by the trapping of electrons in surface states associated with adsorbed oxygen. If oxygen vacancies or interstitials are immobile in the lattice, then the behaviour is described entirely in terms of the distribution of the electrons between surface and bulk states. At elevated temperatures (200-600°C) the conductivity is sensitive to the presence of trace reactive gases because catalytic surface processes result in a kinetically determined change in the surface coverage of the oxygen surface trap states. If oxygen defects are sufficiently mobile in the lattice, then the conductivity is simply determined by the equilibrium between bulk lattice defects and oxygen in the gas phase, and the sensitivity to trace reactive gases is lost. In intermediate cases, a conductivity sensitive to the presence of trace reactive gases but varying in time as the lattice defects equilibrate is observed.

Time-variation of conductivity can also be caused by migration of metal or oxygen defects, which change the potential and hence charge carrier distribution near the surface. The sensitivity to gases, and the time dependence of response, is further modified in a porous body because this behaves as a complex network in which part of the conductivity, that modified by the surface interaction, is gas sensitive, whilst another part, that contributed by the 'bulk' sufficiently far from any surface, is not gas sensitive[7]. Several models concerning the influence of microstructure on the gas response have been proposed. Three different cases are distinguished from another according to the relative magnitude of the crystallite size (D) and the thickness of the space charge layer (2L) [5]

$D > 2L$ (grain boundary control). These conditions happen in a well-sintered material. The depletion layer is restricted to the surface region and the grains are connected via wide necks. The conductivity is controlled by activation of electrons from bulk donor states. The gaseous atmosphere would only affect

the conductivity by substantially narrowing the electron channel inside the necks.

D □ 2L (neck control). A less well-sintered material consists of depletion zones which are larger in comparison to the crystal size and which therefore overlap. The grains are connected by narrower necks with a higher resistance through the centre. The conductivity is determined by activation of electrons from surface states and would therefore directly be affected by changes of surface states due to the influence of the gaseous atmosphere.

D < 2L (grain control). In porous bodies with very short and narrow necks the space charge region is extended over each particle. Schottky barriers are formed at the contact points between the grains. Charge transport through the barrier controls the conductivity.

The effects have a substantial impact on the gas sensing behaviour of the material. Such effects complicate the interpretation of data obtained on porous artifacts. Despite such complications, Williams and Moseley [8] showed that there was a general framework within which the behaviour of semiconducting oxides as reactive gas sensors could be understood. Oxygen species act as surface acceptors; if the bulk oxide is n-type then a decrease in the surface acceptor density increases the conductivity whereas if the bulk material is p-type then a decrease in the oxygen surface acceptor density decreases the conductivity. Behaviour which changed from apparently p-type to n-type with change of gas concentration or temperature could be easily rationalised using this model. The first report of CTO as a p-type sensor material for reactive gases was made by Moseley and Williams [9], who claimed that it was selective to ammonia in air. Subsequently, the properties of CTO as a sensor material for H_2S in air were described by Dawson *et. al.* [10] and by Henshaw *et. al.* [45]. A surface conditioning caused by sulphation and hydroxylation of surface sites was demonstrated, and a model for the sensor action based on reaction of surface oxygen species (O_{ads}^-) to form surface sulphate was developed.

Williams and Pratt [7] described in outline the response of CTO to CO, acetone and toluene in air, and to ethanol, and assumed a response mechanism involving reaction of the target gas with doubly occupied oxygen surface states (O^{2-}_{ads}), by analogy to the mechanisms proposed for the response of SnO_2.[4] Jayaraman *et. al.* [46] reported responses to NH_3, H_2 and LPG, showing a response to ammonia increasing with increasing mole fraction of TiO_2, to a maximum at approximately $Cr_{1.8}Ti_{0.2}O_3$. Sensors based on this material have been introduced commercially for detection of carbon monoxide in air, and for hydrocarbons and VOCs [4].

1.3 Organisation of the thesis

A description of the experimental and surface analytical techniques that have been used in this thesis is given in **Chapter 2**. It involves the preparation of the specimen, the analysis of these samples via XRD and XPS techniques and the conductivity and gas response measurements. **Chapter 3** gives an introduction into the computational simulation techniques that have been used in this thesis. **Chapter 4** is the first result chapter. It describes the two mainly exposed surfaces in Cr_2O_3 and sets up a defect model for the plain and the titanium doped Cr_2O_3. The stability of these defects on the surfaces is assessed by computational modelling and fitted into a general model, which rationalises the gas response to carbon monoxide.

Chapter 5 focuses on the systematic experimental investigation of CTO. A phase diagram is produced and the electrical and gas sensing behaviour of the different $Cr_{2-x}Ti_xO_3$ samples is presented. Surface analysis of the CTO samples via XPS is reported in **Chapter 6**. Two main areas are investigated, firstly the surface segregation of titanium and secondly the nature of the Cr $2p_{3/2}$ peak. Gas sensing experiments of CTO in a nitrogen atmosphere have been carried out in **Chapter 7**. The first part deals with the H_2S response of CTO in a nitrogen atmosphere, whilst the second part focuses on the variation of the gas response with varying oxygen partial pressure. CO and ethanol have been used

as target gases. **Chapter 8** explains the electrical and gas-sensing effects of Cr_2O_3 doped with metal cations adjacent to chromium and titanium, whilst **Chapter 9** investigate the iron and manganese doped CTO. A summary and conclusion of the thesis is given in **Chapter 10** and the references are listed in **Chapter 11.**

2 Experimental methods

2.1 Preparation of the specimen

Materials were prepared by solid-state reaction of Cr_2O_3 and TiO_2. Preliminary work showed that the degree of reaction was sensitively dependent on the particle size and mixing of the two powders, an effect that probably explains the discrepancies in the literature. It has been shown by Shukri[11] that with sufficiently small particles sufficiently well dispersed (for example by mixing colloidal dispersions of $Cr(OH)_3$ and TiO_2, drying and firing), complete reaction can be obtained in relatively short time at relatively low temperature. A convenient procedure is the following. Cr_2O_3 in the form of a fine powder with typical particle size 50nm was prepared by careful thermal decomposition in air of ammonium dichromate contained in a large flask fitted with air condenser and dust trap (*DANGER: EXPLOSION HAZARD*). *The temperature should be raised slowly to the ignition point, then the heating ceased. The amount of material decomposed at any one time should be limited).* The powder was dispersed in propan-2-ol, typically 20 gram of powder and 500 cm^3 propan-2-ol and the required amount of titanium propan-2-oxide solution in propan-2-ol was added under ultrasonic agitation, typically 15 cm^3 titanium propan-2-oxide in 100 cm^3 propan-2-ol. After five minutes 5 cm^3 of water was added. After stirring under ultrasonic agitation for another 15 minutes the solvent was evaporated using a rotary evaporator with continuing application of ultrasound throughout the evaporation in order to maintain intimate mixing of the two components. The powder was dried at 120°C for two hours. Subsequently the powder was fired in recrystallised alumina crucibles for twelve hours at 1000°C. The preparation to form a solid solution can be represented by the equation

$$\left(1-\frac{2x}{3}\right)Cr_2O_3 + xTiO_2 \rightarrow Cr_{2\left(1-\frac{2x}{3}\right)}Ti_xO_3 \qquad (2.1)$$

The preparation was performed by mixing x moles of TiO_2 with (1-x/2) moles Cr_2O_3 and so the balanced equation for the reaction is

$$\left(1-\frac{x}{2}\right)Cr_2O_3 + xTiO_2 \rightarrow Cr_{2-x}Ti_xO_{3+\frac{x}{2}} \qquad (2.2)$$

The representation of this component as $Cr_{2-x}Ti_xO_3$ is a convenient approximation.

2.2 X – ray photoelectron spectroscopy (XPS)

X – ray photoelectron spectroscopy is a very powerful technique and was used extensively in this thesis. It provided information about the surface composition of the doped Cr_2O_3 materials. With the help of this technique, the ions and their charge states on the surface have been identified. Quantification of the peaks gave information about the concentration of the particular ion on the surface. The valence band structure has been also investigated. A detailed description about XPS technology and interpretation of the spectra can be found in the literature. [12] XPS spectra were recorded (VG ESCALAB 220iXL instrument) using focused (300 μm spot size) monochromatized Al Kα radiation. The binding energies were referenced to the oxygen 1s peak at 531.0 eV binding energy and the sample charging was controlled with a 3 eV flood gun. Spectrum quantification was performed using a Shirley background and sensitivity factors were obtained from Wagner *et. al.* [13].

XPS measurements involve the ejection of electrons from the surface atoms, leaving them with a positive charge. This charging can lead to peak broadening and has to be minimised during the measurements. In order to do that the specimen to be investigated was pressed into a very thin pellet and mounted onto an aluminium tray with doublesided carbon tape. Then the sample was covered with a silver foil, leaving a small hole over the analysis area. Recalibration of the XPS machine was performed regularly in order to eliminate any peak drift.

2.3 X – ray powder diffraction XRD

X – ray powder diffraction analysis was used to study the phase system of the prepared chromium titanium oxide powders and to evaluate the influence of cation substitution. This technique was used because it provides information about changes in the bulk structure caused by lattice defects. The results obtained from these investigations were used to set up a phase diagram. Apart from the Cr_2O_3 phase structure, XRD provided information about the lattice parameters, and the average crystallite size.

The sample was prepared by grinding about 20 milligrams of powder using a mortar and pestle. The powder was then applied between two pieces of amorphous Scotch tape and inserted into a Siemens D 5000 XRD machine. The instrument used an incident beam monochromator and operated in transmission mode. In order to get a good spectrum a step time of 12 s and a step size of 0.02° were chosen. The scan was done from 2Θ = 20°-73°. The duration of one run was eight hours and fifty minutes.

The average crystallite size was determined by additional X-ray line broadening. This phenomenon occurs when the crystallite size is roughly below 200 nm. Line broadening can only give an estimate of the crystallite size, since the Kα line has an intrinsic breadth. The Scherrer formula was used to calculate the average crystallite size D.

$$D = 0.9 \lambda / B \cos \theta_B \quad (2.3)$$

where D is the thickness of the crystal in Å, λ is the x ray wavelength θ_B is the Bragg angle and B is the line width in degrees at half peak maximum

2.4 Conductivity and gas response measurements

About 1 g of chromium titanium oxide powder was pressed into pellets with about 2 mm thickness and 13 mm diameter. Those pellets were examined with a computer-controlled rig. (Fig. 2.1)

The rig consisted of a long quartz gas tube with a thermocouple and a ceramic sample holder for up to four samples. Each sample was fitted between two gold electrodes. Alumina spacers divided the gold electrodes.
The quartz tube was fitted into a tube furnace (Carbolite MTF 12/38a) to heat the pellets. The resistance changes of the pellets and the thermocouple voltages were recorded every 120 seconds by a Keithley 175A autoranging multimeter and fed into a computer, which recorded the data separately for each of the four samples. The computer also controlled the furnace temperature and the amount of gas flowing through the glass tube via mass flow controllers and solenoid valves. The gas response of the samples was described as:

$$S = R/R_0 \quad (2.4)$$

One gram of powder was pressed at one tonne pressure into a pellet of 13 mm diameter and 1.5–2 mm thickness, which was sintered before measurement at

1000°C for twelve hours. It is noted that the electric properties of pressed powders are influenced by many variables, including the number and area of intergranular contacts, which control the conduction path. Therefore every single pellet behaves differently and the obtained results are not strictly reproducible. Temperature gradients inside the furnace and small variations of the gas flow are also a source of errors. All obtained results were compared against a standard pellet of $Cr_{1.8}Ti_{0.2}O_3$, which was present in each run.

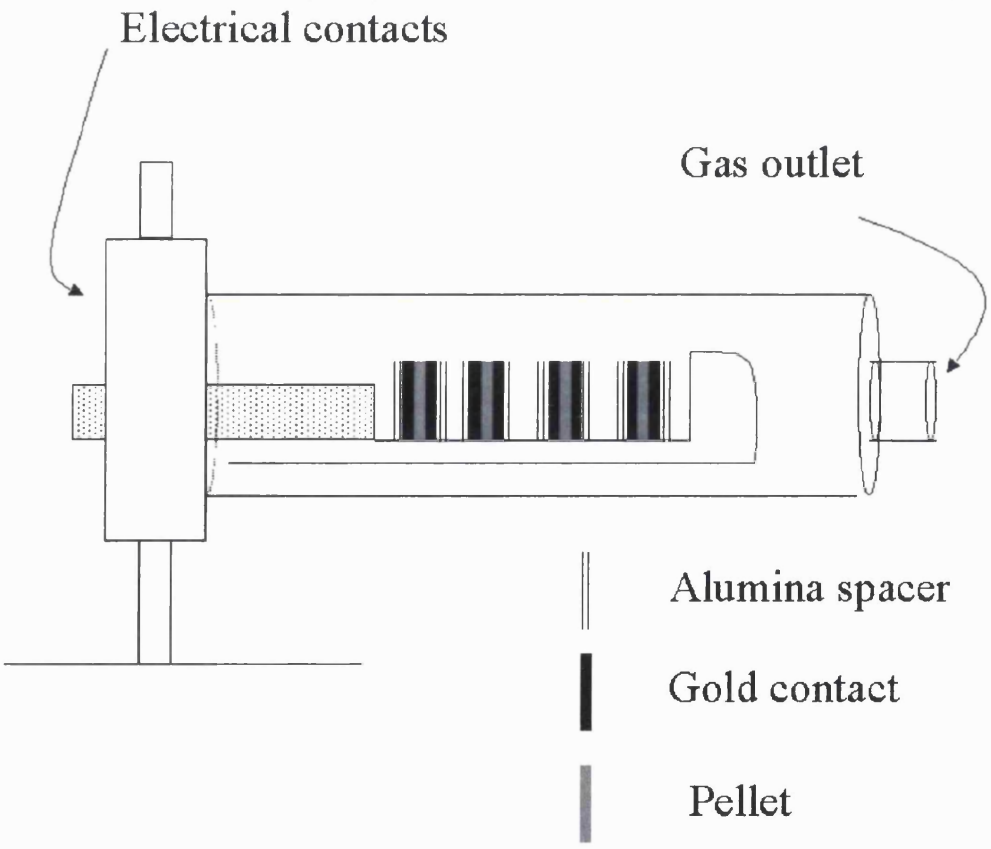

Figure 2.1 Pellet rig

3 Computational simulations

3.1 Why computational chemistry?

In recent years computational simulations have become a major tool for exploring surfaces and interfaces. These very powerful new methods are able to provide information about the most stable atomic configuration at the surface. Defect calculations deliver information about surface irregularities such as point defects, steps, adsorption or surface segregation of bulk defects.

Static lattice simulations have been chosen for this thesis because they are a common way of carrying out calculations on all kinds of crystals and surfaces. They are based on the use of interatomic potentials, which have either been derived *ab initio* or empirically by fitting to bulk elastic or dielectric properties. These potentials subsume knowledge of atomic structure into a numerical or analytical function describing the variation of the total energy of the system with the positions of the nuclei. The goal of these calculations is to predict the most stable structure by finding the atomic configuration in which the total energy is at a minimum.

Results that have been obtained in this way have proven to be consistent with many different computational models.[14] Accordingly using pair potentials can simulate the short-range interactions of atoms very effectively. The long-range Coulomb interactions over two-dimensional periodic structures can be summated in a very general way that is computationally efficient. For that purpose the Ewald method has been modified for two-dimensional systems. [15],[16]. Dipolar electronic effects are described by the shell model, in which the ion core is connected via a spring to a massless shell.[17] These methods are capable of reproducing the bulk properties of defect crystals such as the lattice

parameters, and bulk defect energies. Calculations of bulk properties in this thesis have been carried out with the GULP code.[18]

Recent advances have led to the development of sophisticated software codes for computation of surface energies that require only a crystal structure and a specified surface. MARVINS Program [19] was used in this thesis.

3.2 MARVINS Program

MARVINS stands for (**M***inimisation* **A***nd* **R***elaxation of* **V***acancies and* **I***nterstitials at* **S***urfaces*). As is common for surface simulations the simulation cell used by MARVINS consists of a stack of planes which is infinitely repeated in x and y directions but finite in the z direction (two dimensional periodic boundary conditions). This cell is divided into two regions. Region I symbolises the surface region. Defects are placed in this region. During the calculation, the ions of region I are relaxed to equilibrium. Region II simulates the bulk lattice adjacent to region I. All atoms in region II are kept fixed.

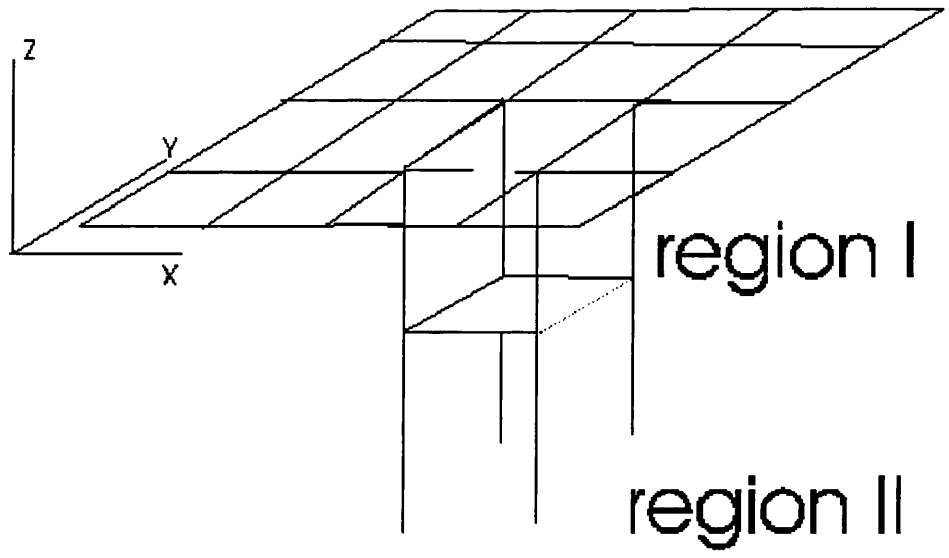

Figure 3.1 Schematic of the MARVINS simulation cell.

3.3 Total energy

The total energy is the sum over all short and long range interactions of the entire region I structural units interacting with themselves, all the region II structural units and the periodic images of both regions. The total energy is the most important quantity that MARVINS calculates and that is minimised in order to get the most stable surface configuration. In defect calculations the gradient of the total energy provides essential information about the most favourable configuration of the defect.

3.4 How is the total energy derived?

The total energy consists of different terms that depend upon the number of atoms that determine the interaction. The energy E_a for every atom is expressed as

$$E_a = \tfrac{1}{2}\sum_b U_{ab}^{(2)} + \tfrac{1}{3}\sum_{bc} U_{abc}^{(3)} + \tfrac{1}{4}\sum_{bcd} U_{abcd}^{(4)} \ldots + \text{higher order terms} \quad (3.1)$$

where $U_{ab\ldots}^{(N)}$ is the interaction energy of order (N) between the atoms and a b c d are indexing all atoms in the system. Double counting of the atoms is avoided by the fraction before each summation. The sum of all E_a's is the total energy. Considering only two body interactions the energy of each atom in region I is given by

$$E_a^{(2D)} = \tfrac{1}{2}\sum_{b}^{N_{all}}\sum_{l} U_{ab}^{(2)}\left(r_a - r_b + l\right) \quad (3.2)$$

The sum over all 2 dimensional lattice vectors is expressed by l and N_{all} stands for the sum over all of the other atoms in the cell. This equation expresses that the two body potentials depend only upon the magnitude of the atom a b separation. The total energy for all region I atoms is

$$E_{total} = \sum_{a}^{N_I} E_a = \tfrac{1}{2}\sum_{l}\sum_{a}^{N_I}\left[U_{aa}^{(2)}\left(l_{l\neq 0}\right) + \sum_{b\neq a}^{N_{all}} U_{ab}^{(2)}\left(r_{ab} + l\right)\right] \quad (3.3)$$

where r_{ab} simply means r_a - r_b and $l_{(l\neq 0)}$ means that l=0 is not included in the sum. This equation expresses the interaction of each atom a with its periodic images ($U_{aa}^{(2)}$) and with a periodic plane of atoms b. The second part of the equation can be split in two parts to express the summation over all region I atoms and all region II atoms.

$$\tfrac{1}{2}\sum_{b\neq a}^{N_{all}} U_{ab}^{(2)}\left(r_{ab} + l\right) = \sum_{b>a}^{N_{1l}} U_{ab}^{(2)}\left(r_{ab} + l\right) + \tfrac{1}{2}\sum_{b}^{N_2} U_{ab}^{(2)}\left(r_{ab} + l\right) \quad (3.4)$$

The last term in the sum is the boundary interaction energy.

$$E_{boundary} = \tfrac{1}{2}\sum_{l}\sum_{a}^{N_1}\sum_{b}^{N_2} U_{ab}^{(2)}\left(r_{ab} + l\right) \quad (3.5)$$

The largest contribution to the energy is electrostatic. The long-range interaction is accounted for by using a two-dimensional Ewald sum.

$$E_{Madelung} = \tfrac{1}{2}\sum_{a}^{N_1}\sum_{b}^{N_{all}} q_a q_b U_{ab}^{Madelung} \quad (3.6)$$

with $U_{ab}^{Madelung} = U_{ab}^{reciprocal} + U_{ab}^{real}$ (3.7)

Heyes[19] has demonstrated that

$$U_{ab}^{real} = \sum_{1} erfc(G|r_{ab} + l|)/|r_{ab} + l| \quad (3.8)$$

and

$$U_{ab}^{reciprocal} = \pi / A\{-2z_{ab} erf(Gz_{ab}) - 2\exp(-Gz_{ab}^2)/\pi^{1/2}G + \sum_{k\neq 0} \exp(ik.r_{ab})/|k|[\exp(|k|z_{ab})erfc(|k|/2G + Gz_{ab}) + \exp(-|k|z_{ab})erfc(|k|/2G - Gz_{ab})]\} \quad (3.9)$$

where z_{ab} is the vertical separation between the ions a and b perpendicular to the surface, k are the 2D reciprocal lattice vectors and A is the surface area of the simulation cell. The Gaussian weighting factor G determines how the sum is divided between real and reciprocal space and was chosen to minimise the number of terms in the sum.

$$G = (\pi / A)^{1/2} \quad (3.10)$$

These expressions can be directly incorporated into the equation describing the total energy to produce the total coulombic energy with one small correction. The reciprocal sum for an ion interacting with its own images will include a self-interaction term, which is removed by subtracting $2^{1/2}$/AG for each region I particle.

A fully ionic model is used for the potentials of most oxides and halides. The effect of the ionic polarisability is modelled by the shell model of Dick and Overhauser, [19] in which an ion is modelled by a massive core that is connected to a mass less shell via an isotropic harmonic spring restoring force. The full

charge of the ion is divided between the core and the shell. The electronic polarisability α is given by

$$\alpha = \frac{Y^2}{k} \qquad (3.11)$$

where k is the spring constant Y is the ionic charge.

All short-range potentials are acting between the different ion shells. Shell model calculations are based on an ionic crystal model assuming formal ionic charges and dominating pairwise interionic potentials. They are given as long-range Coulomb interactions and short-range potentials. The Buckingham formula was used for the short-range interactions.

$$V_{ab} = A\exp\left(\frac{-r_{ab}}{\rho}\right) - Cr_{ab}^{-6} \qquad (3.12)$$

with the Buckingham parameters A, ρ and C. V_{ab} is the Buckingham potential and r_{ab} is the distance between atom a and b.

3.5 How is this total energy minimised?

Three types of minimiser [20] are currently available in the MARVINS code.

- The downhill Simplex method is efficient at a distance far from the minimum; however, it is very inefficient near the minimum. For this type of minimiser, only function evaluations are required.

- The conjugate gradient method is very efficient at moderate to close distances to the minimum. Unfortunately this method shows difficulties at very close distance to the energy minimum. It uses energy and first derivative evaluations.

- The hybrid Newton minimiser provides great efficiency in close vicinity to the energy minimum but proves to be inefficient at far distances. This method incorporates the second derivative as well.

3.6 Recent work

B. Slater *et. al* [21] used the MARVINS code to carry out bulk and surface calculations on the behaviour of Sb^{III} and Sb^{V} ions substituted in tin dioxide. The (001) and (110) faces were examined. In the absence of any dopant a Sn^{II} /oxygen vacancy defect pair was predicted to be stable on the surface. Sb^{III}/Sb^{V} defect pairs were predicted to be highly surface segregated. Sb^{III} was predicted to be associated with in-plane surface oxygen species, while Sb^{V} was predicted to be subsumed below bridging oxygen ions in a more bulk-like environment. The most significant driving forces for surface segregation were found to be for Sb^{III} and Sn^{II}.

R.W. Grimes[37] used atomistic simulation methods to investigate the solution of TiO_2 in Al_2O_3, which is isostructural to Cr_2O_3. Ti^{IV} defects were charge compensated either by an O^{-II} ion on an interstitial position or by Al vacancies. Assuming clustering of defects a solution energy of 2.31 eV/cation was calculated for the O_i compensation, whilst 1.20 eV/cation was calculated for the V_{Al} compensation. These energies show that aluminium vacancy compensation is much preferred over the oxygen interstitial mode.

4 Computational studies of the chromium oxide surface: analysis of defects and interpretation of the Mars-van Krevelen mechanism for redox catalysis and gas response

4.1 Introduction

The objective of this chapter is to establish a defect model for both the undoped and the titanium doped Cr_2O_3 surface and then to use these models as a basis of interpretation of the catalytic activity of Cr_2O_3. Atomistic simulations are used to predict the defect energies and site occupancies of those defect states throughout the host lattice.

Chromium oxide catalysts have always attracted much interest and are now used in a variety of hydrocarbon reactions such as dehydrogenation and dehydration of alcohols or the methanol synthesis [22]. Surface investigations and oxygen adsorption experiments have been performed extensively during the last decades in order to get a deeper understanding about the reaction mechanism on a molecular scale. Burwell *et. al.* [22] introduced the notion of the coordinatively unsaturated site to account for a gain in catalytic activity of Cr_2O_3 on heating. They identified these sites as exposed Cr^{III} surface atoms. Activation of the catalyst is achieved by removal of water molecules. Consequently adsorption of reactant gases (especially oxygen) increases rapidly. Zecchina *et. al.* [23] performed infrared experiments and reported a dissociative oxygen chemisorption on the Cr_2O_3 surface at room temperature, leading to Cr=O double bonds. Formation of chromates and polychromates

was observed at 400°C. The existence of these higher oxidised chromium states was confirmed by chemical analysis, X ray photoelectron spectroscopy (XPS) and Raman spectroscopy[24,25] .The properties of the Cr_2O_3 are often improved by other materials, acting either as support or as dopant. Callister *et. al.* [26] studied the influence of TiO_2 additives and reported an enhanced sintering. They suggested that the cause of this enhancement lay in suppression of the formation of volatile chromium ions such as Cr^{VI}.

A generally accepted mechanism for redox catalysis on metal oxides, applicable to chromium oxide, is that of Mars and Van Krevelen[27] (M-vK)

$$M_{surf} + CO \rightarrow [M{:}CO]_{surf}$$
$$[M{:}CO]_{surf} + O_{latt,\,surf} \rightarrow M_{surf} + V_{O,\,surf} + CO_2 \qquad (4.1)$$
$$V_{O,surf} + (1/2)O_2 \rightarrow O_{latt,surf}$$

Over *et. al.*[28] provided an atomic-scale verification of the mechanism for CO oxidation on RuO_2. Vedrine *et. al.* [29] pointed out that the M-vK mechanism required sites having both redox and acid-base properties, particularly if hydrogen abstraction or oxygen insertion formed part of the reaction. They introduced the idea of a surface ensemble of ions constituting the active site, of particular structure: an inorganic molecular complex of a particular arrangement to promote a particular reaction. The element of the reaction which involves the dissociation of molecular oxygen has recently been explored in a computational study of the SnO_2 surface.[30] This work showed that oxygen gas will dissociate at a bridging oxygen vacancy on the oxide surface, with one atom filling the vacancy and the other being adsorbed onto a coordinatively unsaturated (5-fold coordinated) adjacent surface Sn[30]. Zaki *et. al.*[31] showed that CO oxidation on Cr_2O_3 commences at a temperature as low as 120°C and 100% conversion is achieved at near 220°C. They showed that this good combustion rate is achieved by surface chromate species Cr^{VI} and the main reaction site to be Cr^{VI}-Cr^{III}. A detailed reaction scheme was not proposed.

4.2 Cr_2O_3 surfaces

4.2.1 General

α Cr_2O_3 is a semiconductor with a band gap of 3.4 eV. Like Al_2O_3 it crystallises in the corundum structure, in which the oxygen atoms are hexagonal closed packed. The Cr^{III} cations are octahedrally coordinated by oxygen ions and one third of the possible cation sites are vacant. Zecchina *et. al.* [23] performed IR investigations of α Cr_2O_3 that they prepared by decomposition of ammonium dichromate. They identified the (0001) face as the main exposed face at which the major reactions like oxygen, water or carbon monoxide adsorption take place. Twenty-three years later Zecchina *et. al.* [32] now assigned the $(10\bar{1}2)$ face as the predominant phase in α Cr_2O_3, using FTIR spectroscopy and high-resolution electron microscopy.

Lawrence and Parker [36] used atomistic lattice simulation techniques to calculate the surface energies for several planes of Cr_2O_3, displayed in Table 4.1. The (0001) face had the lowest surface energy after relaxation. The $(10\bar{1}2)$ surface energy is found to be low before and after relaxation. From that Lawrence and Parker deduced that the latter face is most likely to be experimentally observed.

Table 4.1 Perfect surface energies calculated by Lawence and Parker [36]

Surface	Unrelaxed energy ($J*m^{-2}$)	Relaxed energy ($J*m^{-2}$)
0001	4.59	1.61
$10\bar{1}0$	5.05	2.10
$11\bar{2}0$	3.42	1.90
$11\bar{1}0$	4.34	2.05
$10\bar{1}2$	2.77	1.70

4.2.2 (0001) face

The (0001) basal plane is the most commonly investigated surface of Cr_2O_3 (see Figure 4.1 and 4.2). A good review is given by Freund.[33] It is a polar surface of corundum structure. (0001) Cr_2O_3 films have been prepared by careful oxidation of Cr (110). Adsorption experiments revealed that oxygen was molecularly adsorbed at 90 K. A wide band in the infrared spectra indicated the presence of several different adsorbed O_2 species. At 415 K oxygen dissociation takes place resulting in the formation of chromyl groups with Cr=O double bonds. Experiments with isotope labelled $^{18}O_2$ revealed that no exchange of oxygen atoms with the lattice occurred in the stage of molecular oxygen adsorption. O_2 dissociation and the formation of chromyl groups resulted in an exchange with lattice oxygen. Freund [33] concluded that the oxygen adsorption changes the electronic structure of the molecule. Photoelectron experiments confirmed that these changes arise from charge transfer from the surface to the molecule. [34]

4.2.3 $(10\bar{1}2)$face

The $(10\bar{1}2)$ surface is non-polar and has been found by Zecchina *et. al.*[32] to be the predominantly exposed surface in α Cr_2O_3. (See Figure 4.7 and 4.8) All O^{2-} ions in the top layer are three coordinate and the Cr^{III} cations contained in the second atomic layer are five coordinate, so both ions have one degree of coordinative unsaturation relative to their bulk counterparts. Cox *et. al.*[35] performed LEED experiments on the ion bombarded and annealed surface. They discovered that the most stable configuration is a simple bulk termination, which corresponds with calculations that predict a low surface relaxation. Just as for the (0001) surface, IR investigations show dissociative oxygen adsorption at elevated temperatures, leading to formation of chromyl groups. Cox *et. al.*[35] estimated full coverage of the surface Cr atoms with oxygen leading to Cr at the surface in formal oxidation state (V). Molecular oxygen is adsorbed on top of these species.

4.3 Computational models and results.

4.3.1 Simulations of the Cr_2O_3 corundum structure

The Cr_2O_3 (0001) plane consists of buckled layers of chromium between flat layers of oxygen atoms. Electrostatic stability is achieved by cutting the stack between the buckled metal ion layer, so that only half of the number of atoms is left on each surface created. The surface was simulated by using the MARVINS code developed D.H Gay and A. Rohl in 1995 [14] (see section 3.1.2). The Buckingham formula was chosen to represent the short-range interactions. The potentials for chromium oxide have been derived by Lawrence and Parker[36], the potentials for the titanium impurity have been taken from R.W. Grimes.[37]

The potentials were tested by carrying out a bulk constant pressure relaxation prior to the surface simulations. This was done by using the GULP code [38]. The potentials have been able to reproduce the lattice parameters (Table 4.1) quite accurately. After that GULP was used to calculate bulk defect energies for isolated defects (Table 4.5), which were then summed together in Table 4.6.

Table 4.2 Potential parameters chosen for use by MARVINS

Chromium charge	+2.03	Shell Charge	+0.97
		Spring constant $\left[\frac{eV}{A^2}\right]$	100
Titanium charge	+4.00	Shell Charge	0
		Spring constant $\left[\frac{eV}{A^2}\right]$	
Oxygen Charge	+0.18	Shell Charge	-2.18
		Spring constant $\left[\frac{eV}{A^2}\right]$	27.29

The Buckingham Formula was used for the short-range interaction

$$V_{ab} = A\exp\left(\frac{-r_{ab}}{\rho}\right) - Cr_{ab}^{-6} \qquad (4.2)$$

with the Buckingham parameters A, ρ and C. V_{ab} is the Buckingham potential and r_{ab} is the distance between atom a and b.

Table 4.3 Buckingham parameters chosen for use by MARVINS

Interaction	A (eV)	ρ (Å)	C (eV*Å^6)
O^{-II} - Cr^{III}	1734.1	0.301	0
O^{-II} – Cr^{VI}	985.8	0.301	0
O^{-II} – O^{-II}	22764.3	0.149	27.88
O^{-II} – Ti^{IV}	2549.4	0.299	0

Table 4.4 Structural parameters of Cr_2O_3

	Literature [39]	Calculated	Diff (%)
Space group	R-3c	R-3c	
Lattice constant (Å)			
a	4.952	5.024	1.45
c	13.598	13.101	-3.10
Unit cell volume (Å ^{3})	288.71	286.430	0.7

Table 4.3 shows the computed structural parameters. The close agreement between theory and experiment for the lattice parameters and unit cell size is taken as evidence for the reliability of the interatomic potentials used.

4.3.2 Defect models for Cr_2O_3

The postulate offered is that the water vapour removal needed to activate Cr_2O_3 leaves exposed Cr atoms on the surface, which are coordinatively unsaturated [22]. Cr^{VI} states are formed as a consequence [31], acting as acceptor states. These states remove electrons out of the valence band and cause the p-type conduction of the plain Cr_2O_3. The Cr^{VI} states are charge balanced by chromium vacancies. According to this model Cr^{VI} should be restricted to the surface region, in fact, it has never been regarded as existing in the bulk lattice.

$$Cr_2O_3 \rightarrow Cr^{3+}_{2-2x}Cr^{6+}_{x}O_3 \quad (4.3)$$

This was the first model calculated. The second model was set up to describe the case of titanium doped Cr_2O_3. Ti^{IV} states are created on the surface. They are charge balanced by chromium vacancies. This mechanism is also proposed by Holt and Kofstad [48]

$$\left[1-\frac{2x}{3}\right]Cr_2O_3 + xTiO_2 \rightarrow Cr_{2\left(1-\frac{2x}{3}\right)}Ti_xO_3 \qquad (4.4)$$

4.3.3 (0001) face

The stability of lattice defects was explored computationally, both for bulk defects and for defects approaching the (0001) surface. Since the largest term in the lattice energy is the electrostatic term, the most stable defect in

$Cr_{2-x}Ti_xO_3$ was a cluster of three Ti^{IV} in an equilateral triangle surrounding a Cr vacancy (Fig.4.5/4.6). The most stable position of this cluster was near the surface. Defect formation energies relative to the perfect crystal are given in Table 4.6. The segregation energy for this cluster was large. In the surface-segregated defect cluster, oxygen anions surrounding the chromium vacancy relaxed away from the vacancy and moved up slightly out of the surface. If the Ti cations were placed on the surface, then in the relaxed structure they also moved out of the surface slightly - again, this is an electrostatic effect due to the image forces. The defect pair Cr^{VI}-$V_{CR}^{///}$ in pure Cr_2O_3 was also explored. Again, the most stable state was an associated pair segregated to the surface. The defect formation energies and segregation energies are also given in Table 4.6. There was a significant distortion of the surface oxygen configuration: the oxygen ions clustered closely around the Cr^{VI} and relaxed away from the chromium vacancy. There was an optimum distance apart for the chromium vacancy and the Cr^{VI}: approximately 5 Å. The optimised surface configuration for this cluster is illustrated in Figure 4.3/4.4.

4.3.4 $(10\bar{1}2)$ face

The same defects have been also exposed at the $(10\bar{1}2)$ face (Fig.4.7, 4.8) The 3 Ti^{IV}/V_{Cr} showed surface segregation as well, however, the calculation did not converge when the defect was put on top of the surface. This particular total energy listed in Table 4.6 was calculated with the defects one layer below the surface. This problem illustrates the major difficulty with calculations such as these, which is that of choosing appropriate potentials. The Cr^{VI}/V_{Cr} defect was found to be unstable. No distortion of the lattice was observed in either calculation.

Table 4.5 Bulk defect energies for the isolated defects, calculated by GULP

Isolated defect	Bulk defect energy [eV]
Ti^{IV}	-33.40
V_{Cr}	+55.19
V_O	+25.98
Cr^{VI}	-234.07

Table 4.6 Defect formation energies

Face	Cluster	Bulk defect Energy [eV]	Surface defect Energy [eV]	Segregation Energy [eV]
0001	$3\ Ti^{IV}/V_{Cr}^{'''}$	-44.86	- 48.62	- 3.76
0001	$Cr^{VI}/V_{Cr}^{'''}$	-178.88	-180.54	- 1.66
$10\bar{1}2$	$3\ Ti^{IV}/V_{Cr}^{'''}$	-44.86	- 47.24	- 2.38
$10\bar{1}2$	$Cr^{VI}/V_{Cr}^{'''}$	-178.88	-176.60	+2.28

4.3.5 Computational exploration of the possibility of Chromium vacancy migration

The possibility of chromium vacancy migration was explored computationally by using the GULP code. For that a chromium vacancy was placed between three titanium ions and the defect energy was calculated. This vacancy was then moved via interstitial places into the chromium site one layer below. The defect energy for the interstitial sites was calculated and subtracted from the initial defect energy. Defect formation energies of the interstitial sites with respect to the initial surface are given in Figure 4.9. An energy barrier of 7.26 eV was calculated for chromium vacancy migration (see Figure 4.9). It appears that this defect is stable and does not migrate.

4.3.6 Computational investigation of other defect migrations

Charge balance in the lattice consequent upon introduction of Ti could be achieved also either by reduction of Ti^{IV} to Ti^{III} or by introduction of oxygen vacancies. In the calculations clustering of the defects was assumed. The charge neutral defect including an oxygen vacancy ($Ti^{IV}V_{Cr}V_O$) shows a bulk defect energy of +39 eV and is therefore unlikely to exist in the CTO lattice. Formation of Ti^{III} seems also unlikely because there is no experimental evidence of such a species in CTO (see chapter 6).

4.4 Discussion

The computational studies suggest that some lattice defects can be stabilised by the formation of defect clusters and by the segregation of these clusters to the surface. We have noted in the introduction that the surface sites of Cr_2O_3 are well characterised and that there have been speculations concerning the involvement of different parts of surface sites in the catalytic activity of chromium trioxide. Combination of these ideas with our computational studies of the chromium oxide surface suggest an interesting interpretation of the carbon monoxide combustion. It seems reasonable to propose that the chromium vacancy provides a site for carbon monoxide adsorption, promoted by the relaxation of the surface oxygen atoms away from the vacancy: the vacancy carries a net negative charge and CO is a dipole with oxygen positive, so it is plausible to suggest that CO adsorbs with oxygen down, in the pocket over the vacancy. Dissociation of the oxygen molecule is on Cr^{VI} (mainly for the case of Cr_2O_3) or Ti^{IV} (mainly for the case of CTO). The postulate is that oxygen is bound first as a peroxo species that then slowly dissociates: an analogous mechanism has recently been shown through computation to be feasible on Ti-substituted zeolites.[40] The second adsorption site needed for an oxygen atom could be either adjacent Cr^{III} or the surface pocket formed over

the Cr vacancy. The two surface oxygen atoms would then constitute the surface electron trap states, one of which would be significantly more reactive than the other. Removal of these surface trap states could be achieved by reaction with the carbon monoxide. (Scheme 1). Exposed Cr^{III} on the surface could provide an extra adsorption side for carbon monoxide. Carbon dioxide would be formed by reaction with oxygen, adsorbed on an adjacent Cr^{VI} or Ti^{IV} site. Reoxidation could then be achieved by dissociation of an oxygen molecule between the Cr^{VI} or Ti^{IV} and an adjacent chromium vacancy. This is a M-vK mechanism in which the catalytic entity is a surface defect cluster. Removal of Cr^{VI} sites, as believed to be the case in CTO, did indeed lead to a substantial decline in CO oxidation activity.[41] The reaction site would involve a Ti^{IV}/V_{Cr} defect cluster, as shown in Scheme 1.

The proposed model is capable of explaining the redox behaviour of Cr_2O_3 (0001) films that are grown as combustion catalysts. Although the formation of a $Cr^{VI}\,V_{Cr}$ cluster is unfavourable for the $(10\bar{1}2)$ face, it is likely that the Cr^{VI} charge can be balanced and therefore stabilised by adsorbed oxygen atoms from the air.

4.5 Summary

Atomistic simulations have been performed on the (0001) and $(10\bar{1}2)$ face to assess defect models for pure- and titanium doped Cr_2O_3. In the absence of titanium, one stable defect is a Cr^{VI} - $V_{Cr}^{'''}$ pair, which segregates to the (0001) surface. With titanium addition, a stable defect, segregated on both of the investigated surfaces, is the complex $(Ti^{IV})_3V_{Cr}^{'''}$. Distortion of the arrangement of surface oxygen above the Cr vacancy creates a potential binding site; the high-valence surface cation creates another. The spacing of the two sites is such that they could act in consort to promote a surface reaction, which can be formulated as a Mars- Van Krevelen mechanism.

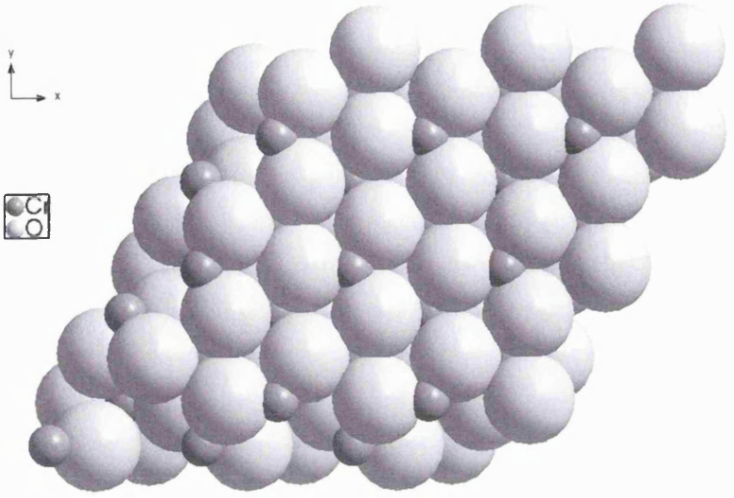

Figure 4.1. Top view of the Cr_2O_3 (0001) surface.

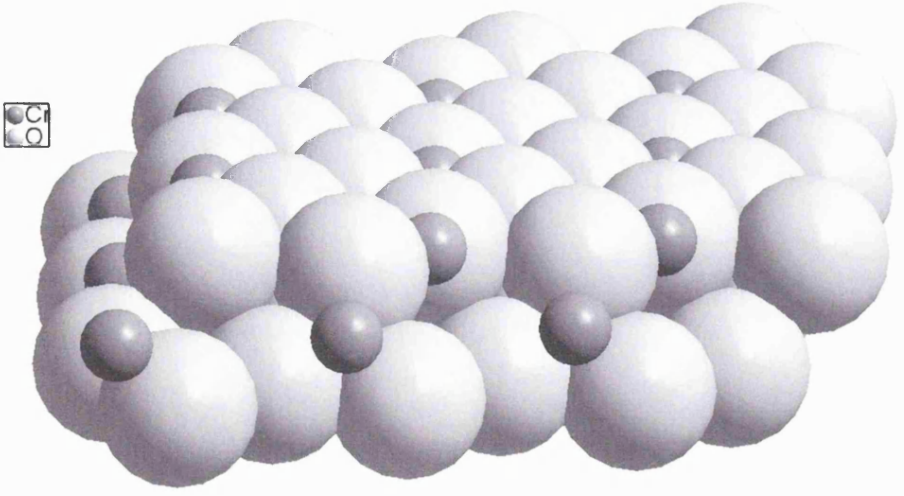

Figure 4.2 View along the Cr_2O_3 (0001) face

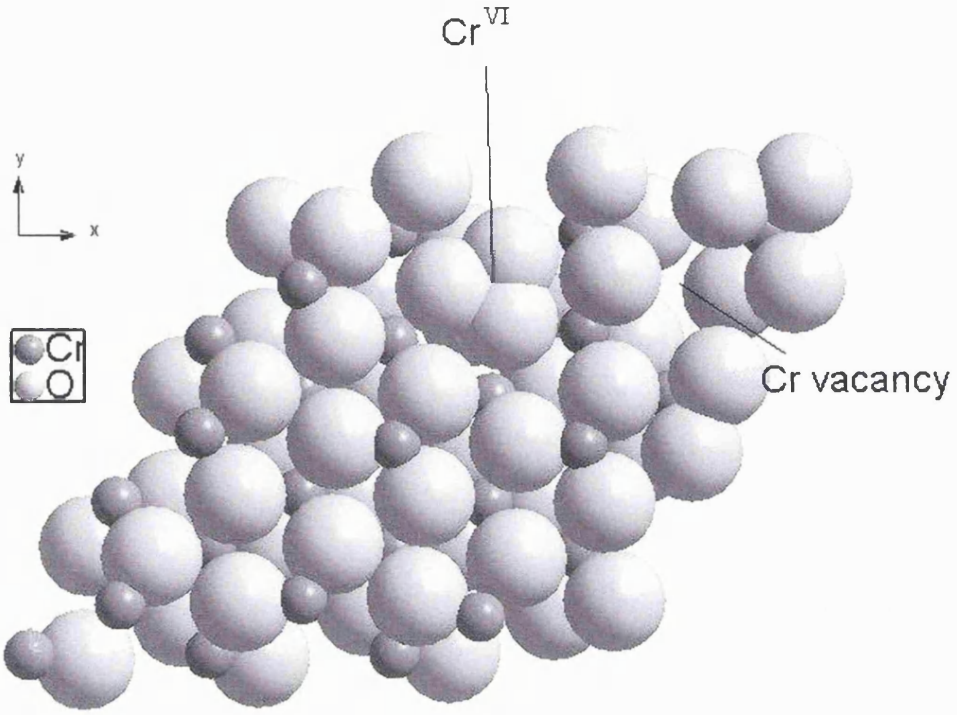

Figure 4.3 Top view of the defective Cr_2O_3 (0001) face. The arrows mark the position of Cr^{VI} and the chromium vacancy.

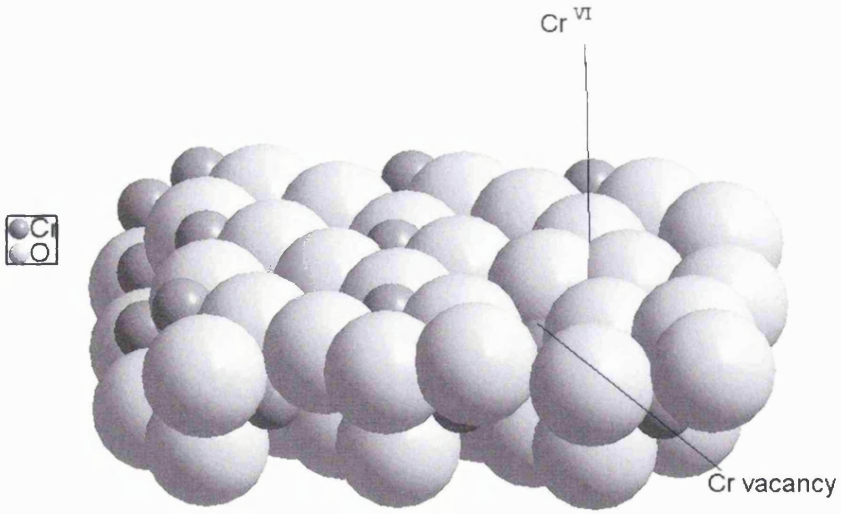

Figure 4.4 View along the defective Cr_2O_3 (0001) face

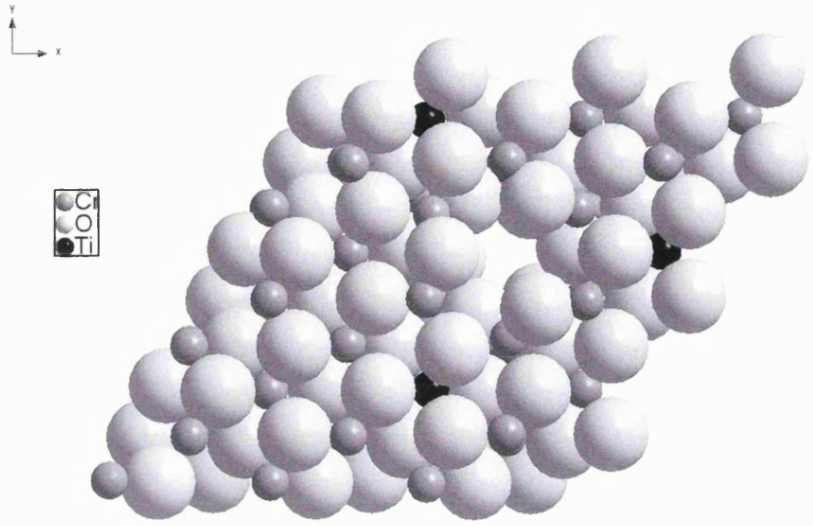

Figure 4.5 Top view of the Cr_2O_3 (0001) surface with the 3 Ti^{IV}/V_{Cr} cluster

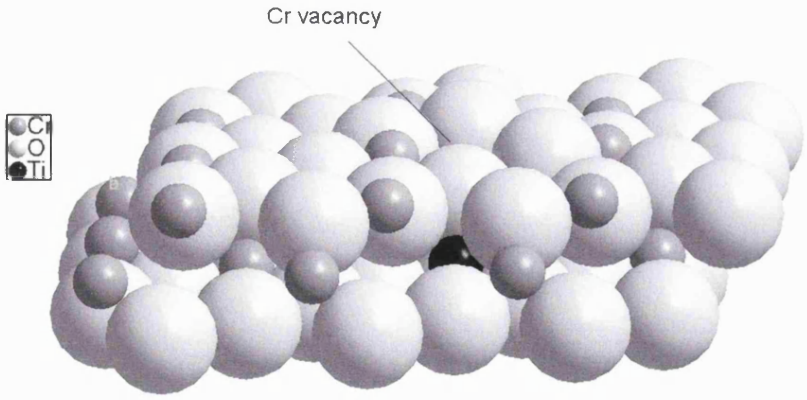

Figure 4.6 View along the (0001) face with the 3 Ti^{IV}/V_{Cr} cluster

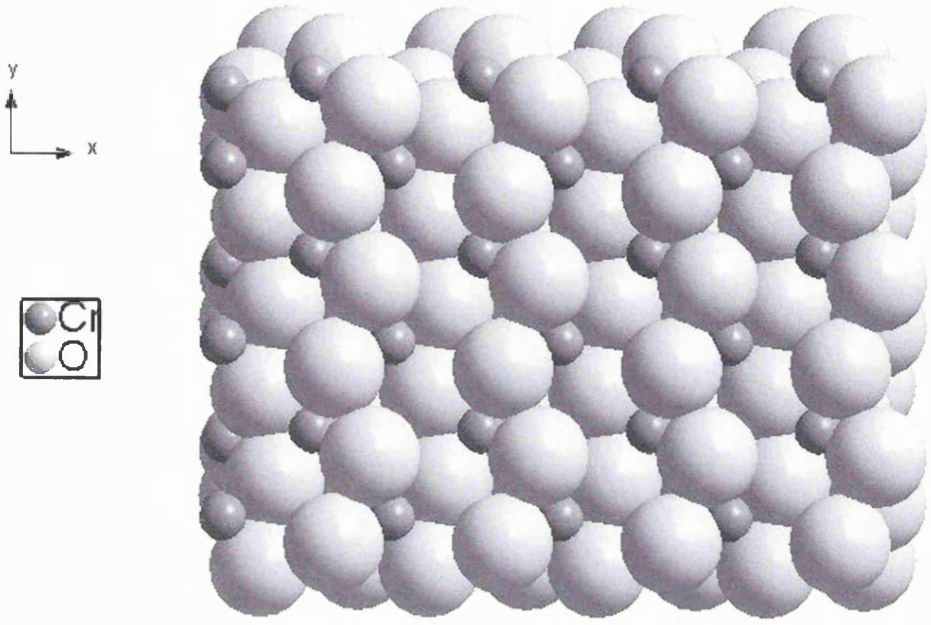

Figure 4.7 ($10\bar{1}2$) face

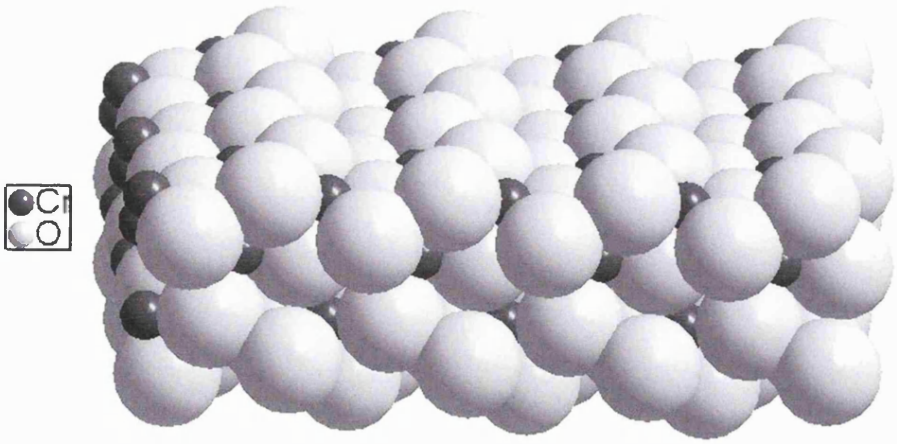

Figure 4.8 View along the ($10\bar{1}2$) face

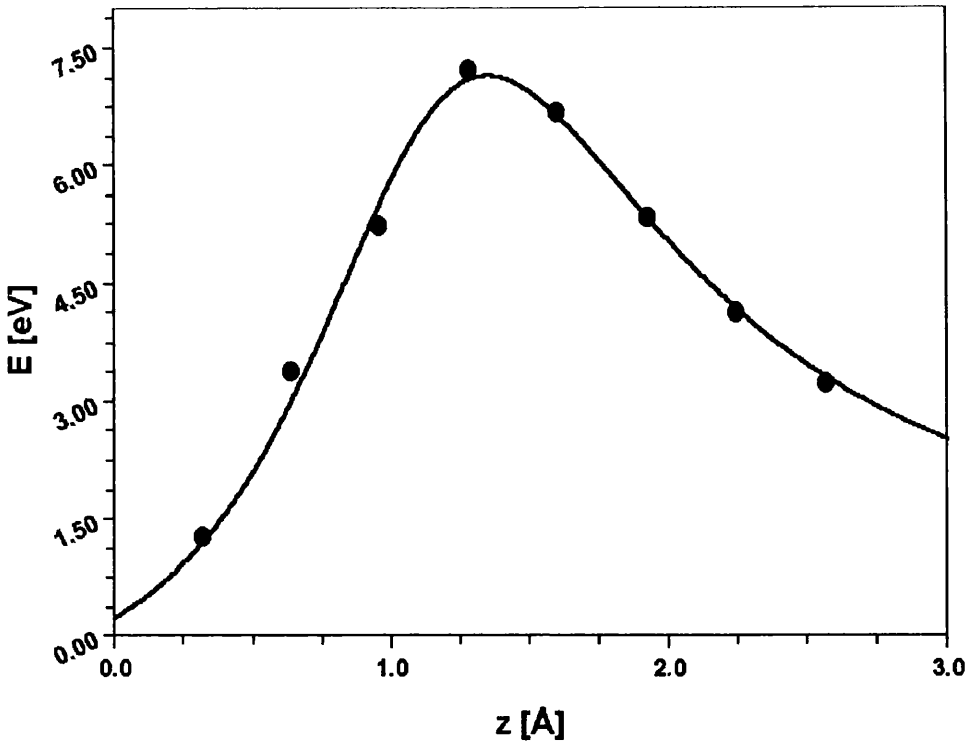

Figure 4.9 Activation energy of chromium vacancy migration

Scheme 1: Model for surface processes. Reactions A create reactive oxygen species, which can also act as surface trap states for electrons. Reactions B remove the reactive surface oxygen species. Reactions C regenerate the initial surface
state.

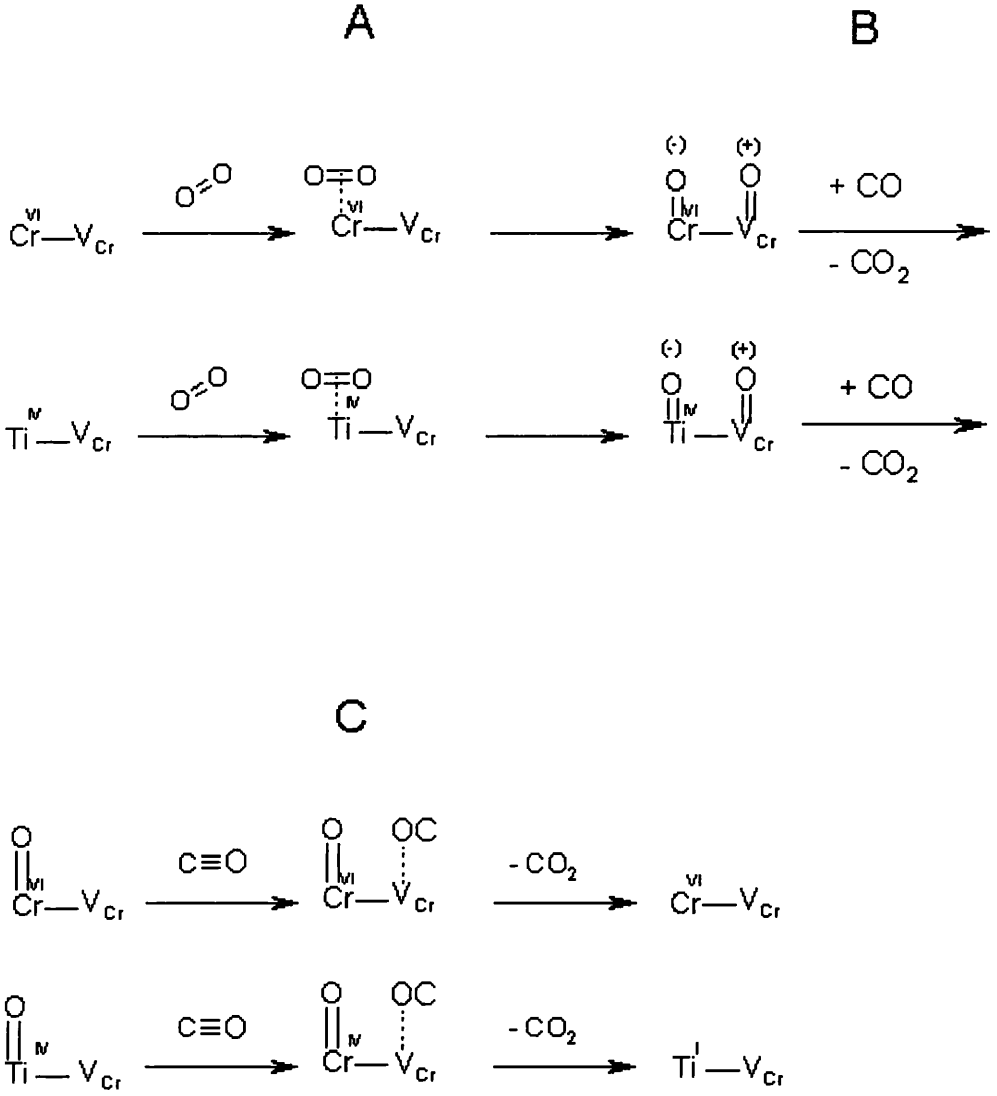

5 Gas-sensing behaviour of the solid-solution $Cr_{2-x}Ti_xO_3$ ($x \leq 0.5$)

5.1 Introduction

It has been mentioned in chapter 1 that chromium titanium oxide (CTO) has excellent capabilities for carbon monoxide detection. The purpose of this research was to present the behaviour of this material particularly in respect of its response to carbon monoxide and water vapour, to describe critical factors controlling the response and to discuss the surface chemistry which mediates the electrical response.

5.1.1 Phase diagram and defect model.

Early phase diagram work on the Cr_2O_3 – TiO_2 system reported a series of phases of the form $Cr_2Ti_{n-2}O_{2n-1}$ [42,43] and a phase (the 'E' phase) of nominal composition $Cr_2Ti_2O_7$ with a wide composition range. Above 1300°C, a two-phase mixture of 'E' and corundum phases is reported to exist over the range 45 to 98 mol% TiO_2 in $CrO_{1.5}$ [44]. However Henshaw *et. al.* [45] reported a solid solution phase in $Cr_{2-x}Ti_xO_3$ with $x \leq 0.4$. Jayaraman *et. al.* [46] showed that, over the range x=0.1 to 0.4, the solid solution was the major phase, merging with $CrTiO_3$ as the minor phase. All of these reports used solid-state reaction of mixed Cr_2O_3 – TiO_2 as the preparation method. Oyama *et. al.* [47] prepared CTO by laser-induced explosive chain reaction of CrO_2Cl_2-$TiCl_4$-H_2 in the

vapour phase. A complete solid solution in the range up to x=0.25 was found, with lattice parameters showing a small variation (8%) obeying Vegard's law. A defect model for CTO was proposed by Holt and Kofstad[48] and by Henshaw *et. al.* [45]: Ti substituted on Cr sites with charge compensated by Cr vacancies.

5.1.2 Electric properties.

At elevated temperature (>1000C), pure Cr_2O_3 behaves as an intrinsic semiconductor, with conductance independent of oxygen partial pressure and with activation energy for conductance 1.86eV, interpreted as corresponding to a band gap of 3.3eV and a migration activation energy (see below) of 0.2eV [49]. At lower temperature, more complex behaviour has been reported[50]. Holt and Kofstad [49,50] showed a very small dependence of the conductivity of pure Cr_2O_3 on oxygen partial pressure ($\sigma \sim P_{O2}^{1/20}$), consistent with earlier literature, and an activation energy for dense specimens of 0.2eV. They attributed this activation energy to an activation energy of mobility of the charge carriers. They postulated control of the conductivity at low temperature by extrinsic defects associated with impurities present above the solubility limit, which predicts, for the divalent impurities taken as the example, variation of $\sigma \sim P_{O2}^{1/8}$. They presumed that the equilibration was very slow, being determined by the very slow migration of lattice defects.

For $Cr_{1.98}Ti_{0.02}O_3$, at 1000C, Holt and Kofstad reported p-type conductivity for $P_{O2}>10^{-4}$atm, varying as $P_{O2}^{1/4}$, and n-type conductivity at lower P_{O2}, varying as $P_{O2}^{-1/4}$. At lower temperatures, for highly porous specimens, Henshaw *et. al.* [45] showed an increase of activation energy of conductivity with decreasing oxygen partial pressure, and a consequent decrease in magnitude of the power law exponent of the oxygen dependence of conductivity, from $\sigma \sim P_{O2}^{0.36}$ at 250°C to $\sigma \sim P_{O2}^{0.10}$ at 450°C (close to the value of the exponent observed by Holt and Kofstad). They introduced consideration of the surface processes for interpretation of the behaviour of

porous bodies at lower temperature, in particular noting the presence of Cr^{VI} species at the surface, detected by XPS. The effect of the surface processes can explain the higher activation energy for conduction shown by porous bodies in comparison with compact specimens.

A simple surface trap-limited model for the conductivity, in which oxygen adsorbed from the gas phase onto the crystallites of the finely porous structure acts as an acceptor state and is the major determinant of the electrical conductivity for such specimens, and with O^-_{ads} as the surface state, predicts $\sigma \sim P_{O2}^{1/2}$ as the limiting case at low temperature. At higher temperature, the conductivity should be determined by the charge carrier equilibria in the bulk of the crystallites, as considered by Holt and Kofstad. Both groups showed that Ti substitution caused a significant decrease in the electrical conductivity, also confirmed by Jayaraman *et. al.* [46].

5.2 Experimental

Pellets of CTO were prepared as described in chapter 2. Phase characterisation was carried out by X-ray diffractometry (Siemens D 5000 in transmission mode with incident beam monochromator and Cu Kα radiation). The electrical behaviour of the pellets and the gas response experiments were performed with the rig described in chapter 2.

5.3 Results

5.3.1 Phase characterisation.

Powder diffractometry (Fig 5.1) up to $x \approx 0.3$ showed a single-phase material with lattice parameters very similar to Cr_2O_3, as reported by Jayaraman *et. al.* [46]. The lattice parameter variation, shown by Oyama *et. al.* [47], was not observed: there was only a minor increase with increasing titanium concentration. A single diffraction line due to a second phase at 2 theta = 54.4 was just discernable at $x \approx 0.3$. This phase was clearly present at $x = 0.5$ and identified tentatively as $CrTiO_3$. Figure 5.2 shows the variation of lattice parameters with titanium concentration. The average crystallite size of the samples displayed in Figure 5.3 was determined by the Scherrer equation. Increasing Titanium concentration decreased the average crystallite size linearly. Above the solid solution range the average crystallite size does not show a trend. The obtained results agree very well with studies from Chabanis *et. al.* [51]on CTO prepared by a sol-gel route.

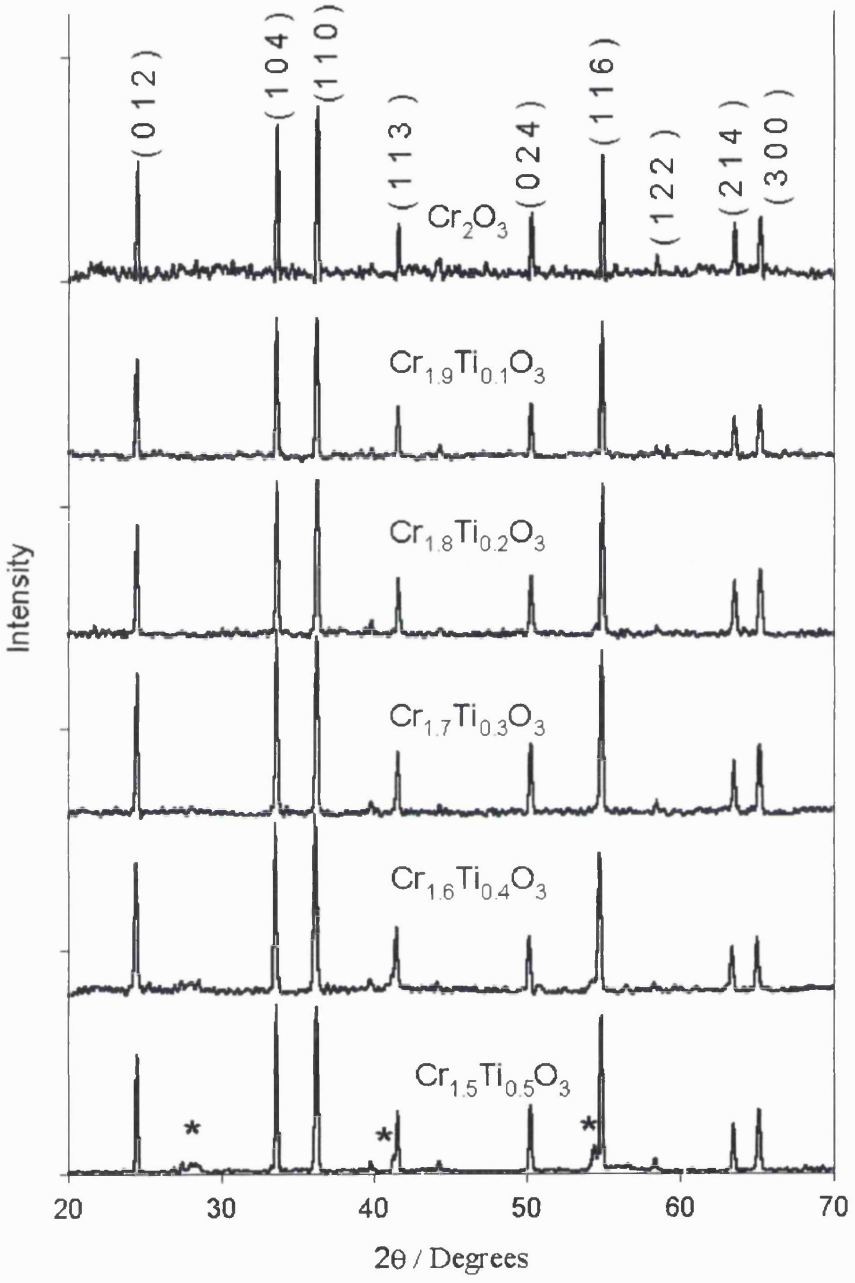

Figure 5.1 x - ray powder diffraction patterns of $Cr_{2-x}Ti_xO_3$ $0 < x < 0.5$

* second phase identified tentatively as $CrTiO_3$

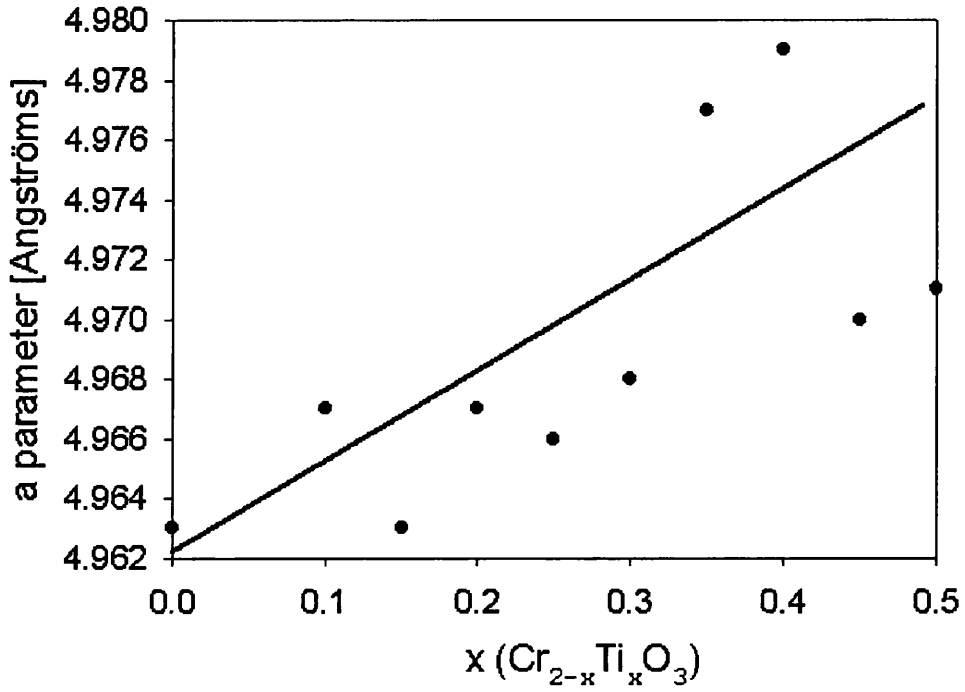

Figure 5.2 Lattice parameter variation with Titanium concentration

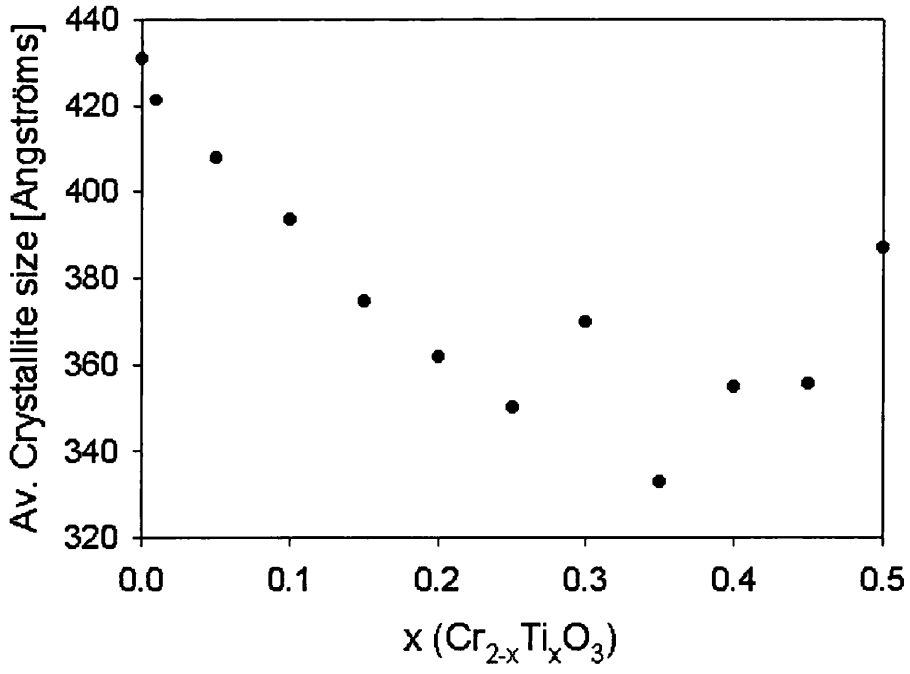

Figure 5.3 Average crystallite size determined by the Scherrer equation

5.3.2 Electrical behaviour

The conductivity measurements carried out in this research work correspond with the results obtained by Henshaw *et. al.*.[45] Figure 5.4 shows the resistivity and Figure 5.5 the activation energy for conductivity. Small additions of titanium decreased the conductivity by up to two orders of magnitude. The activation energy for conductivity increased by up to 100%. Further increasing titanium concentration decreased the activation energy down to the value of undoped Cr_2O_3.

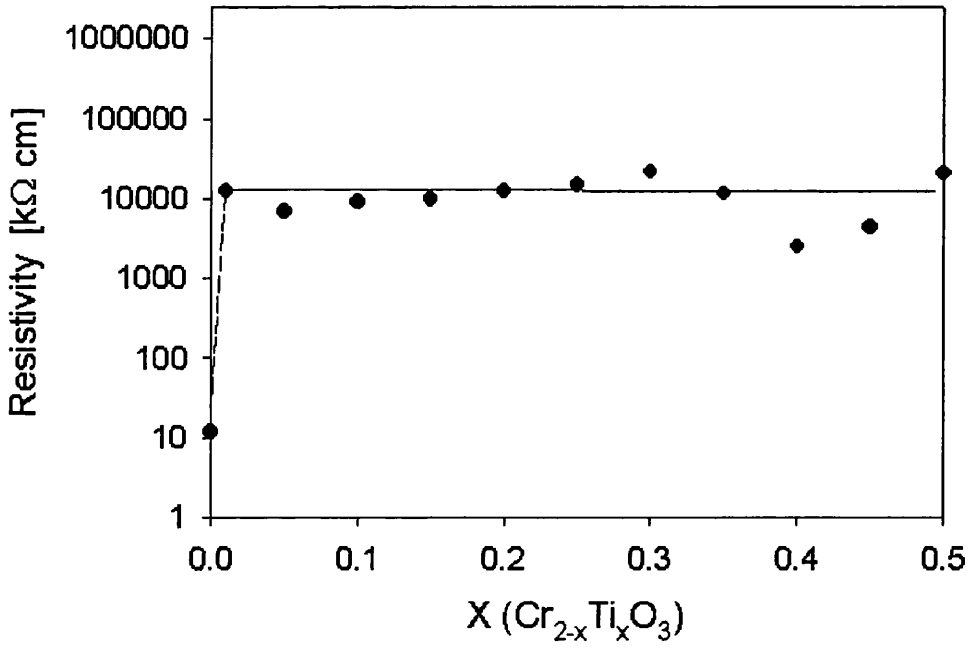

Figure 5.4 Resistivity at 300°C

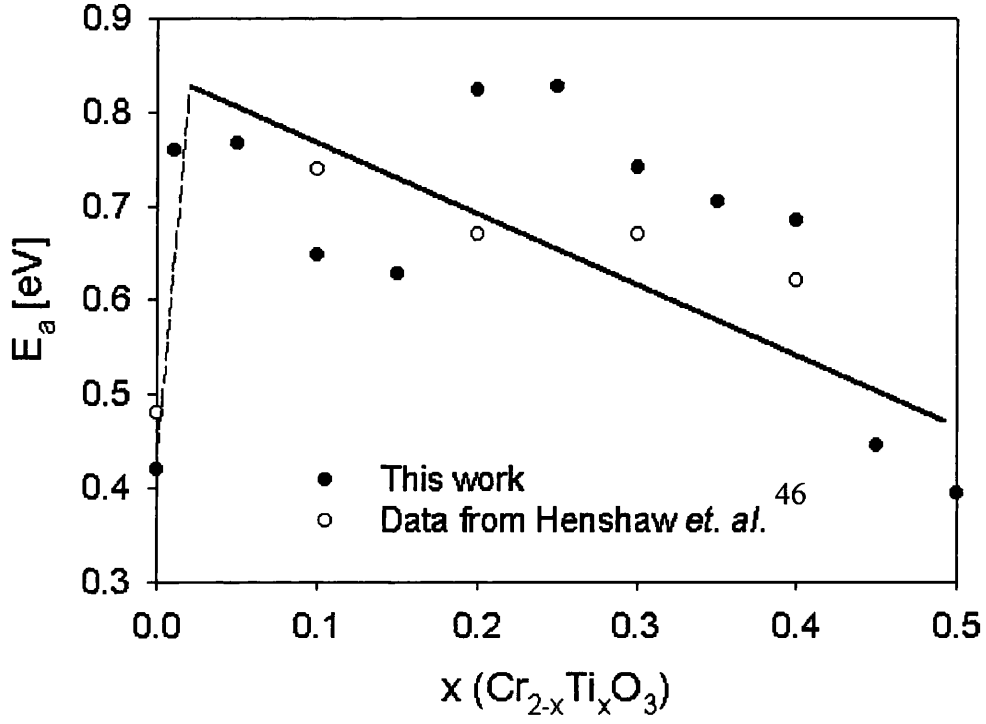

Figure 5.5 Activation energy for conductivity

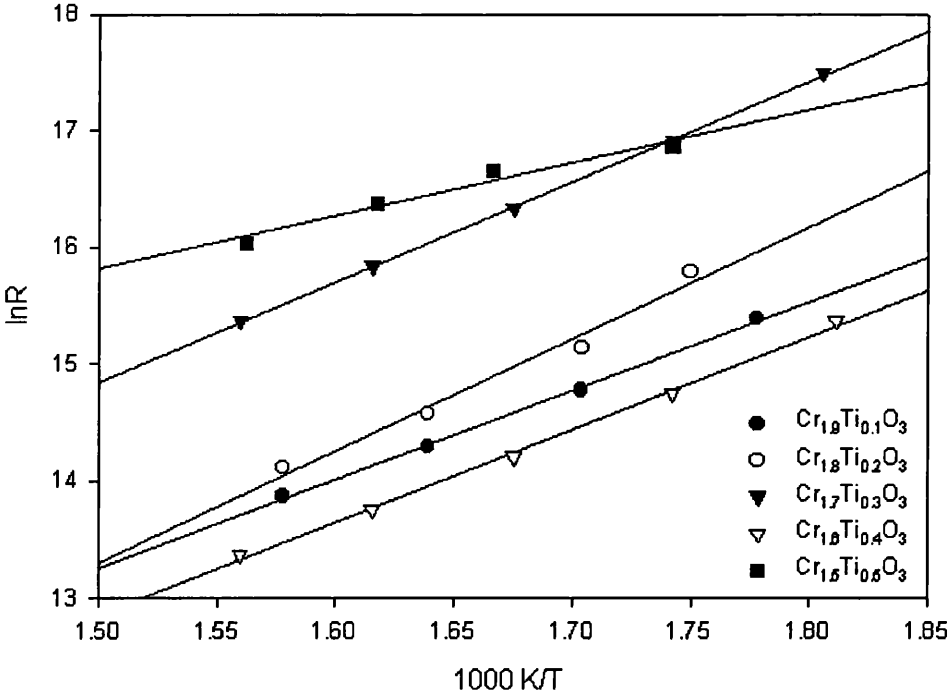

Figure 5.6 Arrhenius plots

5.3.3 Gas response

Important qualitative features of the behaviour as determined on porous pellets are shown in Figure 5.7. In the experiment the temperature was ramped from 300°C to 520°C (left wing) and back to 300°C (right wing), while the gas was switched in fifteen-minute intervals from air to air containing 500 ppm of carbon monoxide. This diagram illustrates that the substitution of a small amount of Ti into Cr_2O_3 caused a significant increase in resistivity and in activation energy of the resistivity, and the appearance of a significant gas response to carbon monoxide in air. Measurements at constant temperature showed that there was, in fact, a very small response of resistivity of Cr_2O_3 to traces of CO in air but that this signal disappeared at temperature ≥ 300 °C. The effect of Ti substitution was to give a much larger gas response evident at higher temperature. The gas response varied approximately as the square root of the gas concentration (Figure 5.8). Figure 5.9 shows the dependence of gas response on Ti substitution, again emphasising that only a very small substitution of Ti is necessary to achieve the gas response. Like the conductivity the gas response is temperature dependent (Fig.5.10)

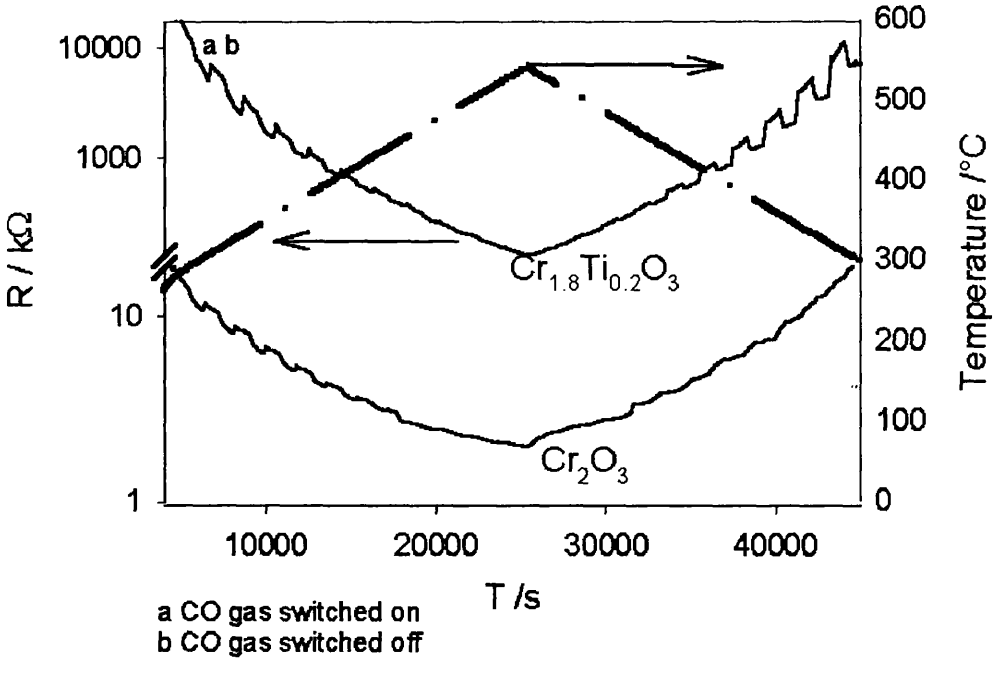

Figure 5.7 Ramp experiment

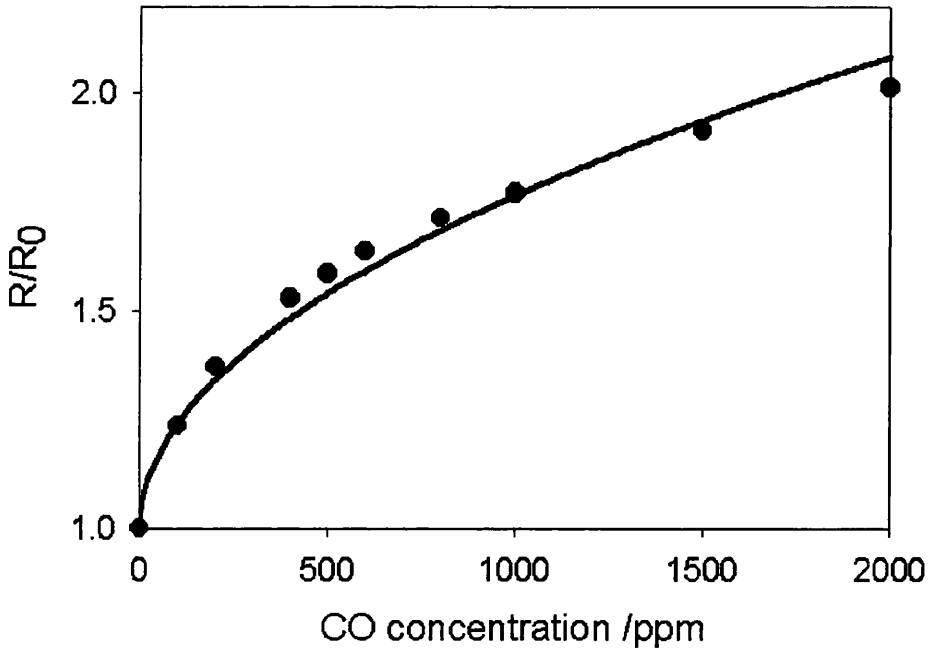

Figure 5.8 Response to carbon monoxide at 350°C

Devices fabricated by screen-printing show qualitatively similar behaviour to the pellets but with substantially larger and more rapid gas response because of their more open microstructure. What is practically significant about these devices in the rather small effect of variation in water vapour pressure upon the baseline and response, in comparison with the effects of gases such as CO. These effects are illustrated in Figure 5.11. The variation of response to water vapour and to carbon monoxide with variation of titanium substitution was different. The response to carbon monoxide reached a maximum for $x \approx 0.05$ and then declined with further increase of Ti substitution, whereas the response to water vapour went through a broad maximum at $x \approx 0.2$, similar to the behaviour reported for response to NH_3 by Jayaraman *et. al.* [46]. The important fact relevant to the gas response is the strong surface segregation of Ti. The maximum in response to CO is at a surface cation concentration ratio $x_{surf} = [Ti]_{surf} / ([Ti]_{surf} + [Cr]_{surf})$ ~0.23, and for water vapour it is at $x_{surf} \approx 0.5$ (Figure 5.9). The surface concentration of titanium was calculated from XP spectroscopy (see chapter 6)

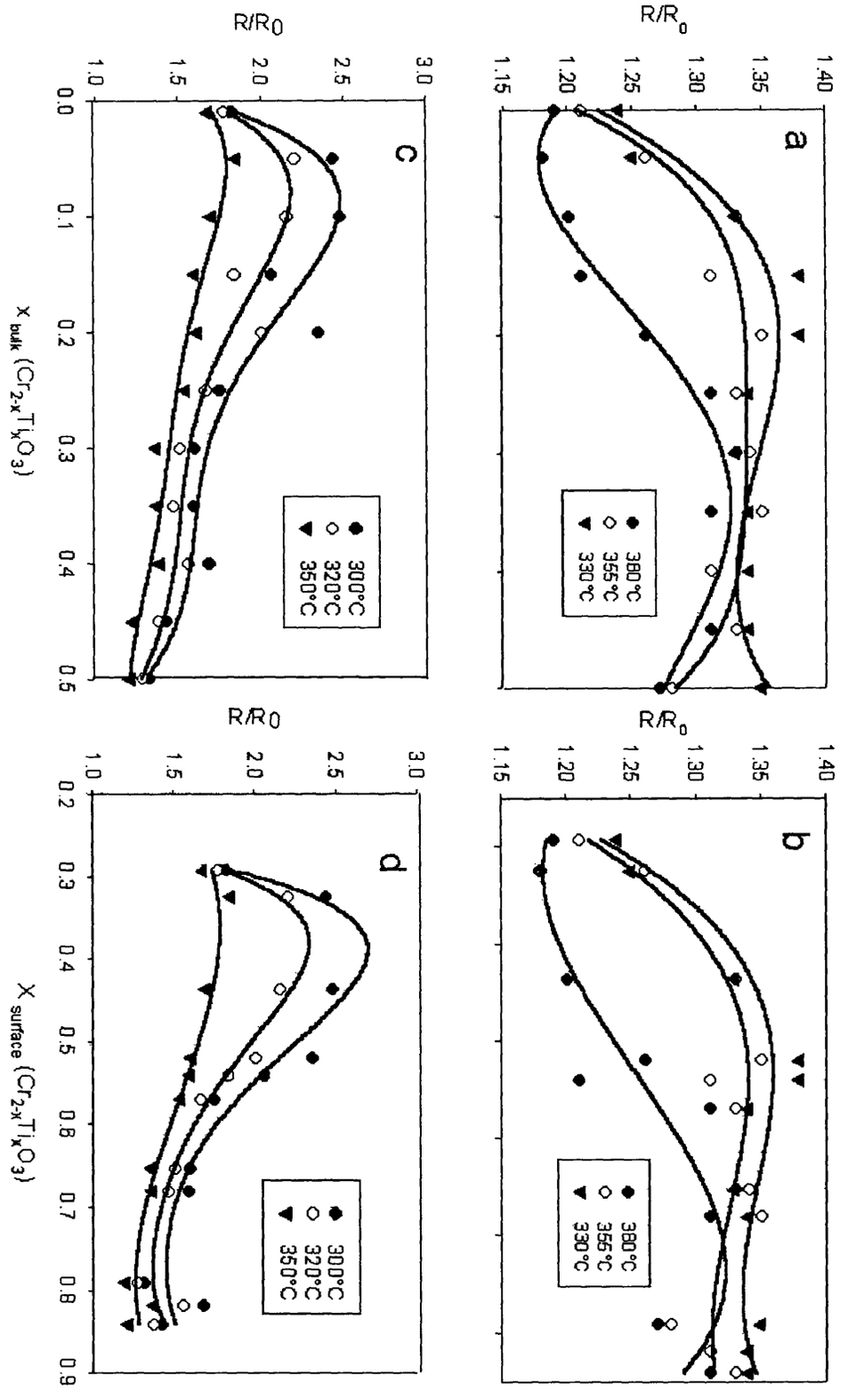

Figure 5. 9 Gas response to 500 ppm of CO and 100% rel. humidity at RT

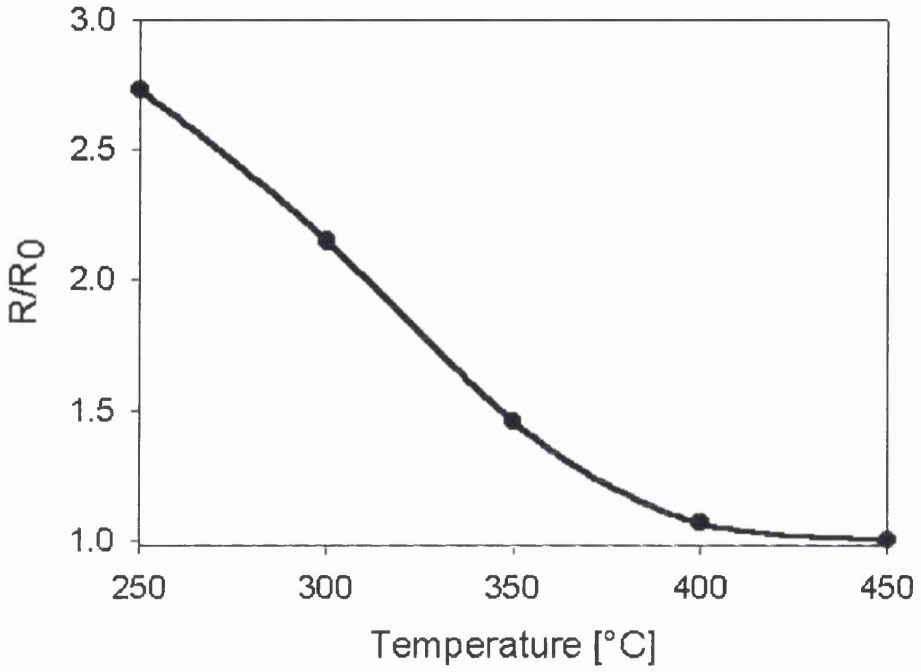

Figure 5.10 Gas response of a pellet to 500 ppm of CO as a function of temperature

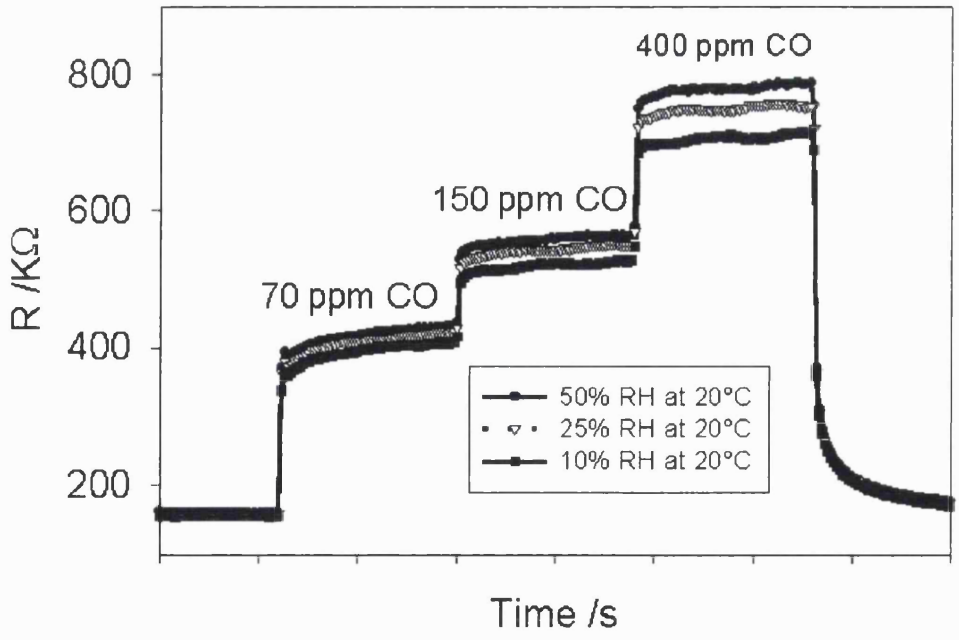

Figure 5.11 Gas response to CO and water of a sensor device

5.4 Discussion

5.4.1 Phase behaviour

The existence of a solid solution of TiO_2 in Cr_2O_3 with wide homogeneity range is confirmed. However, comparison with the high-temperature phase diagram [44] suggests that this phase has an upper stability temperature limit, over 1000 °C (the preparation temperature used here) and below 1300°C (the lowest temperature reported on the high temperature phase diagram). Oyama *et. al.* [47] show much larger lattice parameter variations than has been found in the present work. It is likely that their preparation had Ti uniformly distributed and was metastable because the powder was rapidly quenched from a high temperature whereas in the conventional solid-state reaction method the lattice strain caused by the defects is relieved by surface segregation. The computational results support this interpretation. The computational results also reveal the strong stabilisation of the $(Ti)_3$ V_{Cr} complex, which can be interpreted that the material has a tendency to phase-separate – which would rationalise the difference between our results and the high-temperature phase diagram.

5.4.2 Electrical behaviour

The surface conductivity of Cr_2O_3 can be attributed to the oxidation to Cr^{VI} whilst the bulk conductivity is probably associated with lower valent states like Cr^{IV} as suggested by Kofstad [50]. The computational results show that the Cr^{VI} V_{Cr} defect pair is stable and strongly surface segregated. It would be further stabilised at the surface by interaction with adsorbed oxygen. These chromate or polychromate species have been observed by IR spectroscopy [52, 53, 54]. The empty Cr 3d states act as electron acceptors, giving p-type conductivity localised near the surface. The effect of Ti substitution, enhanced by its surface segregation, is to decrease the acceptor state density in the surface region and

hence decrease markedly the conductivity. The activation energy found for the pure porous Cr_2O_3 specimen ~ 0.4-0.5 eV can be attributed to the activation energy for formation of valence band holes: i.e. to the energy difference between the unoccupied Cr^{VI} d states and the valence band. The activation energy for specimen with small Ti substitution ~0.8 eV is too small to correspond to band gap excitation It could be attributed to the activation energy for excitation from a surface acceptor state. The decrease in activation energy with increasing Ti substitution could be attributed to a change in the energy of the state with respect to the valence band edge.

5.4.3 Gas response

The simplest phenomenological model is that the sensor material behaves as a parallel combination of a gas-insensitive (the 'bulk') and a gas sensitive resistor (the surface) with some modification reflecting the influence of the microstructure [7]. Here, we interpret the conductive 'surface' element as due to both a surface layer of acceptor states associated with Cr^{VI} species and an accumulation layer of holes whose charge balances charge trapped in surface acceptor states. Oxygen adsorbed on the surface acts as the surface acceptor state: variation of the surface acceptor density as a consequence of reaction of surface oxygen with gas phase species is what confers gas sensitivity. If the bulk acceptor concentration in the surface region is too large then variations of surface acceptor state density have little effect on the conductivity. The effect of Ti is then simply to diminish the concentration of surface-segregated acceptor states - Cr^{VI}. Callister *et. al.* [26] used the same interpretation to explain the effect of TiO_2 on the sintering rate of Cr_2O_3. The surface segregation of Ti is thus particularly important since it ensures that a small addition of Ti has a particularly marked effect. Ti present in the bulk would also have an effect of decreasing the bulk acceptor state density, hence of decreasing the conductivity of the bulk element. Since the bulk element shunts the gas

sensitive surface element the effect would be to further enhance the gas sensitivity.

It has been noted previously on a number of systems that the effects of water vapour are exerted on surface sites different to those involved in the gas response. The same effect can be discerned in the present system: Figure 5.9 a and b shows the gas response and the response to water vapour plotted against the surface concentration of Ti. The gas response appears immediately there is sufficient Ti to neutralise the bulk acceptor states near the surface and then declines with further increase of Ti content. The water vapour response on the other hand climbs to a maximum at $[Ti/(Ti + Cr)]_{surface} \sim 0.5$, corresponding to an overall composition of $Cr_{1.85}Ti_{0.15}O_3$. Since TiO_2 added in small amounts acts as a sintering aid for Cr_2O_3 [26] and the microstructure is noticeably coarser for the larger additions of Ti [55] (although the crystallite size indicated by X-ray diffraction line broadening is not increased), it is possible that the decline in signal with increasing Ti content is attributable to some degree to the effects of changing microstructure. However, differences in behaviour of CO and H_2O response to increase of Ti at low Ti content imply a different interaction with the surface. One can speculate that H_2O is interacting predominantly via the Ti cations on the surface whereas the gas response appears predominantly as a result of an interaction involving surface Cr. The decrease of surface Cr with increasing Ti therefore would cause a decrease in gas response, as observed.

5.4.4 Speculations concerning surface interactions mediating the gas response

It has been previously noted that the surface sites, which mediate gas response, are different to those, which mediate the major reaction paths for surface catalysed combustion. [56] This effect is particularly noticeable for the electrical response of CTO to carbon monoxide: on this material, in a flow-through packed bed reactor, there is no easily discernable catalysed combustion reaction of carbon monoxide at temperatures below 400 °C.

However, the sensor signal is strong at temperatures below this. Speculations on the active site for sensor response can be developed from other studies of the catalytic behaviour of chromium oxides and from our computational studies. The Mars and van Krevelen mechanism that was discussed in the last chapter can be also applied to explain the gas sensing behaviour.

As discussed in the last chapter Burwell *et. al.* [22] introduced the idea of a coordinatively unsaturated site. The idea of activation of the material due to heating explains the behaviour observed in the ramp experiment in Figure 5.7.

The activation of the catalyst is achieved by removal of water from surface sites. Consequently adsorption of carbon monoxide and oxygen increases rapidly. For the case of CTO this leads to an increased gas response visible in Figure 5.7 (right wing of the experiment). Cr_2O_3 shows the opposite behaviour, because the increased oxygen adsorption leads to increased formation of acceptor states, diminishing the gas response. The difference in response for water vapour and for carbon monoxide is understandable if water is preferentially adsorbed onto surface Ti, whilst CO preferentially adsorbs onto surface Cr.

5.4.5 Summary

$Cr_{2-x}Ti_xO_3$ is an excellent gas sensor material, with stability of performance over the short and long-term and minor influences of variations of humidity. The phase limit is at $x \simeq 0.3\text{-}0.4$; above the phase limit a 2-phase mixture with $CrTiO_3$ is found. Substitution of Ti strongly decreases the electrical conductivity of the porous bodies studied. The proportion of Cr^{VI} at the surface is decreased by Ti substitution. This effect, and the surface segregation of Ti, controls the gas sensor behaviour.

6 The influence of Ti^{IV} defects on the x-ray photoelectron spectra of Cr_2O_3

6.1 Introduction

It has been established in the previous chapters that chromium oxide is a material of multiple applications. Apart from being an excellent combustion catalyst material and – in combination with titanium - an outstanding solid-state gas sensor, it is also used as a pigment in the colour industry.

Apart from its wide range of practical applications chromium (titanium) oxide is also of a great scientific interest. XP spectroscopy of the Cr 2p region of Cr_2O_3 has been performed extensively in the literature. Many research groups have reported a splitting of the Cr $2p_{3/2}$ peak. There is some confusion about the origin of this splitting. In the literature the splitting has been attributed to multiplet splitting [57,58] satellites [59] or mixed valences [60]. Tsurkan *et. al.* [61] have recently observed a splitting of the Cr 2p states in chromium sulphides and selenides. They attributed this effect to the local magnetic moment at the Cr ion. This explanation is used in this chapter to explain the effect of titanium impurities on the XPS of the Cr 2p levels of $Cr_{2-x}Ti_xO_3$ ($0<x<0.2$).

Dusastre *et. al.* used x-ray photoelectron spectroscopy to investigate antimony surface segregation on tin dioxide. This was done by quantification of the tin, oxygen and antimony peaks of the spectra. The ratio of tin to antimony was then compared with the ratio used in the preparation. A large surface segregation of antimony was found. The same method is also applied in this work to investigate titanium surface segregation in Cr_2O_3.

6.2 Multiplet splitting (exchange splitting)

The core level structure is a direct reflection of the electronic structure of the atoms. Investigation of the Cr 2p region reveals a doublet arising through spin – orbit (jj) coupling. Two possible states characterised by the quantum number j (j = l + s) arise when l > 0. The difference in energy of the two states reflects the parallel or anti parallel nature of the spin and orbital angular momentum vectors of the remaining electron. This separation can be several electron volts. The relative intensities of the doublet peaks are given by the ratio of their respective degeneracies (2j+1).

Multiplet or exchange splittings can result from coupling between core electrons and unpaired d electrons. In most cases multiplet splitting is observed in the 3 s spectra. The splitting between the multiplet lines of the Mn 3s levels in manganese compounds is reported to be about 10 eV binding energy. It is much more difficult to observe multiplet splitting in p levels because the much smaller distance between the peaks leads to an overlap in multiplet peaks. Separation of the peaks has proven to be very difficult. The first indirect evidence for multiplet splitting of the 2p peaks was presented by Frost *et. al.* [62] Soon afterwards the first direct evidence was found in square planar Co^{II} complexes. Tsurkan *et. al.*[61] investigated the splitting of the Cr 2p XPS signals in ternary sulphides and selenides. Compounds covering a variety of electrical and magnetical properties were chosen, including metallic and semiconducting ferromagnets, semiconducting ferrimagnets and insulating antiferromagnets. All the observed samples showed a splitting of 1.0 ± 0.1 eV. The effect was attributed to the magnetic exchange splitting due to the local magnetic moment of the Cr ion. This interpretation is based on previous observations of a similar exchange splitting in Mn 2p core levels in some semi metallic ferromagnetic Heusler alloys. Plogmann *et. al.* [63] have given a complete description of the electronic and magnetic properties of these compounds. Fully relativistic photoemission calculations were carried out by these authors in order to deliver a quantitative description of the core level

spectra. It has been proven that the observed splitting is directly correlated to the local magnetic moment at the Mn sites. The intensity distributions in both Mn $2p_{3/2}$ peaks can be explained mainly by direct transitions from the Mn $2p_{3/2}$ states into final d bands. Hence changes in the relative intensities are dominated by the dipole transition matrix elements. A very good agreement between theory and the observed spectra has been achieved.

Cox *et. al.* [35] performed XP spectroscopy on a Cr_2O_3 $(10\bar{1}2)$ surface and Salvi *et. al.*[64] investigated Cr_2O_3 powder. Both research groups etched their samples with Ar^+ ions for 30 minutes prior to investigation and they only observed one Gaussian shaped peak.

6.3 Experimental

6.3.1 Sample preparation

Materials were prepared by solid-state reaction of Cr_2O_3 and TiO_2 as described in chapter 2. A small sample of the loose material was attached to the sample tray by double-sided tape. A silver mask was placed around the sample to avoid charging effects.

6.3.2 Surface investigation

XPS spectra were recorded (VG ESCALAB 220iXL instrument) using focused (300 μm spot size) monochromatized Al Kα radiation. The binding energies were referenced to the oxygen 1s peak at 531.0 eV binding energy and the sample charging was controlled with a 3 eV flood gun. Spectrum quantification was performed using a Shirley background and sensitivity factors were obtained from Wagner *et. al.* [65] The effect of etching on the intensity of the peak splitting was also observed. The etching was done for 6 minutes with a 3 kV beam and 2 μA. current.

Table 6.6.1 Sensitivity factors

Peak	Sensitivity factor
Cr2p3	1.50
O 1s	0.66
Ti 2p3	1.20

6.4 Results

XPS investigation was performed on chromium titanium oxide samples with a titanium concentration from ($0<x<0.25$) for $Cr_{2-x}Ti_xO_3$. A survey spectrum is displayed in Figure 6.1. The binding energies for the species observed on the surface are listed in Table 6.2. They correspond very well to the values obtained from the literature.[66]

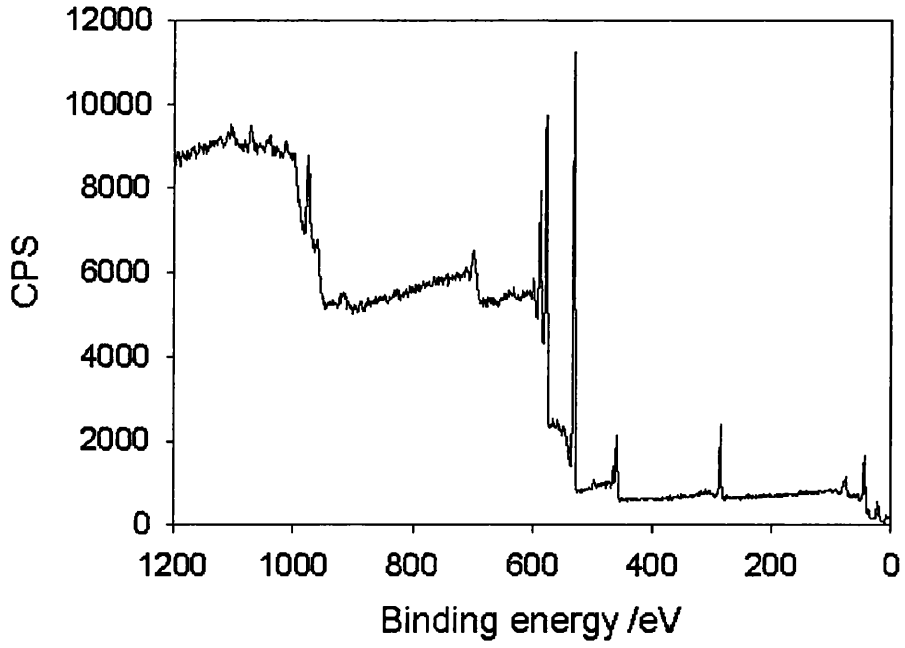

Figure 6.1 Survey spectrum of Chromium titanium oxide

Table 6.2 The main elements on the surface and their binding energies

Elements	Binding energy [eV]
C 1s	285.2
Ti 2p	458.8
O1s	531.0
Cr 2p	577.4

6.4.1 The effect of the Ti defects on the Cr peaks

The XPS investigation focussed on the Cr 2p region displayed in Figure 6.2. The spectra are normalised to the intensity at 582.0 eV binding energy. The 2p region is divided into a $Cr2p_{1/2}$ and a $Cr2p_{3/2}$ due to spin orbit coupling. The latter region consists of three features at 576.4, 577.4 and 580 eV binding energy respectively. The shoulder at 580 eV BE has been assigned to Cr^{VI} by comparison with CrO_2 and chromates[66]. Since the binding energies of Cr^{III} and

Cr^{IV} are very close the presence of Cr^{IV} in the spectrum cannot be ruled out. All of the signals were affected in a characteristic way by Ti substitution. The Cr^{VI} signal was decreased by about 40% (Fig. 6.5). The $Cr2p_{3/2}$ splitting was blurred, but then sharpened again with further increase of Ti. (Fig.6.2) Etching of the surface with argon ions significantly reduced the splitting. (Fig. 6.6) A spectrum of the Ti 2p region (Fig. 6.4) shows no splitting or deformation of the Ti $2p_{3/2}$ peak indicating a single oxidation state of +IV. A clear signature of the Cr3d states can be observed at the valence band edge (Fig 6.3) With a small Ti substitution, the valence band edge was moved by 1.3 eV referenced to the C1s peak at 285 eV and the Cr states diminished relatively in intensity.

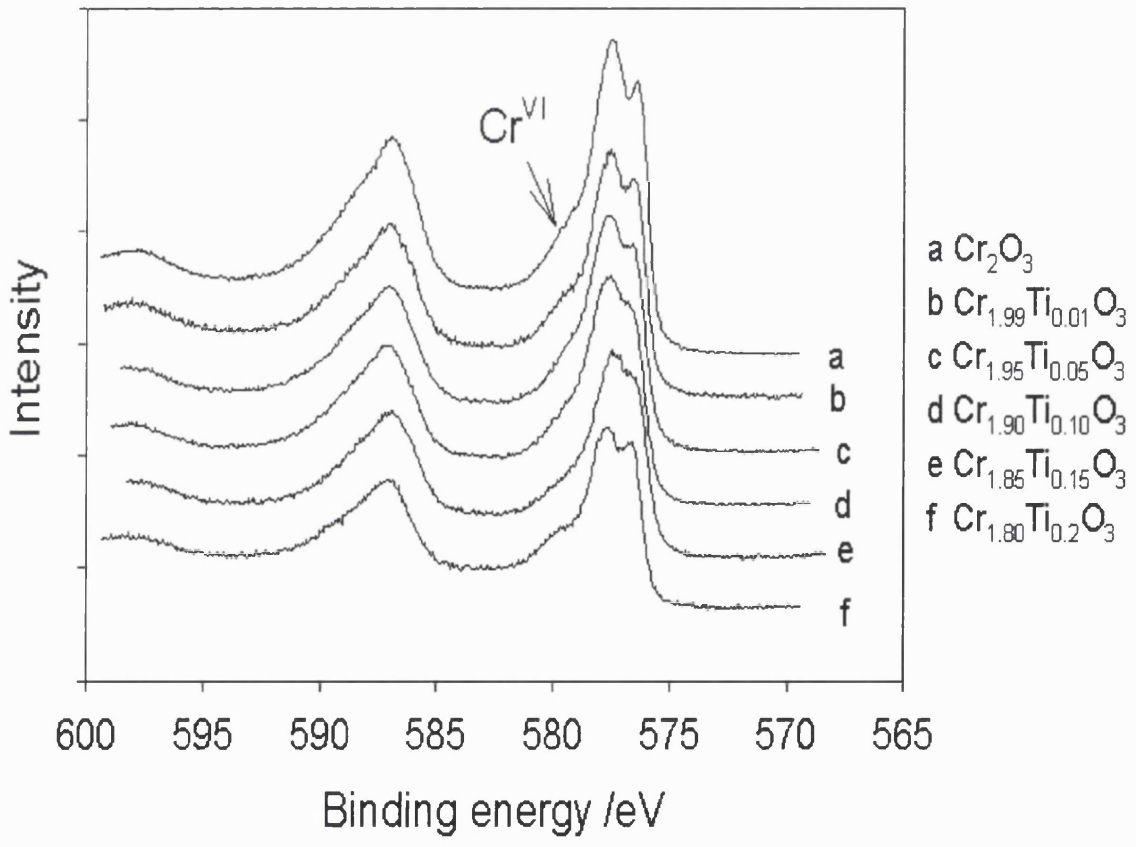

Figure 6.2 XP core spectra of the Cr 2p region of $Cr_{2-x}Ti_xO_3$

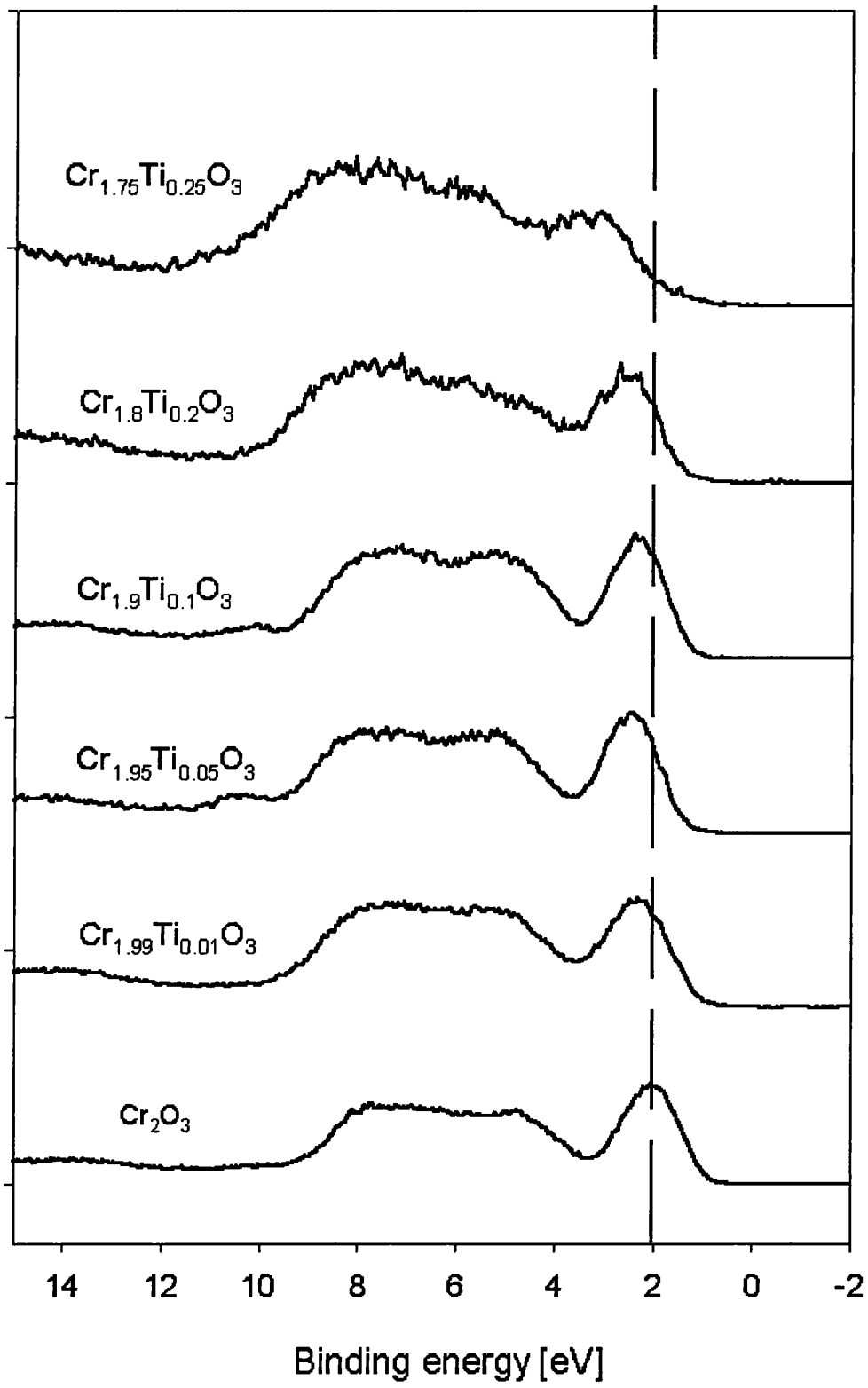

Figure 6.3 XP valence band spectra of $Cr_{2-x}Ti_xO_3$

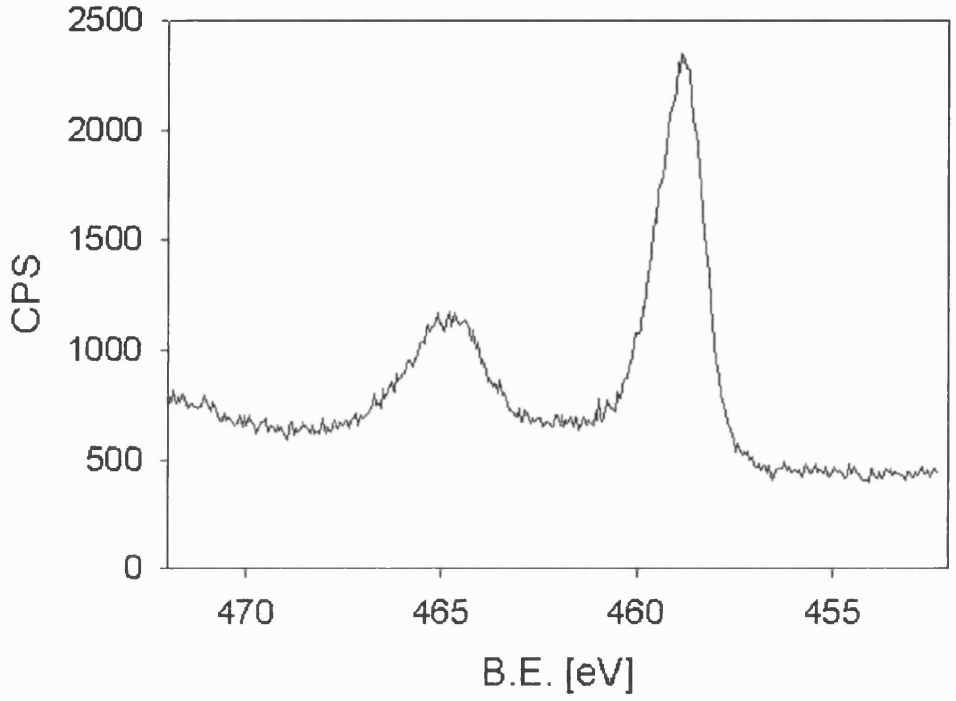

Figure 6.4 XP core spectrum of the Ti 2p region ($Cr_{1.8}Ti_{0.2}O_3$)

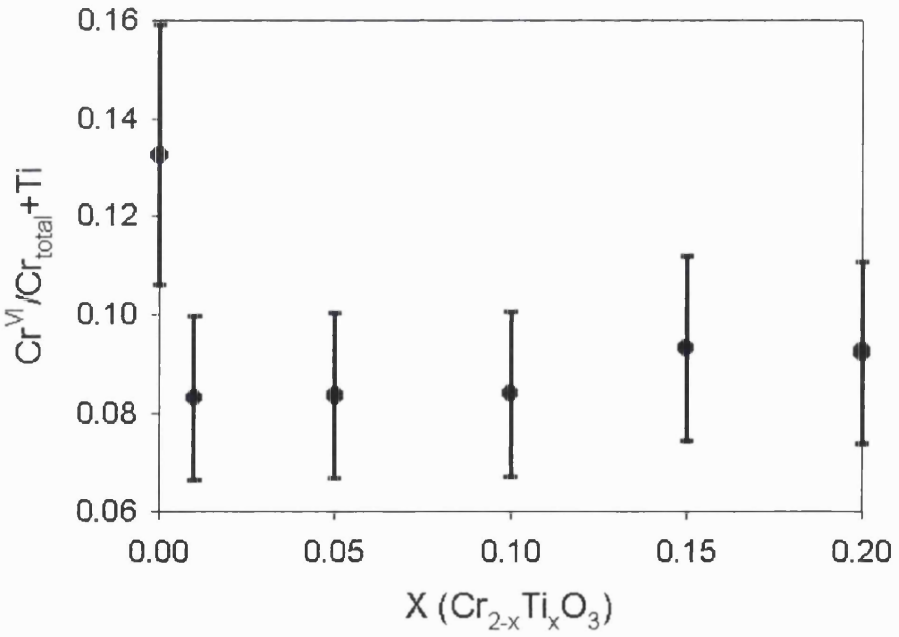

Figure 6.5 Variation of surface Cr^{VI} with increasing titanium concentration

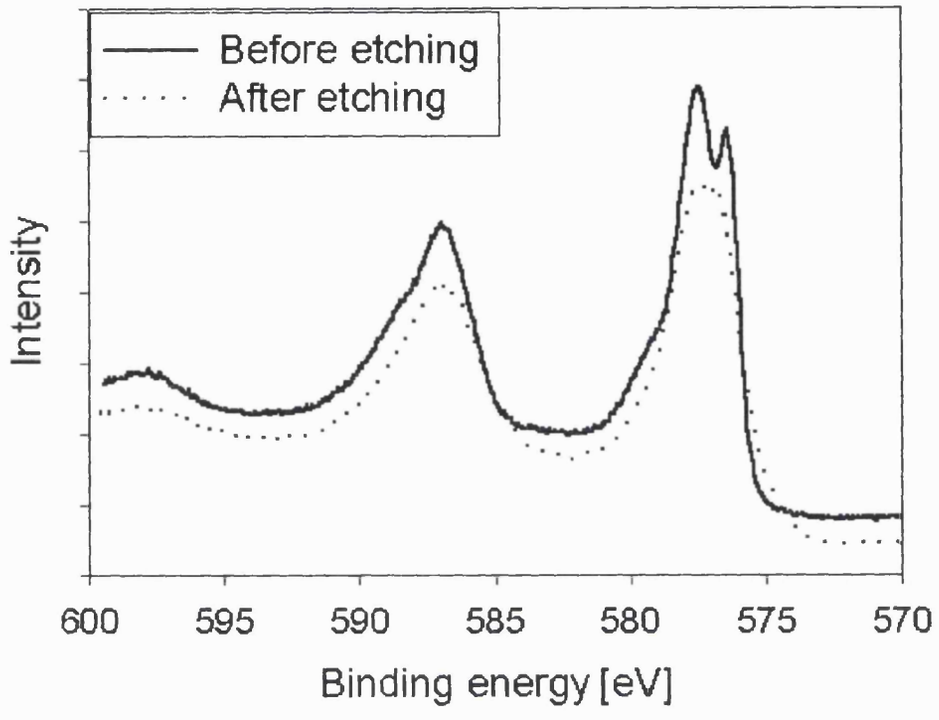

Figure 6.6 The Cr 2p peak of Cr_2O_3 before and after etching

6.4.2 XPS investigation of surface segregation

XPS showed a strong Ti surface segregation (Fig 6.7). The fitting was done by using a Langmuir equation.

$$X_s = X_{sat} \times \frac{KX_b}{1 + KX_b} \qquad (6.1)$$

where x_s and x_b are the fractions of titanium being on the surface and in the bulk respectively. They are defined as:

$$X = \frac{[Ti]}{[Ti + Cr]} \qquad (6.2)$$

x_{sat} (= 0.5) represents the upper phase limit, where $CrTiO_3$ is tentatively formed. This is the Langmuir-McLean model in which it is assumed that the

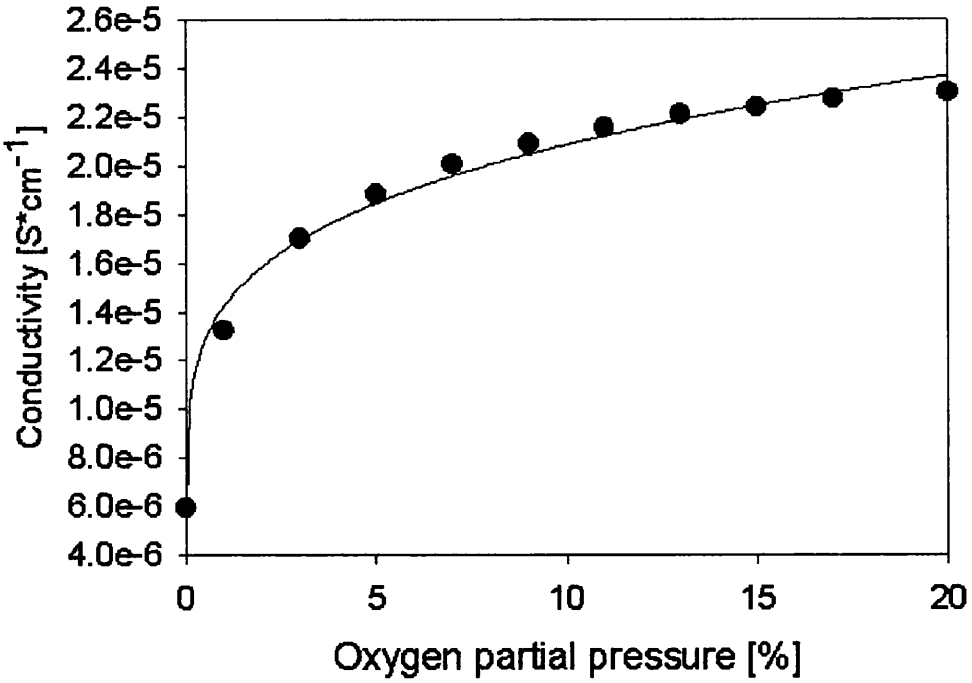

Figure 7.1 Conductivity of a sensor device at 400°C. The fitted curve is $\sigma \approx P_{O2}^{1/4}$

7.3.2 Gas response to H_2S

The experiments showed that CTO is capable of detecting small quantities of H_2S in a nitrogen atmosphere. The response to 5 ppm of H_2S at 450°C operating temperature is displayed in Figure 7.2. The first exposure to H_2S (black dots) showed a high gas response that can be divided into two phases. One initial phase from 0 up to 200 s and a second phase for the rest of the gas response. After the first pulse the baseline resistivity increased by 80%. The response curve obtained for the second pulse of H_2S (white dots) looked similar in Phase 2, but the increase in resistance was much quicker during Phase 1 indicating a different response mechanism. The baseline resistivity shifted by another 5.5%. The gas response varied with the square root of the gas concentration. (Fig. 7.3)

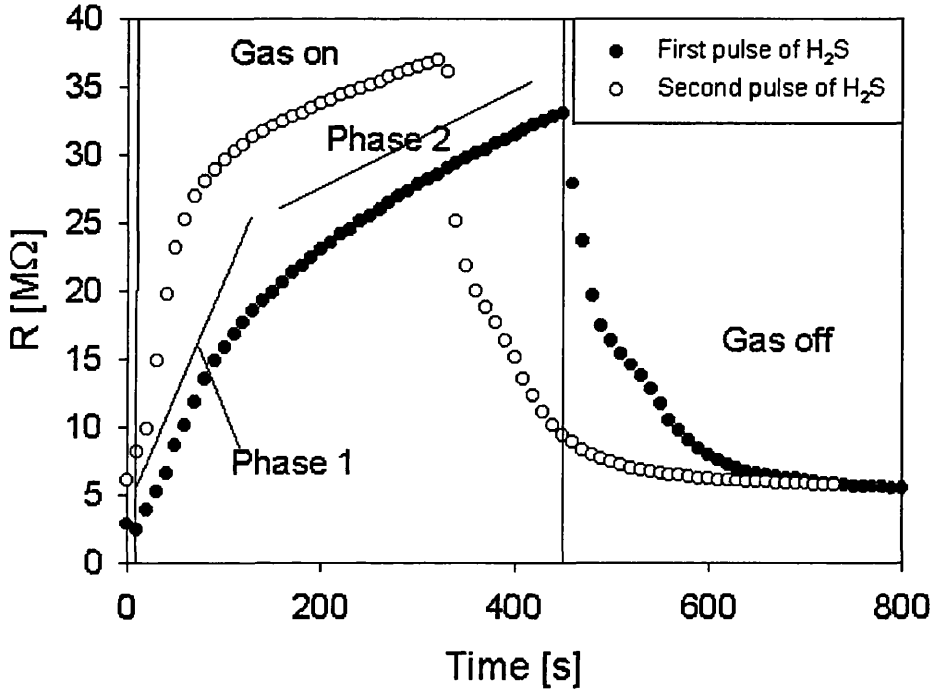

Figure 7.2 Gas response to 5 ppm of H_2S in N_2 at 450°C

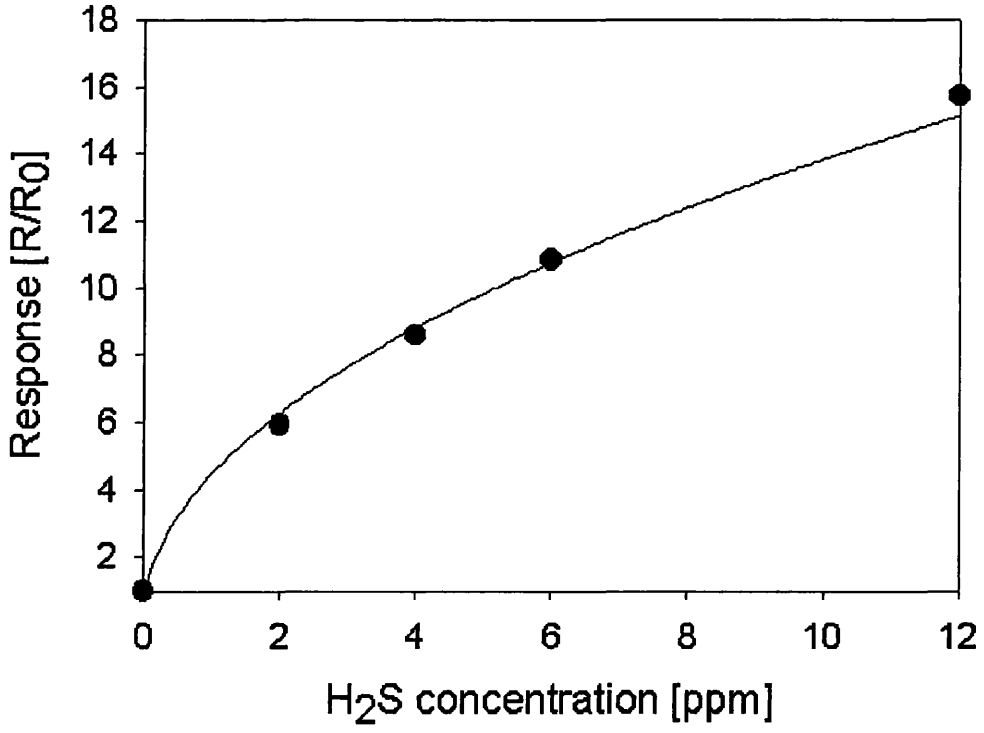

Figure 7.3 H_2S response of a sensor device in N_2 at 450°C.

The fitted curve is $R/R_0 \approx P_{H2S}^{1/2}$

composition is uniform and equal to the bulk value in all layers below the surface layer.

The measured signal has a contribution from the bulk. The element of intensity d*I* of the photoelectron signal comes from a depth *h* below the surface, where the mole fraction of Ti is x_h, can be written:

$$dI = I_0 X_h e^{\frac{-h}{\lambda_0}} dh \qquad (6.3)$$

where λ_0 denotes the mean free path of the photoelectron and the variation with depth of the incident x- ray intensity is ignored. Hence, the signal due to subsurface Ti I_B is

$$I_B = I_0 \int_{h_0}^{\infty} X_h e^{\frac{-h}{\lambda_0}} dh \qquad (6.4)$$

where h_0 denotes the depth of the first subsurface layer. Now, if one makes the crude assumption that the mole fraction of Ti is uniform with the depth and equal to the bulk value, x_b for all layers below the surface, the signal due to sub-surface Ti can be written as:

$$I_B = I_0 X_b \int_{h_0}^{\infty} e^{\frac{-h}{\lambda}} dh \qquad (6.5)$$

Hence a correction for the bulk contribution of the measured signal can be written:

$$x_{s,m} = (1-f)X_s - (X_b \times f) \quad (6.6)$$

where *f* is a constant describing the exponential decay of the signal with layer depth. Crudely the signal due to surface Ti is proportional to x_s h_0 whilst the signal due to subsurface Ti is proportional to $X_b \lambda e^{\frac{-h_0}{\lambda}}$ Hence:

$$f \cong \frac{X_b \lambda e^{\frac{-h_0}{\lambda}}}{X_b \lambda e^{\frac{-h_0}{\lambda}} + X_s h_0} \qquad (6.7)$$

The mean free path of the photoelectron, λ is 10 Å[35] and h_0 can be defined as the depth of one layer of the structure (3.642 Å). With these values f was calculated for each composition and the surface mole fraction calculated from $X_{s,m}$, using the equations above. The surface fractions calculated in this way are also shown in Figure 6.7.

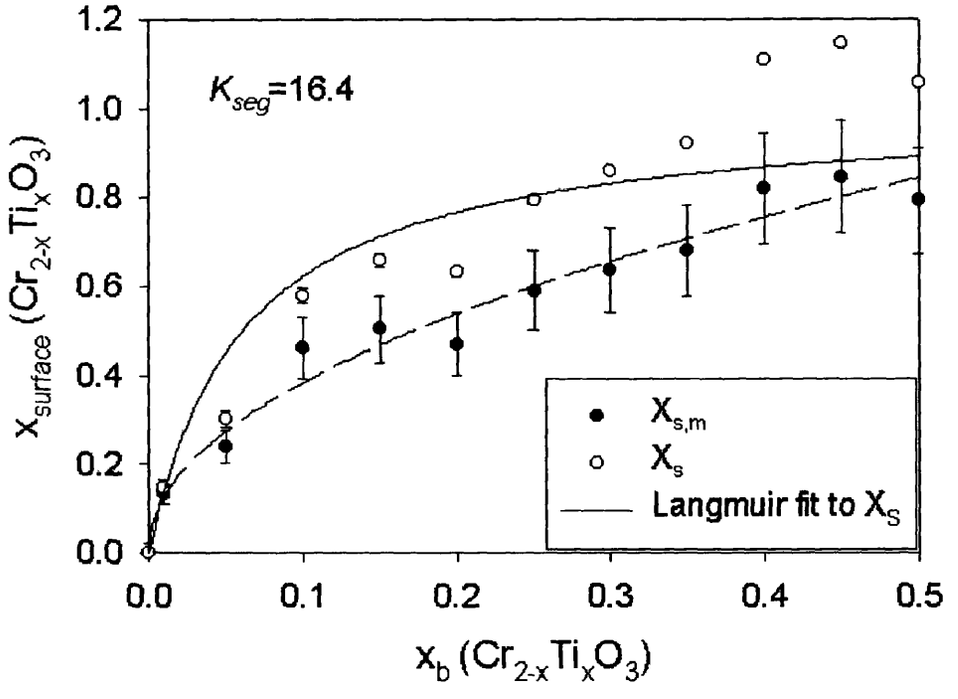

Figure 6.7 Surface segregation of titanium in Cr_2O_3

A reasonable assumption for x_s is that the surface tends to the composition $CrTiO_3$; i.e. X_s=0.5. (x=1 in $Cr_{2-x}Ti_xO_3$). With this assumption the calculated X_s values were fitted to the Langmuir equation. A Gibbs free energy for segregation ΔG_{seg} of –29.6 kJ*mol^{-1} was be calculated from the equilibrium constant K, obtained from the Langmuir fit.

$$K = \exp\left(\frac{-\Delta G_{seg}}{RT}\right) \qquad (6.8)$$

where T is the temperature of preparation (1273.15 K) and R is the gas constant.

6.5 Discussion

The effects of titanium substitution in the Cr_2O_3 lattice have been investigated by XP spectroscopy. A considerable surface segregation of titanium was shown, confirming the computational simulations in chapter 4. XPS also showed a strong decrease in Cr^{VI} states with increasing titanium concentration (Figure 6.4), as predicted in our model.

XP spectroscopy of chromium oxide shows the same Cr 2p splitting that was observed by Tsurkan and Plogmann [61] for the case of ternary chromium sulphides and selenides. We observed the same magnitude of approximately 1.0 eV. It indicates that the contribution of neighbouring atoms to the splitting is small. Molecular calculations carried out by Kaltsoyannis [67] support this interpretation. Evidence that the splitting originates simply by interaction between the 2p core and the d electron of the same Cr atom can be derived by the fact that the Ti^{IV} core spectrum (d^0 system) does not show such a splitting. Plogmann *et. al.* [63] observed a direct correlation between the magnitude of the splitting and the local magnetic moment at the Cr site. According to this correlation a splitting between 0.95 and 1.0 eV results from a local magnetic moment of about 2.9-3.0 μB.

Whilst the magnitude of the splitting stayed constant for all the investigated samples the peak shape varied significantly with titanium concentration. The blurring of the lines caused by Ti substitution could then be explained by the deformation of the Cr environment near to the Ti, revealed by the computational modelling. Etching results in roughening of the initially well sintered surface, leading also to deformation of the Cr environment. The

reappearance of the splitting at higher Ti concentration could then be attributed speculatively to ordering of the surface structure. However, this interpretation is not unambiguous since there is also a variation in the signal due to high-valent Cr that overlaps the Cr^{III} signals and causes an apparent broadening of the XP lines.

The surface segregation of titanium onto the Cr_2O_3 that was predicted by computational modelling is confirmed. It can be assumed that the surface tends to the composition $CrTiO_3$. The computed segregation energy is the enthalpy of segregation at 0K and is significantly larger than the Gibbs energy of segregation deduced from the composition dependence of surface composition (Figure 6.7). Since vibrational and configurational contributions to the segregation enthalpy and entropy are generally fairly small [68], we attribute the difference to the difference between segregation enthalpy at very low defect concentration (determined by the computational method) and that at rather high defect concentration (determined experimentally). The experimental evidence that the measured mole fraction of Cr^{VI} decreased markedly with small Ti substitution but then remained constant we can interpret by proposing that Ti displaces Cr^{VI} from the top surface layer but that the Cr^{VI} - V_{Cr} defect remains segregated to the immediate sub-surface layers. A detailed description of the electrical behaviour would therefore have to take into account the contribution of these sub-surface acceptor states.

6.6 Summary

The Cr $2p_{3/2}$ states show a multiplet splitting, originating from local magnetic moments at the Cr site. The splitting showed a constant magnitude of about 1 eV for all investigated CTO samples. Distortion of the Cr environment by titanium caused blurring of the peak shape. However, the splitting was restored with further increasing titanium concentration. It is speculated that this is due to ordering of the surface. XPS analysis revealed a strong surface segregation of Ti^{IV} states. It can be assumed that the surface tends to the composition $CrTiO_3$.

7 Gas response of semiconducting oxides in a nitrogen atmosphere

7.1 Introduction

Many reports in the literature have dealt with the capacity of semiconducting oxides to detect traces of reactive gases in air. It is widely agreed that oxygen plays a crucial part in the gas detection.[69] The gas detection is registered by variations in electrical conductivity in the presence of a reacting gas. The conductivity of the sensors is dependent upon the coverage of surface acceptor states (O^{2-}). Variation of those acceptor states can be achieved either by exposure of the sensor to a reacting gas (gas detection) or by alteration of the oxygen partial pressure.

Because oxygen has such a key role the range of uses for semiconducting oxides has so far been restricted to air containing environments. In order to get a more detailed view of the oxygen dependence we tested the gas response of CTO in a nitrogen atmosphere. Chromium titanium oxide (CTO) was chosen as semiconducting oxide and hydrogen sulphide, ethanol and carbon monoxide were chosen as reacting gases.

7.2 Experimental

The gas response to H_2S gas was carried out in a rig through which the gases were allowed to flow horizontally. The cell was exposed to pure nitrogen gas for twelve hours in order to remove oxygen and to achieve a stable baseline resistance. The target gas concentration was controlled by manual mass flow controllers and the resistivity of the sensor was monitored by a Beckman industrial autoranging multimeter. Multimeters, which apply up to 2V across the sensor, can sometimes cause a baseline drift. In order to minimise this problem the multimeter was connected to the sensor only for the short time when the reading was taken. The time was recorded by using a stopwatch. The gas response to carbon monoxide and ethanol in a nitrogen atmosphere was tested in the same way. A similar gas rig was chosen to carry out these experiments. Prior to each experiment the cell was exposed to pure nitrogen for twelve hours in order to remove any traces of oxygen.

7.3 Results

7.3.1 Electrical behaviour

The change in conductivity with oxygen partial pressure is illustrated in Figure 7.1. P–type conductivity is observed at all oxygen partial pressures. At low oxygen partial pressures the baseline stabilised only slowly. The conductivity dependence on the oxygen partial pressure $\sigma \approx P_{O2}^{1/4}$ as reported by Holt and Kofstad [48] was confirmed

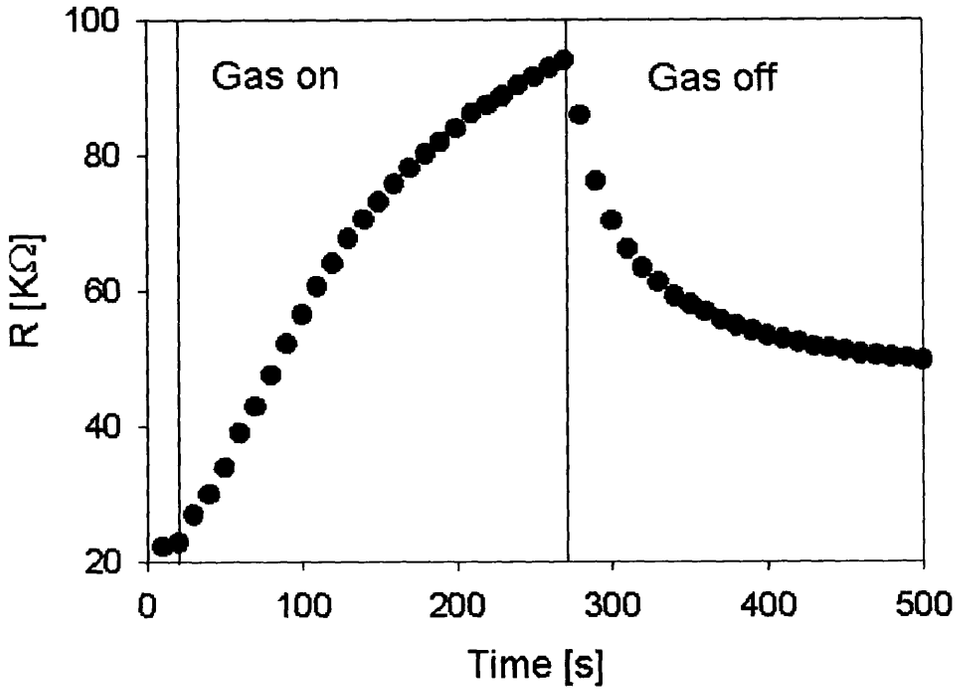

Figure 7.4 Response to 5 ppm of H_2S in N_2 at 530°C.

Exposure to 5 ppm of H_2S at 530°C operating temperature showed a smaller and more rapid gas response. (Figure 7.4). A baseline shift of 100% was observed after the pulse of H_2S.

7.3.3 Long term exposure to H_2S

The gas sensor was constantly exposed to 6 ppm of H_2S in N_2 for eight hours in order to study the long–term exposure to H_2S. (Figure 7.5 and 7.6) It is noted that the surface of the sensor had already been conditioned by H_2S during previous experiments. The experiment was repeated twice. The results obtained for the last experiment are incomplete because of a failure of the gas supply.

Figure 7.5 illustrates that the sensor showed a stable gas response over eight hours. The measurements taken on the second and third day showed a similar behaviour after approximately three hours. A slight increase in resistance is observed, possibly arising from some further conditioning of the surface.

Figure 7.6 magnifies the first 200 minutes of each experiment. The behaviour of resistance over time is divided into two phases. The timescale for the initial response is similar in all three cases

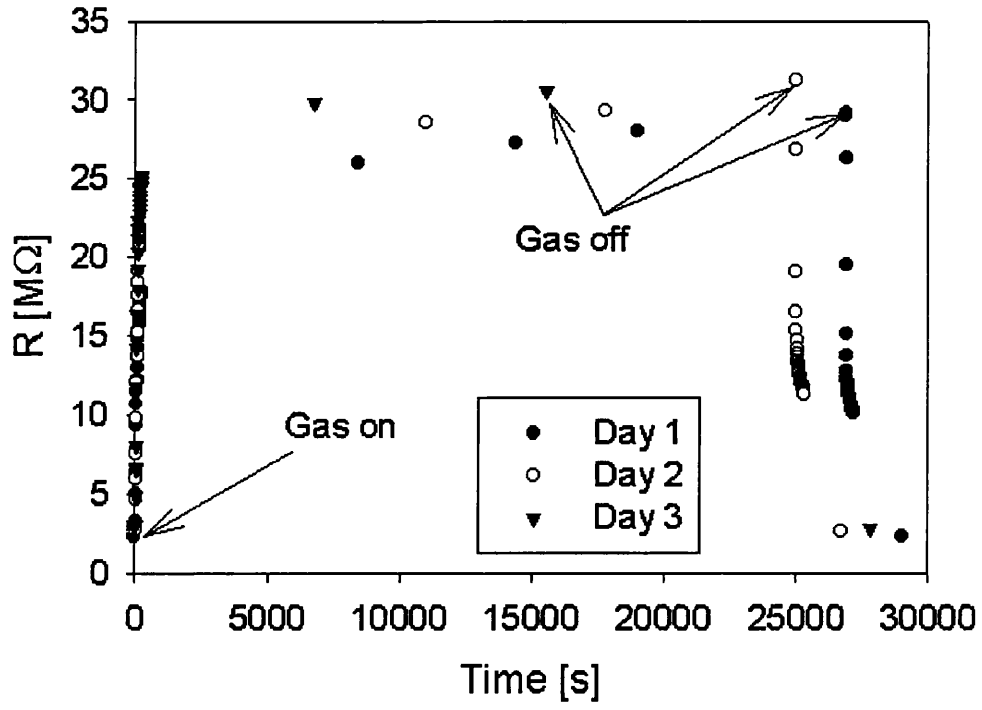

Figure 7.5 Long term exposure to 6 ppm H_2S in N_2 at 453°C

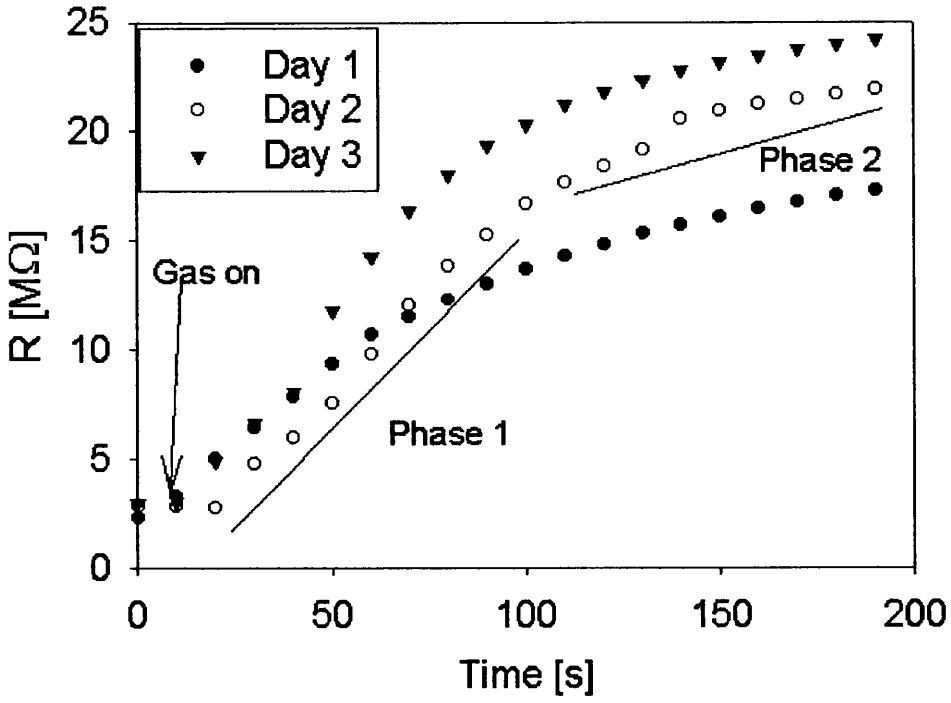

Figure 7.6 Magnification from Figure 7.5 of the first 200 seconds of the response to 6 ppm H_2S in N_2 on each of three successive days.

7.3.4 Gas response to carbon monoxide and ethanol

Figure 7.7 and 7.8 show the dependence of the response to 200 ppm of ethanol and 100 ppm of carbon dioxide on the oxygen partial pressure. It is observed that the gas response, like the resistivity, increased significantly with decreasing oxygen partial pressure. Experiments carried out at a higher operating temperature showed the same results. The gas response was however significantly decreased at the higher temperature. It is noted that CTO did show a response to both ethanol and carbon monoxide in nitrogen gas.

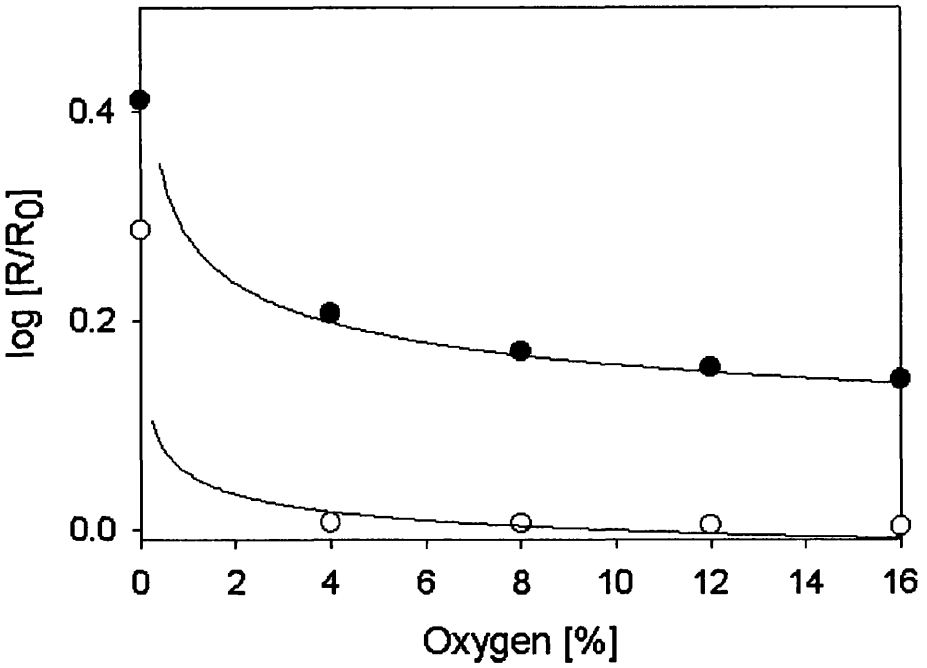

Figure 7.7 Response to 200 ppm of carbon monoxide at 400°C (black dots) and 530°C (white dots) The fitted curve is $R/R_0 \approx P_{O2}^{-1/4}$. R_0 denotes the resistance in the reduced oxygen partial pressure in the absence of gas.

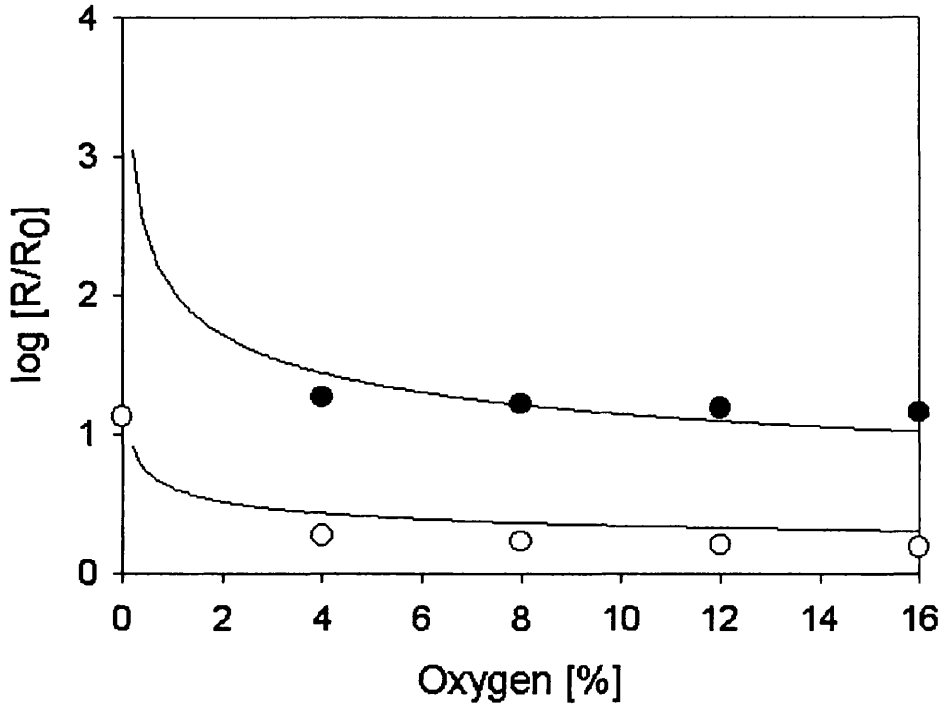

Figure 7.8 Response to 100 ppm of ethanol at 400°C (black dots) and 530°C (white dots) The fitted curve is $R/R_0 \approx P_{O2}^{-1/4}$. R_0 denotes the resistance in the reduced oxygen partial pressure in the absence of gas.

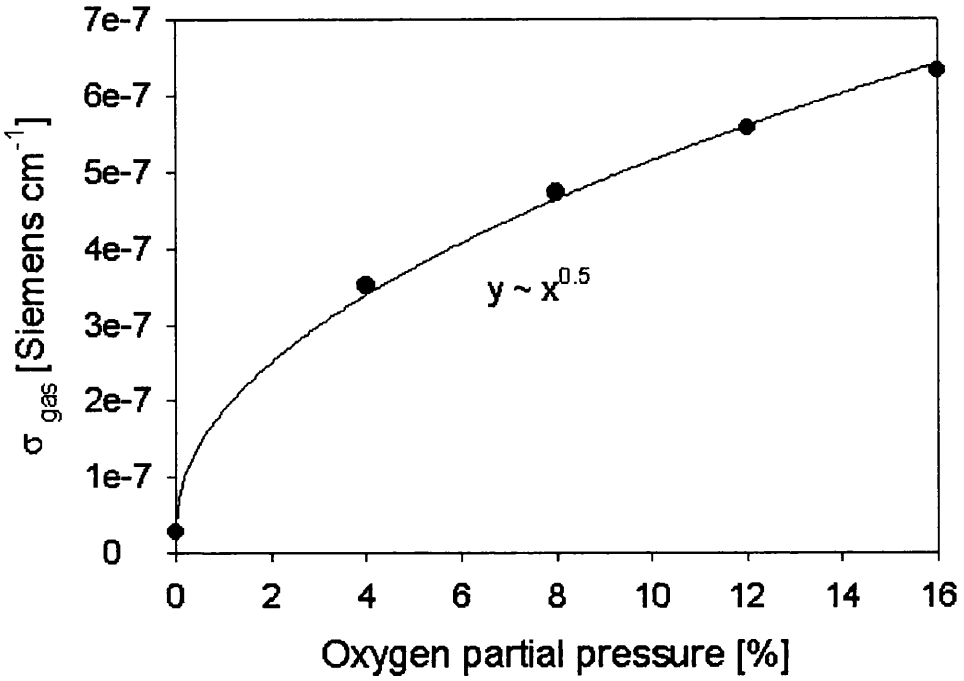

Figure 7.9 Conductivity of the sensor in the presence of 100 ppm carbon monoxide at 300 °C.

7.4 Discussion:

The literature on semiconducting oxides as sensors for reactive gases at low concentration invariably assumes that oxygen must be present in the gas phase. The response mechanism is generally formulated as a reaction with the target gas of electrically active surface states, assumed to be associated with the adsorption of oxygen. With this background, the observation of responses to trace gases in nitrogen is somewhat unexpected. The previous literature is based on discussions of observations pertinent to tin dioxide as the sensor material. In this discussion therefore, the differences between CTO and SnO_2, which might result in the observed response of CTO in a nitrogen atmosphere, are highlighted.

7.4.1 Electrical behaviour

The large decline in conductivity of CTO with decreasing oxygen partial pressure has been observed before. Henshaw *et. al.* [45] studying highly porous bodies similar in microstructure to the devices studied in the present work, attributed this effect to the decline of adsorbed oxygen species, which acted as surface acceptor states. Since the charge transfer to these states is reported to be predominantly from the Cr d states in the bandgap the surface acceptor states could also be described as Cr^{VI} (CrO_3) species; p–type conductivity was observed at all oxygen partial pressures.

Holt and Kofstad [48] studied dense specimens and suggested a change from p to n – type conductivity at 1000°C and low oxygen partial pressure. Such a change in sign of majority charge carrier is common for semiconducting oxides and arises because electrons and holes are generated equally by band-gap excitation but one of the carriers (that which is normally the majority carrier) is trapped in gap states associated with lattice defects. Both authors agree that the predominant lattice defects are chromium vacancies. The significant difference between CTO and SnO_2 is that CTO is much more difficult to reduce.

7.4.2 H_2S gas adsorption and response model

Henshaw *et. al.*[45] studied the gas response of CTO to H_2S in air. They reported the formation of a surface sulphate detected by XP spectroscopy. Temperature programmed desorption experiments carried out in vacuum showed the presence of SO_2 in the first cycle. Adsorption of a second pulse of H_2S in vacuum followed by TPD did not show any more traces of SO_2 only H_2S desorbed from the second exposure. The authors attributed the

desorption of SO_2 in the first cycle to the reaction of this gas with surface adsorbed oxygen present as a consequence of the previous exposure of the oxide to air. When these species had been removed, then H_2S was molecularly adsorbed only. A permanent baseline resistance increase on first exposure to H_2S in air, reversible by heating to sufficiently high temperature, was attributed to the surface sulphation: the surface sulphate species were assumed to act as hole traps.

According to these observations the permanent baseline shift observed in the experiments in nitrogen reported here could also be attributed to conditioning of the surface by sulphate species. The assumption is that the oxygen partial pressure in the nitrogen ambient was sufficient to oxygenate the surface. Thus, as mentioned in the chapter 4 the surface of CTO is covered by chemisorbed oxygen species, which form Cr^{VI} (CrO_3). The assumption, based on the fact that the behaviour is stable over an extended time and consistent with the high oxygen affinity of the chromium oxide surface, is that those species are still present at significant surface coverage at low oxygen partial pressure. Contact with H_2S would result in a reduction to Cr^{III} (Cr_2O_3), which is conveniently formally expressed as reaction (7.1).

$$2CrO_3 + H_2S \rightleftharpoons Cr_2O_3 + SO_2 + H_2O \qquad (7.1)$$

The water that is also formed in this reaction could either be released into the atmosphere or hydroxylation of the surface could take place. Reaction of the sulphur dioxide with other Cr^{VI} species would lead to formation of the chromium sulphate species that have been detected by XPS by Henshaw [45]. The reverse of the reaction by heating of the sample can be expressed as reaction (7.2).

$$2CrO_3 + 3SO_2 \rightleftharpoons Cr_2(SO_4)_3 \quad (7.2)$$

The quicker response curve observed in the second pulse of H_2S also mirrors the behaviour observed in air. Following the conditioning of the surface, it is concluded that the gas response is caused by adsorption of H_2S on the Cr^{III} sites, forming a new surface acceptor state. The conductivity is now dominated by the concentration of these species; expressed as reaction (7.3)

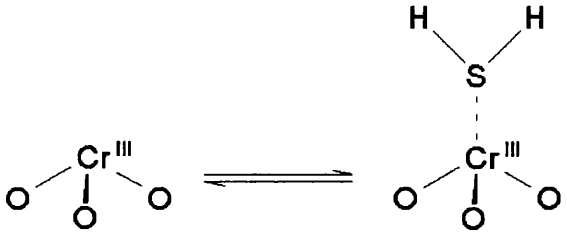

(7.3)

7.4.3 Variation of the response to carbon monoxide and ethanol with oxygen partial pressure.

The change of gas response with oxygen partial pressure obeys the same power law as the variation of baseline resistivity with oxygen partial pressure. The concentration of oxygen surface acceptor states correlates the resistivity and the gas response such that a high resistivity caused by a low oxygen concentration leads to a high gas response. The high gas response that was observed in pure nitrogen indicates the presence of a relatively small number of oxygen states. These oxygen states were removed by the gas response to ethanol / CO, but the baseline recovery after the gas response indicated that the surface acceptor states must have been restored. Hence it can be speculated that a small number of oxygen molecules was still present in the gas flow.

The facts to be addressed by a formal model are:

- the variation $\sigma \sim P_{O2}^{1/2}$ in the presence of a sufficient concentration of a reactive gas (Figure 7.9)
- the variation of $\sigma \sim P_{O2}^{1/4}$ in the absence of a reactive gas. The variation is consistent with that reported in the literature ($\sigma \sim P_{O2}^{0.36}$ at 250°C decreasing to $\sigma \sim P_{O2}^{0.10}$ at 450°C. [45]
- the variation of response, as resistivity referenced to resistivity in the absence of gas but at the same oxygen partial pressure, $P/P_0 \sim P_O^{-1/4}$. (Fig. 7.7+7.8)

A rather simple model can be set up to describe the behaviour of a p-type oxide. At the surface, an accumulation layer of holes is developed by charge exchange with surface oxygen species. There is also the evidence adduced in earlier chapters that Cr^{VI} is segregated to the surface or near sub-surface, giving a near-surface increase in concentration of acceptor states and thus contributing a distinct 'surface' element to this conductivity. Thus one can expect the conductivity as two parallel elements, one representing the surface zone (including the immediate sub-surface) and the other the 'bulk':

$$\sigma = \sigma_s + \sigma_b \qquad (7.4)$$

Here σ_s itself has two components, one due to the charge exchange with surface oxygen states and the other due to the lattice acceptor states, associated with Cr^{VI}. The element σ_s is gas-sensitive whilst σ_b is not.

The effects of microstructure on response, where the conductance is split into a 'surface' and a 'bulk' part as in equation (7.4) has been considered by Williams and Pratt [7]. These authors showed that a response approximately $\sigma \sim P_{gas}^{-1/2}$ was obtained from a p-type material if $\sigma_s \sim P_{gas}^{-1}$ A signal could be obtained even if σ_s was rather small in comparison with σ_b.

The mechanism embodied in scheme 1 of chapter 4 can be written as follows where S denotes the surface site.

$$S + O_2 \xleftarrow{K_1} [S\cdots O_2] \underset{k_{-1}}{\overset{k_1}{\rightleftharpoons}} [S\cdots O,O] \quad (7.5)$$

$$[S\cdots O,O] + CO \xrightarrow[k_2]{} [S\cdots O] + CO_2 \quad (7.6)$$

$$[S\cdots O] + CO \xrightarrow[k_3]{} S + CO_2 \quad (7.7)$$

$[S\cdots O,O]$ denotes a dissociated oxygen state. The surface oxygen state, the near-surface acceptor state (Cr^{VI}, represented as A^{3+}) and valence band holes will be in electronic equilibrium.

$$[S\cdots O,O] \xleftarrow{K_4} [S\cdots O,O]^- + p^* \quad (7.8)$$

$$A^{3+} + [S\cdots O,O]^- \xleftarrow{K_5} A^{2+} + [S\cdots O,O] \quad (7.9)$$

From equation (5), $[p^*]_s = \left(K_4 \times \frac{[S\cdots O,O]}{[S\cdots O,O]^-} \right)$ (7.10)

and the charge balance is:

$$[S\cdots O,O]^- = [p^*]_s + [A^{2+}] + [A^{3+}] \quad (7.11)$$

and the mass balance is $[A^{2+}] + [A^{3+}] = \text{constant}$

The experimental evidence is that A^{3+} is relatively high. So assuming that $[A^{2+}] + [A^{3+}] >> [p^*]_s$, then

$$[S\cdots O,O]^- \cong [A^{2+}] + [A^{3+}] = \text{constant} \quad (7.12)$$

Thus from equation (7), $[p^*]_s \propto [S\cdots O,O]$ (7.13)

Now from equation (7.5) + (7.6)

$$k_1 \times K_1 \times P_{(O_2)} = k_{-1}[\mathrm{S}\cdots\mathrm{O,O}] + k_2 P_{(CO)}[\mathrm{S}\cdots\mathrm{O,O}]$$
$$= [\mathrm{S}\cdots\mathrm{O,O}](k_{-1} + k_2 P_{(CO)})$$

Furthermore

$$(\mathrm{S}) + [\mathrm{S}\cdots\mathrm{O}_2] + [\mathrm{S}\cdots\mathrm{O,O}] + [\mathrm{S}\cdots\mathrm{O}] = \text{constant} \approx (\mathrm{S})$$

Therefore

$$[\mathrm{S}\cdots\mathrm{O,O}] = \frac{k_1 K_1 (\mathrm{S}) P_{(O_2)}}{k_{-1} + k_2 P_{(CO)}} \qquad (7.14)$$

i.e.

$$\sigma_s \propto [\mathrm{p}^*]_s \propto \frac{k_1 K_1 (\mathrm{S}) P_{(O_2)}}{k_{-1} + k_2 P_{(CO)}} \qquad (7.15)$$

Thus, if $k_2 P_{(CO)} >> k_{-1}, \sigma_s \propto \left(\frac{P_{(O_2)}}{P_{(CO)}}\right)^{+1}$ (7.16)

Therefore taking into account the effects of the microstructure as expressed through equation 1 the result of Figure 7.9 is explained with $P_{(CO)}$ constant, $\sigma_s \propto P_{(O_2)}{}^{+1}$, so $\sigma = \sigma_s + \sigma_b \propto P_{(O_2)}{}^{+1/2}$ and with $P_{(O2)}$ constant $\sigma_s \propto P_{(CO)}{}^{-1}$, so $\sigma \propto P_{(CO)}^{-1/2}$, as shown earlier.

The results in Figure 7.9 can now be explained. The resistance in the presence of gas varies as

$$R \propto P_{(O_2)}^{-1/2}, P_{(CO)}^{1/2}$$

The baseline resistance (from Figure 7.1) varies as $R_0 \propto P_{(O_2)}{}^{-1/4}$. Therefore the ratio $R/R_0 \sim P_{(CO)}{}^{1/2} P_{(O2)}{}^{-1/2} P_{(O2)}{}^{1/4} = P_{(O2)}{}^{-1/4}$ at fixed $P_{(CO)}$, as it is observed (Fig.7.7). To explain the result of Figure 7.1 requires a more detailed consideration of the reaction scheme. Firstly suppose that the state $[\mathrm{S}\cdots\mathrm{O,O}]$ will trap <u>two</u> electrons. Then, following arguments similar to those above, in the absence of CO, one has $[\mathrm{p}^*]_s \propto [\mathrm{S}\cdots\mathrm{O,O}]^{+1/2}$, and hence

$\sigma_s \propto [p^*]_s \propto P_{(O_2)}^{+1/2}$. Therefore in view of the effects of the microstructure, *(equ.1)* $\sigma \propto P_{(O_2)}^{+1/4}$, which is what is observed. To explain the behaviour in the presence of CO with $\sigma_s \propto P_{(O_2)}^{1}$ requires the postulate that reaction (3) is fast.

$k_2 P_{(CO)}[S\cdots O,O] >> k_{-1}[S\cdots O,O]$ and $k_3 P_{(CO)}[S\cdots O]$

Thus in the presence of CO, $[S\cdots O] >> [S\cdots O,O]$. If $[S\cdots O]$ is a one electron trap state then the arguments leading to equation (10) can be repeated, giving $[p^*]_s \propto [S\cdots O]^{+1}$ and $[S\cdots O] \propto P_{(O_2)}$. Hence:

$\sigma_s \propto P_{(O_2)}^{1}$ and $\sigma \propto P_{(O_2)}^{1/2}$ in the presence of CO, as it is observed.

7.5 Summary

The response of CTO to H_2S in nitrogen is considerable. Therefore, this new technique could be successfully applied to the monitoring of H_2S in oil pipes. A consistent and simple description of interaction of H_2S with the surface has been given and related also in some detail to the effect of the gas on the electrical resistivity of the material. The gas response to CO and ethanol varied significantly with oxygen partial pressure: The conductivity in the presence of carbon monoxide was fitted to $P_{(O2)}^{1/2}$. The baseline conductivity varied as $P_{(O2)}^{1/4}$ and the gas response, expressed as the ratio of resistance in the presence or absence of gas at a particular oxygen partial pressure, varied as $P_{(O2)}^{-1/4}$. A model has been developed, based on a reaction scheme given in Chapter 4, which explains the observations.

8 CO and water response of Chromium oxide doped with transition metal cations in addition to titanium

8.1 Introduction

It has been demonstrated in the previous chapters that the addition of small amounts of titanium to Cr_2O_3 has led to a new material that is sensitive to small amounts of carbon monoxide. This gas response is due to surface reaction of CO to CO_2. The sensor signal was shown to develop because titanium was surface segregated and hence removed the acceptor state near the surface which were associated with Cr^{VI}, thus allowing effects of variation of surface concentration of oxygen species to be revealed. It was also speculated that surface Ti provides a binding site for water vapour adsorption whereas the Cr vacancies and surface Cr atoms mediated the response to carbon monoxide. In this chapter Cr_2O_3 was doped with other 3-d elements adjacent to titanium in the periodic table. They all form stable oxides and provide therefore interesting additives to chromium oxide. In principle surface segregation of these cations should occur and their ionic radius is not so different, from that of Cr^{III}, that solid solution might be achieved. However, the interaction with water vapour should be different to that of titanium. Dusastre *et.al.*[70] showed recently that a change of cation could significantly change the effects of water vapour. Apart from those 3-d transition metal oxides described below MgO was chosen as well in order to study the influence of a small defect cation with only one stable oxidation state (+II). The metal oxides that were chosen are displayed in Table 8.1.

Table 8.1 Elements that have been chosen, their most stable oxidation states and their ionic radii. hs = high spin ls = low spin

Element	Stable oxidation states	Ionic radius [pm]
Titanium	+IV	60
Vanadium	+III / + V	64 / 54
Chromium	+III/ +VI	61/ 44
Manganese	+II /+III / +IV / +VII	83hs 67ls / 64hs 58ls /53 /46
Iron	+II / +III	78hs 61ls / 64hs 55ls
Magnesium	+II	72

Cr^{III} and Ti^{IV} have very similar ionic radii (Table 8.1). It is argued that due to this similarity Cr^{III} could easily be substituted by Ti^{IV}. The only elements with similar ionic radii are V^{III} (64 pm), Fe^{III} high spin (64 pm) and Mn^{III} (64 pm hs 58 pm ls).

8.2 Preparation method

Cr_2O_3 prepared by decomposition of ammonium dichromate was dispersed in propan-2–ol, along with the required amount of the second oxide. Table 8.2 gives a list of the oxides that were added and the powders that were finally obtained. After being ball–milled for 12 hours the solvent was evaporated. The powders were fired overnight in recrystallised alumina crucibles at 1000°C and subsequently pressed into pellets of 13 mm diameter and 5 mm thickness.

Table 8.2 Ternary compositions prepared

Oxide chosen	**Composition prepared**
TiO_2 *	$Cr_{1.8}Ti_{0.2}O_3$
V_2O_5	$Cr_{1.8}V_{0.2}O_3$
Cr_2O_3	Cr_2O_3
MnO_2	$Cr_{1.8}Mn_{0.2}O_3$
Fe_2O_3	$Cr_{1.8}Fe_{0.2}O_3$
MgO	$Cr_{1.8}Mg_{0.2}O_3$

* has been obtained in the flask by reaction of a titanium isopropoxide precursor and water. Details of the preparation method have been described in chapter 2.

Table 8.2 gives a list of the oxides that were added to the dispersed Cr_2O_3 powder in propane–2–ol. $Cr_{1.8}Ti_{0.2}O_3$ has been arbitrarily chosen as a standard with which the other materials have been compared. To allow a better comparison all the powders were prepared with the composition $Cr_{1.8}X_{0.2}O_3$. However, it should be not implied by this formula, that the compounds form a solid solution.

8.3 Results

8.3.1 Phase characterisation

X–ray powder diffractometry (Figure 8.1–8.3) revealed a Cr_2O_3 corundum phase in all investigated samples, which are indexed. The other peaks observed in the patterns belong to impurity phases, which have been identified and listed in Table 8.3. Chromium vanadium oxide did not show any impurity phases, however. A vanadium rich corundum phase ($V_{2-x}Cr_xO_3$) has been reported in the literature.[71] XPS did not show any trace of substituted ions on the surface, (with the exception of titanium, see chapter 6), which indicates either that none of the impurity atoms has dissolved into the lattice, or that they show inverse segregation. The impurities reduced the average crystallite size by 20-40%. A small increase in lattice parameter size was observed in some samples. (Table 8.4)

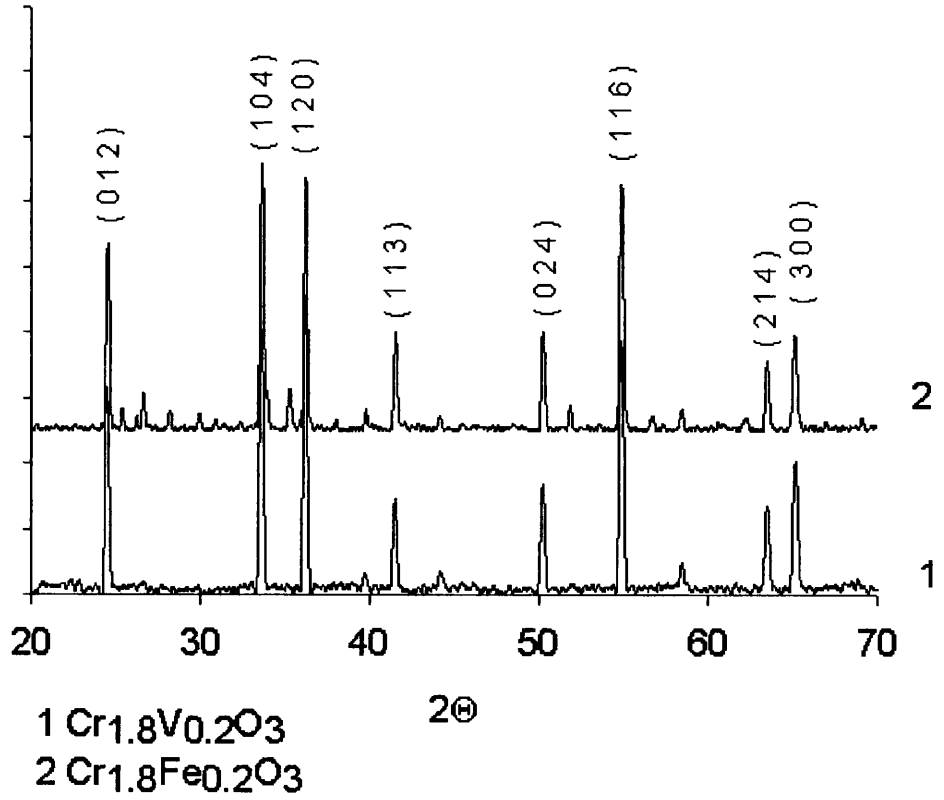

Figure 8.1 X-ray powder diffraction patterns of Chromium vanadium oxide and chromium iron oxide.

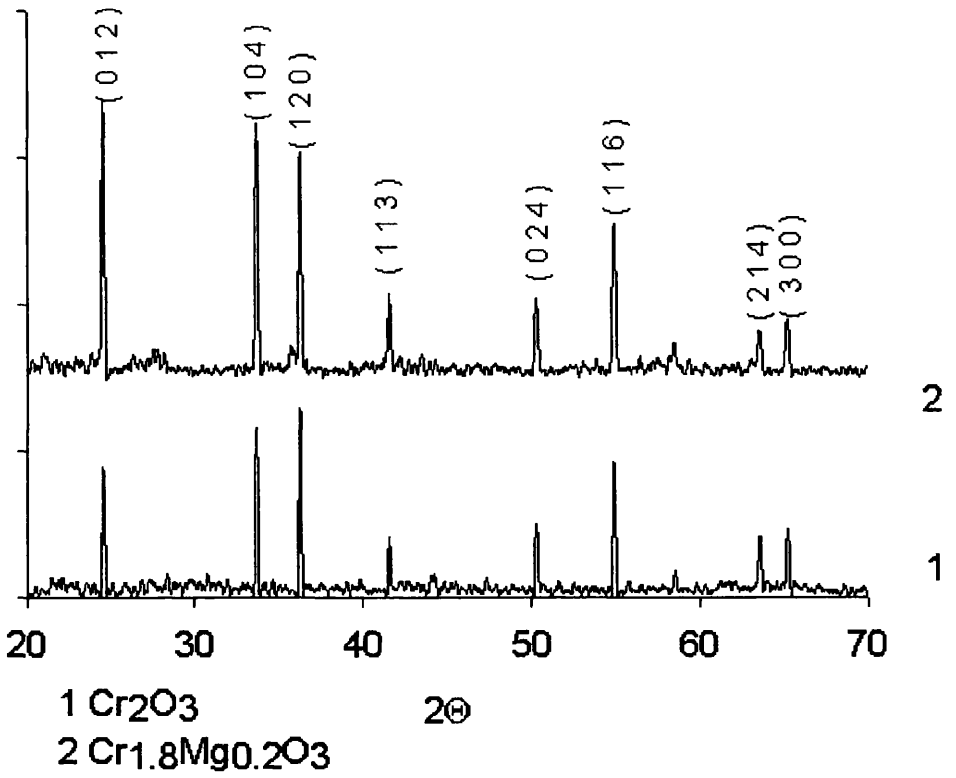

Figure 8.2 X-ray powder diffraction patterns of Cr_2O_3 and Chromium magnesium oxide.

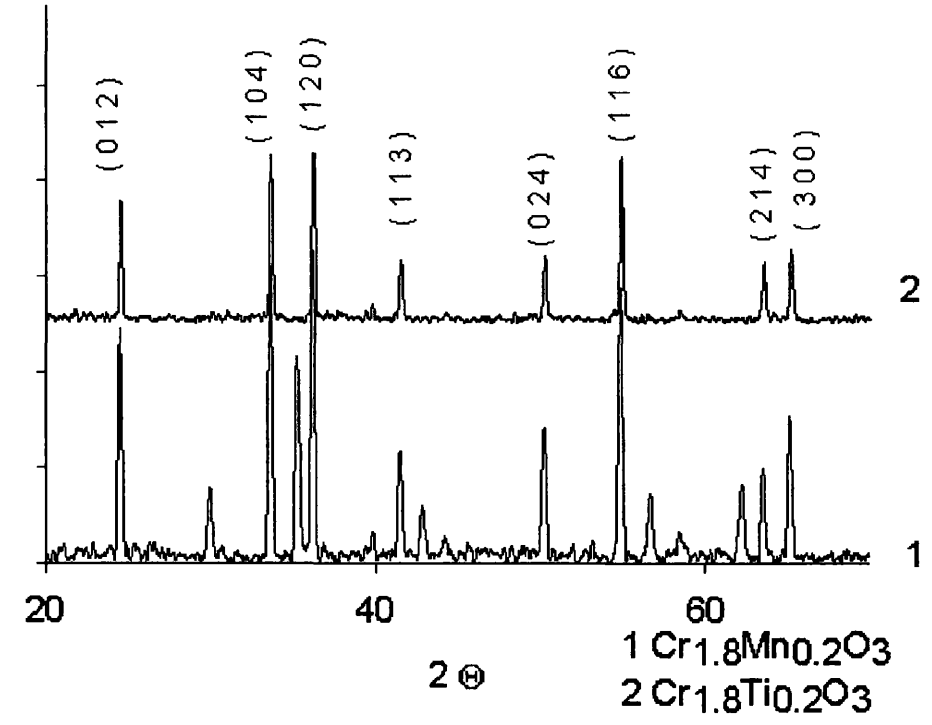

Figure 8.3 X-ray powder diffraction patterns of chromium manganese oxide and chromium titanium oxide

Table 8.3 Investigation of the impurity phases

Impurity cation	**Identified phase**
TiO_2 *	$Cr_{2-x}Ti_xO_3$
V_2O_3	$V_{2-x}Cr_xO_3$*
MnO_2	$MnCr_2O_4$
Fe_2O_3	$(Fe_{0.6}Cr_{0.4})_2O_3$ **
MgO	$MgCr_2O_4$

* vanadium rich impurity phase

** isostructural to α- Fe_2O_3, as reported by Music *et.al.* [72]

Table 8.4 XRD characterisation of the powders

Nominal Composition	**A [Å]**	**C[Å]**	**Cell size[Å^3]**	**Av. Cryst. size [Å]**
$Cr_{1.8}Mg_{0.2}O_3$	4.96	13.49	288.03	400
$Cr_{1.8}Ti_{0.2}O_3$	4.96	13.48	288.05	400
Cr_2O_3	4.96	13.50	288.02	500
$Cr_{1.8}Mn_{0.2}O_3$	4.97	13.54	290.34	430
$Cr_{1.8}Fe_{0.2}O_3$	4.97	13.53	289.64	400
$Cr_{1.8}V_{0.2}O_3$	4.98	13.55	290.37	320

8.3.2 Electrical behaviour

Magnesium was the only substituent that decreased the resistivity of Cr_2O_3: by 80%. (Table 8.5) Manganese and iron enhanced the resistivity by a factor of 4 and 7 times, respectively. Chromium vanadium oxide showed an increased resistivity by a factor of more than 10 and titanium increased the resistivity of Cr_2O_3 by about 100 times, as previously noted in Chapter 5. The changes in resistivity and the change in crystallite size imply at least some substitution of the additives into the Cr_2O_3 lattice.

8. Response of Cr_2O_3 doped with cations in addition to Ti

The activation energy for conductivity was marginally reduced by iron and magnesium and marginally increased by manganese. Titanium was the only defect material that altered the activation energy significantly.

Table 8.5 Resistivity at 350°C

Compound	Resistivity at 350°C[KΩ cm]	$\frac{R_{Compound}}{R_{Cr2O3}}$
$Cr_{1.8}Mg_{0.2}O_3$	1.7	0.2
$Cr_{1.8}Ti_{0.2}O_3$	664.3	69.9
$Cr_{1.8}V_{0.2}O_3$	126.7	13.2
Cr_2O_3	9.5	1
$Cr_{1.8}Mn_{0.2}O_3$	63.8	6.6
$Cr_{1.8}Fe_{0.2}O_3$	40.0	4.2

Table 8.6 Activation energy for conductivity for the prepared compounds

Compound	E_A [eV]
$Cr_{1.8}Mg_{0.2}O_3$	0.42
$Cr_{1.8}Ti_{0.2}O_3$	0.82
$Cr_{1.8}V_{0.2}O_3$	0.51
Cr_2O_3	0.49
$Cr_{1.8}Mn_{0.2}O_3$	0.54
$Cr_{1.8}Fe_{0.2}O_3$	0.42

8.3.3 Gas response to carbon monoxide

Apart from chromium vanadium oxide (CVO) every sample showed a gas response to carbon monoxide. Chromium iron oxide (CFO) and chromium titanium oxide (CTO) show a significantly improved gas response with respect to Cr_2O_3, chromium manganese oxide (CMO) and chromium magnesium oxide (CMgO) showed a very similar response to Cr_2O_3. Chromium iron oxide has a particular good gas response at high temperatures (Fig. 8.4). The square root dependence of the gas response to the target gas concentration has been observed for all the doped samples. (Fig. 8.5)

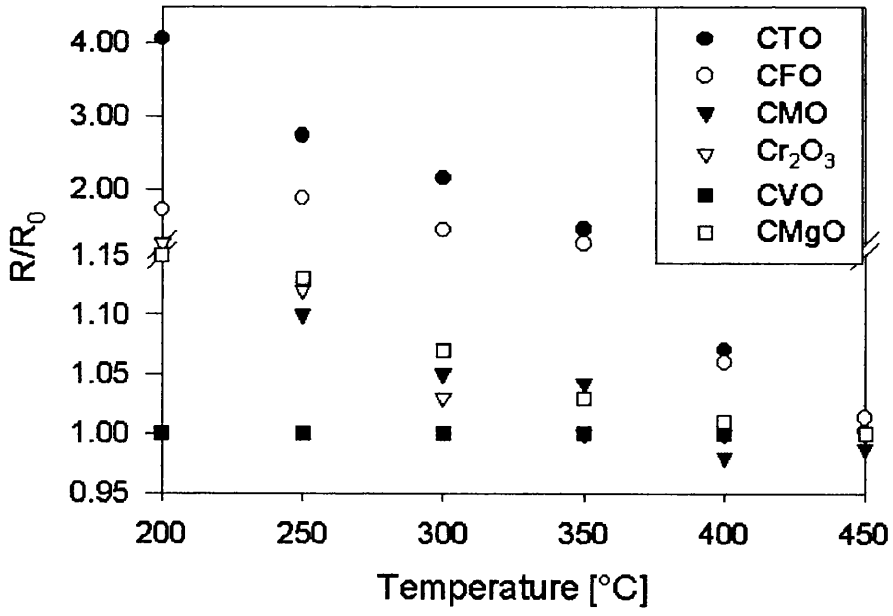

Figure 8.4 Response to 500 ppm of CO

Chromium titanium oxide had the highest response to water vapour (Figure 8.6). The other doped chromium oxide samples showed only a small response to water vapour. $Cr_{1.8}Mg_{0.2}O_3$, $Cr_{1.8}V_{0.2}O_3$, and Cr_2O_3 are not displayed in Figure 8.6 because they showed no water vapour response ($R/R_0=1$)

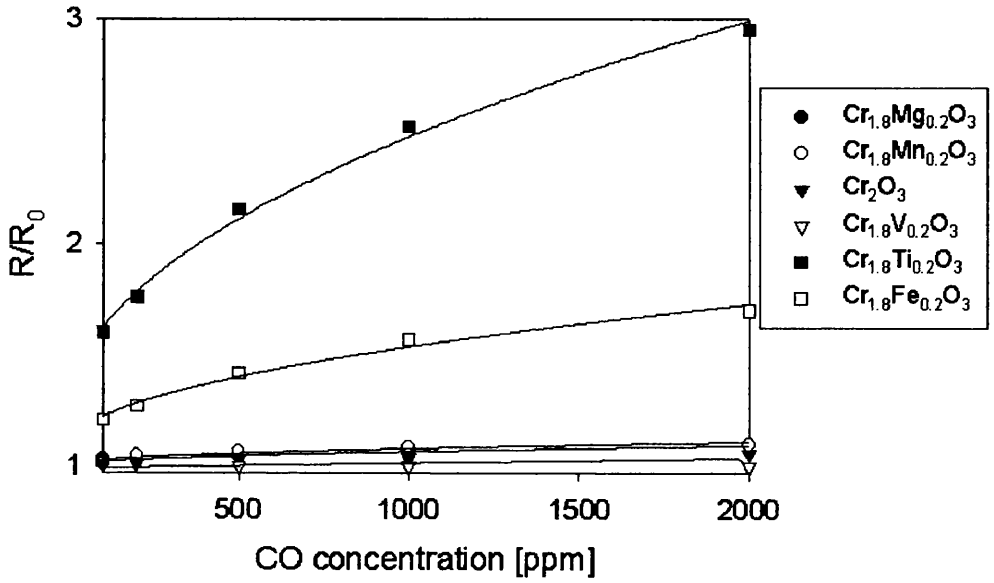

Figure 8.5 Response to carbon monoxide at 300°C

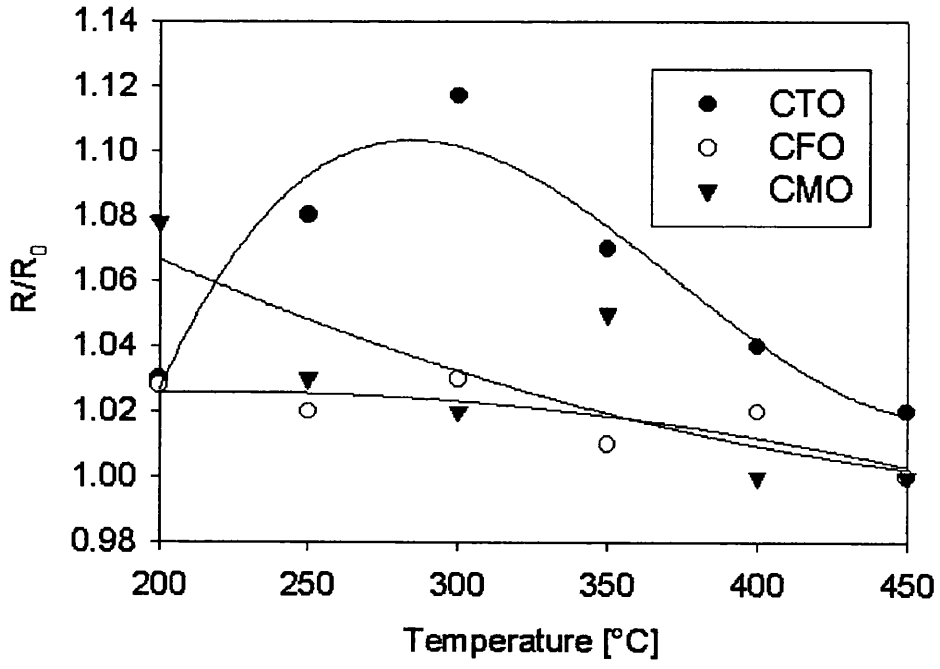

Figure 8.6 Response to 100% relative humidity at RT

8.4 Discussion

The ionic radii of Ti^{IV} (60 pm) and Cr^{III} (61 pm) are very similar, resulting in a wide range of solid solution. A small solid solution range for iron and vanadium in chromium trioxide is reported [71, 72], but the XP spectra show no alteration of the surface structure, hence no variation of surface acceptor states has occurred by iron, magnesium, manganese or vanadium doping. As a consequence most of the samples show a similar CO gas response to Cr_2O_3. Apart from CTO, iron doped Cr_2O_3 shows an increased gas response, possibly arising from lower bulk conductivity. As the conductivity of the sensor material is a parallel combination of bulk conductivity (gas insensitive) and surface conductivity (gas sensitive), lowering the bulk conductivity increases the gas sensitive behaviour.

8.5 Summary

Titanium is the only substituent found to modify the surface structure of Cr_2O_3. It has been discovered that chromium iron oxide showed an acceptable gas response to small amounts of carbon monoxide in air at all operation temperatures. This gas response arises from decreased bulk conductivity. At 450 °C it had the highest gas response of all samples. Since chromium iron oxide showed a reduced gas response to water vapour further investigations might be recommended.

9 CO and water gas response of manganese and iron doped chromium titanium oxide

9.1 Introduction

As demonstrated previously chromium titanium oxide showed a good gas response to carbon monoxide and a low response to water vapour. The major reason lies in the fact that surface segregated titanium diminished Cr^{VI} surface acceptor states, resulting in a variation of oxygen species, which determine the gas response. Titanium crystallised in a solid solution with the lattice. Other 3d transition metal elements adjacent to titanium in the periodic table formed impurity phases and caused no change in the surface acceptor concentration. It could be shown that a decline in bulk conductivity could also lead to an increased gas response. In principle a combination of these effects could lead to a development of a better sensor material.

Chromium titanium manganese oxide ($Cr_{2-(x+y)}Ti_xMn_yO_3$) and chromium titanium iron oxide ($Cr_{2-(x+y)}Ti_xFe_yO_3$) were prepared and the gas response was tested. Doping was performed by mixing small amounts of manganese and iron oxide into the chromium titanium oxide. Surface and bulk structure studies were made to determine the difference between these preparations and the unsubstituted chromium titanium oxide. The gas response to CO and water vapour of those doped powders was tested and compared with chromium titanium oxide. The data achieved from those experiments offered interesting perspectives for further gas sensor development.

9.2 Preparation of the powders

Chromium titanium manganese oxide (CTMO) and chromium titanium iron oxide (CTFO) were prepared in the following way. Cr_2O_3 and Fe_2O_3/MnO_2 were dispersed in propan-2-ol, typically 18 gram of Cr_2O_3 powder 0.6 gram of MnO_2 (or 1 gram of Fe_2O_3) and 500 cm^3 propan-2-ol. The required amount of titanium propan-2-oxide solution in propan-2-ol was added under ultrasonic agitation, typically 15 cm^3 titanium propan-2-oxide in 100 cm^3 propan-2-ol. After five minutes 5 cm^3 of water was added. After stirring under ultrasonic agitation for another 15 minutes the solvent was evaporated and the powder was dried at 120°C for two hours. Subsequently the powder was fired in recrystallised alumina crucibles for twelve hours at 1000°C.

9.3 Results

9.3.1 Phase behaviour

Chromium titanium manganese oxide (Figure 9.1) shows the pattern of the Cr_2O_3 corundum structure. However a second phase was discovered with increasing Mn concentration, identified as $MnCr_2O_4$. In this spinel phase Mn^{II} ions are tetrahedrally coordinated by four oxygen atoms and Cr^{III} ions are octahedrally coordinated by six oxygen atoms.

The XRD pattern of chromium titanium iron oxide (Figure 9.2) showed the Cr_2O_3 corundum structure. However, for a iron concentration of 5% the literature reported the existence of a α $(Cr_xFe_{1-x})_2O_3$ phase [72]. XRD identified $(Cr_{0.4}Fe_{0.6})_2O_3$

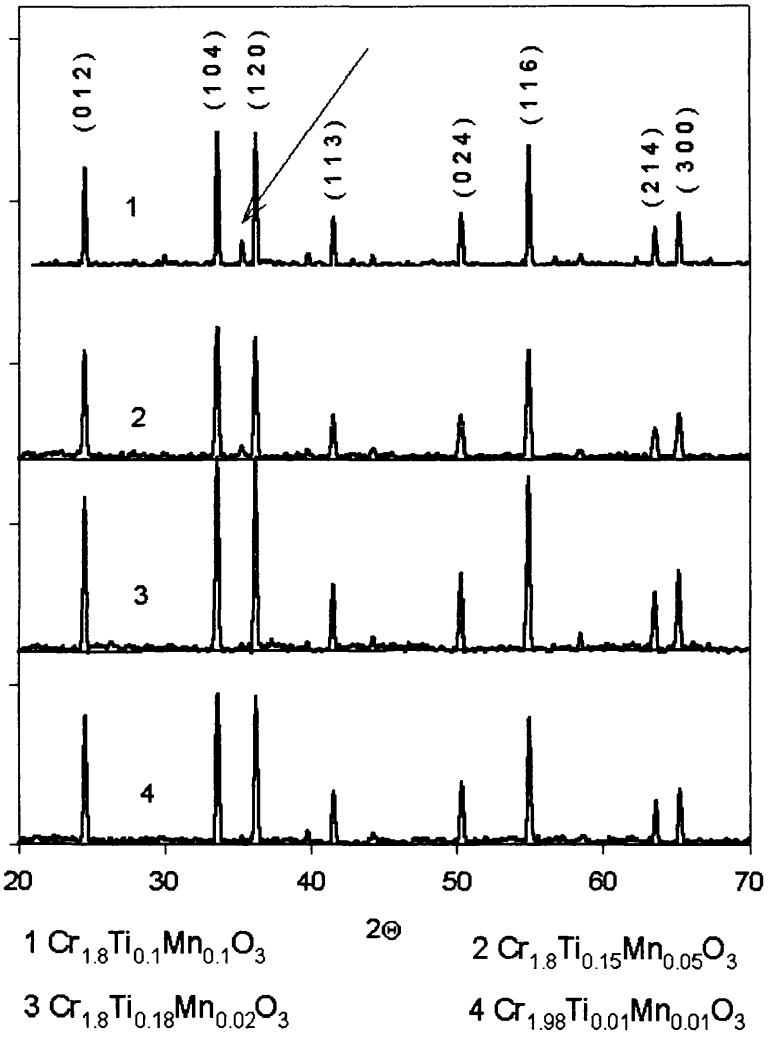

Figure 9.1 X-ray diffraction patterns of $Cr_{2-x-y}Ti_xMn_yO_3$. The signature of the impurity phase is marked by the arrow.

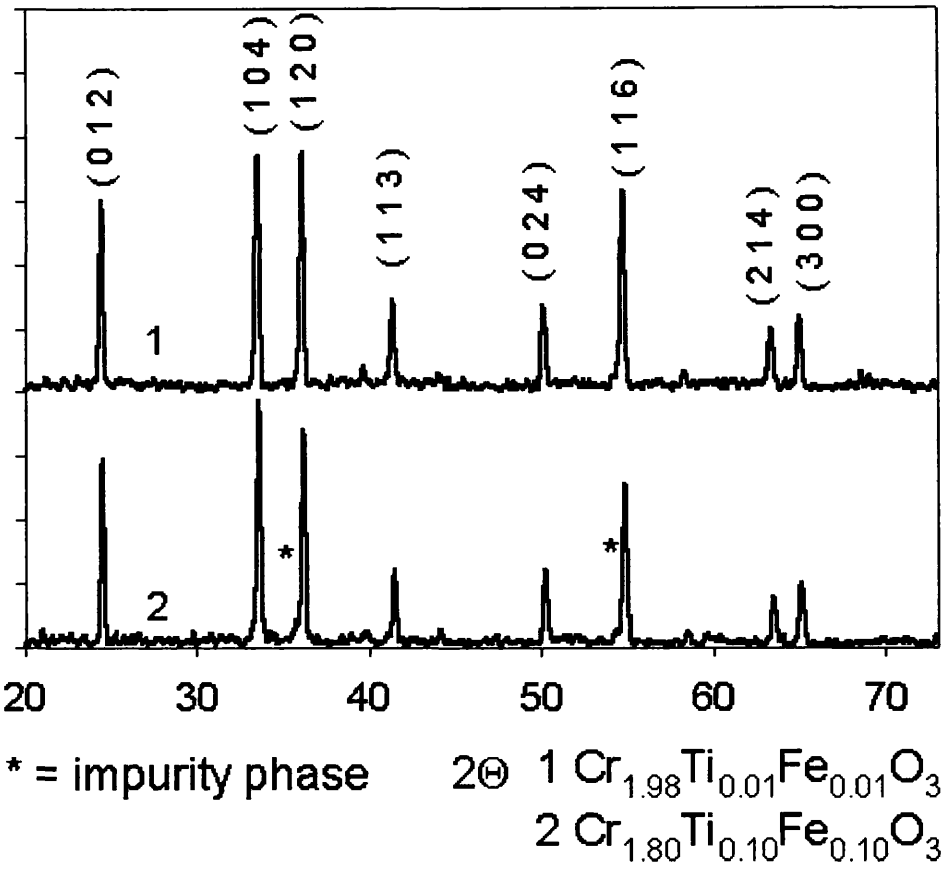

Figure 9.2 X-ray diffraction patterns of $Cr_{2-x-y}Ti_xFe_yO_3$

The impurity phases are marked (*)

XPS analysis of the chromium titanium manganese oxide sample did not show any trace of manganese on the surface. In Figure 9.3 the Cr 2p core peaks of chromium titanium manganese oxide and chromium titanium oxide are compared. Both showed the split $Cr2p_{3/2}$ core peak previously identified as multiplet splitting and the feature at 580 eV binding energy that was identified as Cr^{VI} (see chapter 6). The spectra are almost identical, apart from a slightly enhanced splitting in the manganese-doped sample and a somewhat larger Cr^{VI} signal.

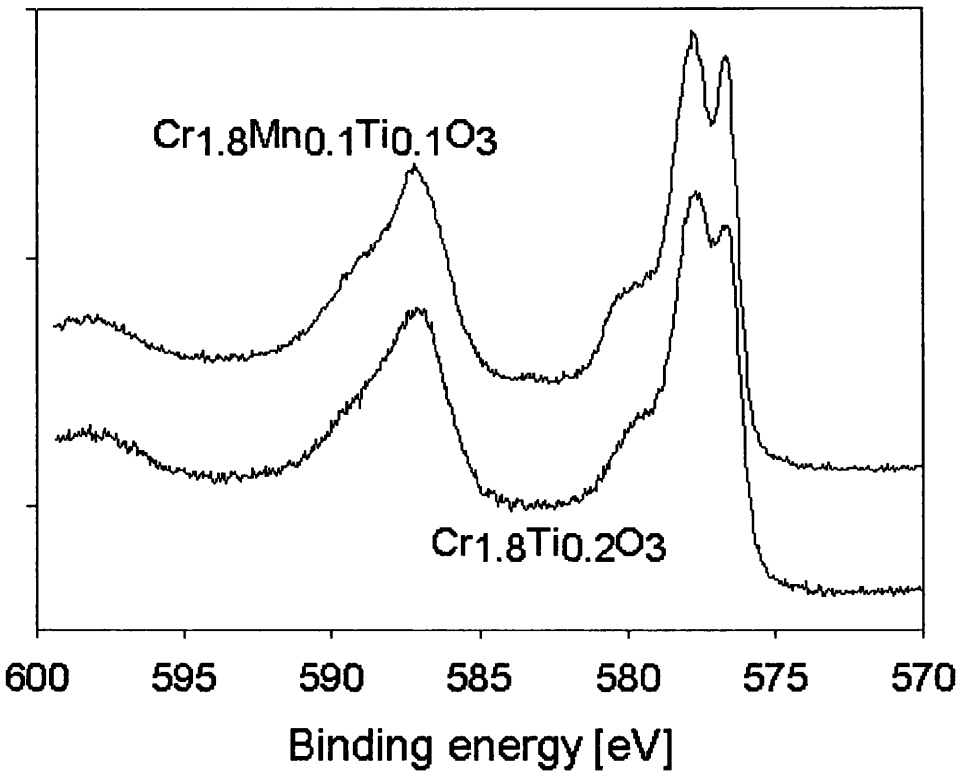

Figure 9.3 XP spectra of the Cr 2p region

The valence band spectra of chromium titanium oxide and chromium titanium manganese oxide are displayed in Figure 9.4. They show the Cr 3d states at 2.5 eV binding energy and the O 2p region between 4 and 6 eV binding energy. Some Cr 3d satellites are visible at 13 eV binding energy. The spectrum of the manganese doped chromium oxide showed the same peaks as chromium titanium oxide but with a change in intensity of features in the O 2p valence band region.

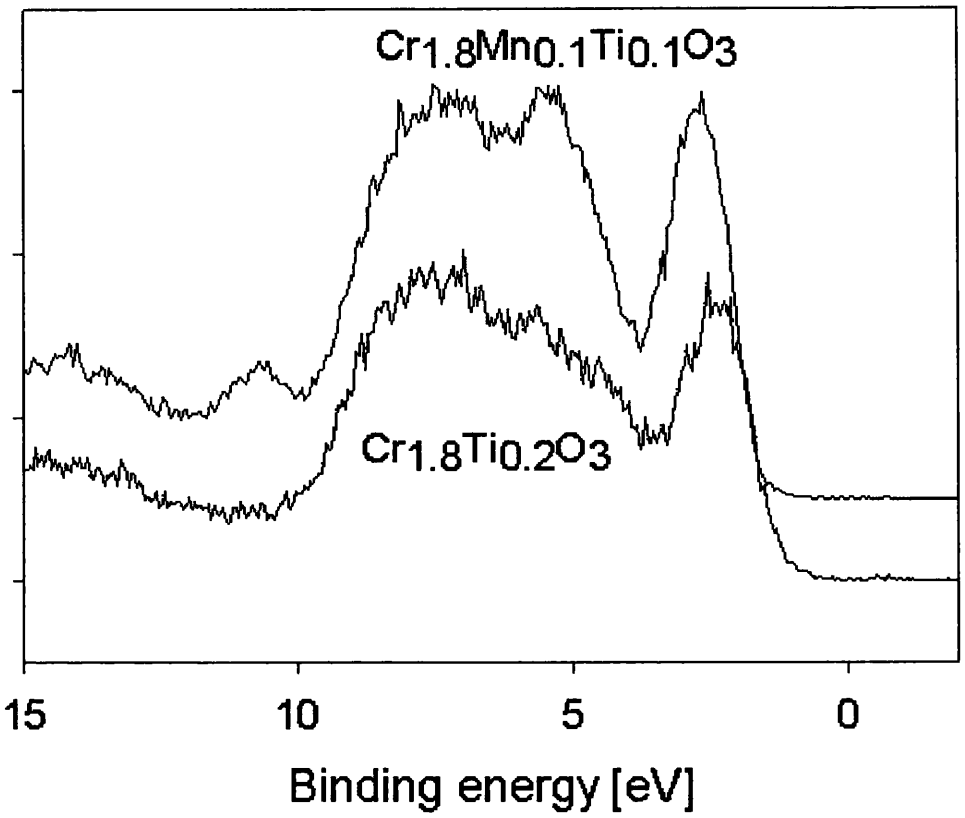

Figure 9.4 Valence band spectra

XP spectroscopy of chromium titanium iron oxide showed large charging effects. The amount of surface enrichment of titanium determined by integration of the peaks is displayed in Table 9.1. The iron and manganese doped samples show a similar titanium surface concentration although less titanium was added during preparation of these samples than for undoped CTO.

Table 9.1 Surface enrichment of defective atoms

Atom	$[Ti]_{bulk}$	$[Ti]_{surface}$
$Cr_{1.8}Ti_{0.2}O_3$	0.2	0.49
$Cr_{1.85}Ti_{0.15}O_3$	0.15	0.54
$Cr_{1.8}Ti_{0.1}Mn_{0.1}O_3$	0.1	0.55
$Cr_{1.8}Ti_{0.1}Fe_{0.1}O_3$	0.1	0.48

A cross–section of a manganese doped chromium titanium oxide pellet was studied by EDAX in order to check the distribution of elements. Figure 9.5 shows a cross – section of a $Cr_{1.8}Ti_{0.1}Mn_{0.1}O_3$ pellet of 1 mm^2 size. The white spots marked by the circles are identified as areas of large Mn enrichment. Imaging experiments of the chromium titanium manganese oxide powder revealed that the $MnCr_2O_4$ impurities form needle shaped crystals with 0.2 μm diameter.

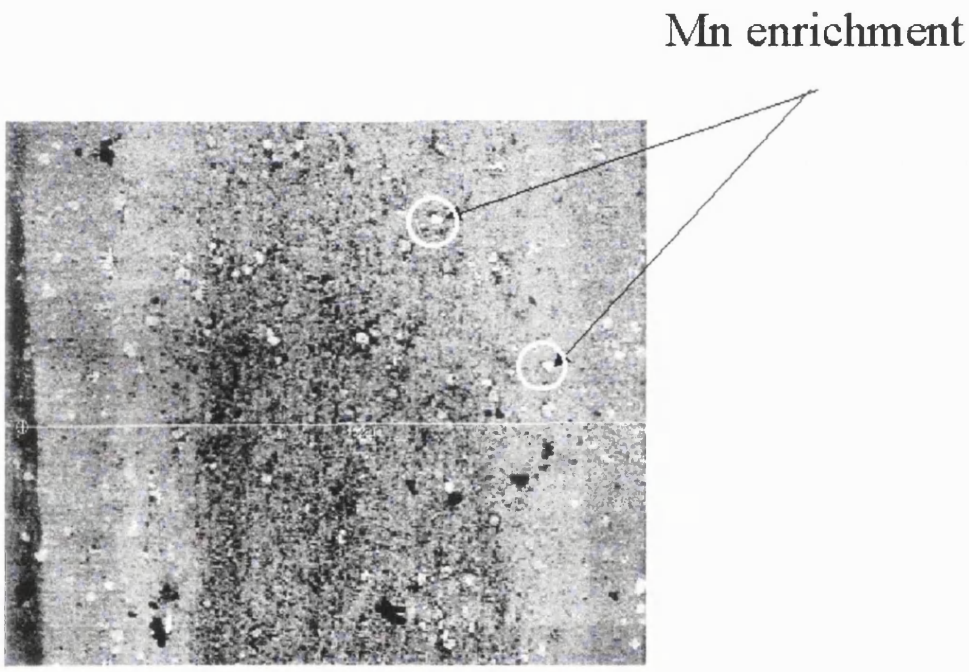

Figure 9.5 Cross section of a chromium titanium manganese oxide pellet

Table 9. 2 Quantitative analysis of the white spots observed

Element	Atom %	Ratio
Ti	0.44	0
Cr	28.28	2
Mn	14.00	1
O	57.29	4

Quantitative analysis of those white spots point to the formula $MnCr_2O_4$ confirming the result derived from X – ray powder diffraction

9.3.2 Gas response experiments

$Cr_{1.8}Ti_{0.1}Mn_{0.1}O_3$ and $Cr_{1.8}Ti_{0.1}Fe_{0.1}O_3$ were tested and compared to $Cr_{1.8}Ti_{0.2}O_3$. The gas response to 500 ppm of CO was determined by using the temperature ramp experiment described earlier. Subsequently the gas response to different concentrations of CO and water vapour was checked. Samples prepared with different amounts of manganese impurities were also investigated. They were characterised by XRD and the CO and water vapour response was checked and compared to $Cr_{1.8}Ti_{0.2}O_3$.

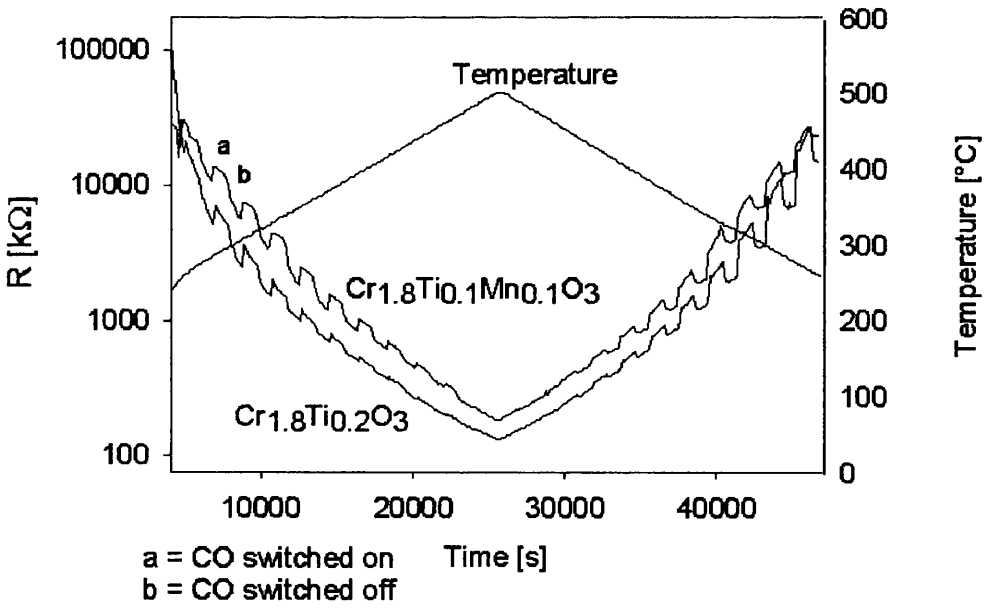

Figure 9.6 Ramp experiment

In Figure 9.6 the resistance and temperature is displayed against time. The experiment was carried out by heating $Cr_{1.8}Ti_{0.2}O_3$ and $Cr_{1.8}Ti_{0.2}Mn_{0.1}O_3$ up to 520°C for six hours and then back to room

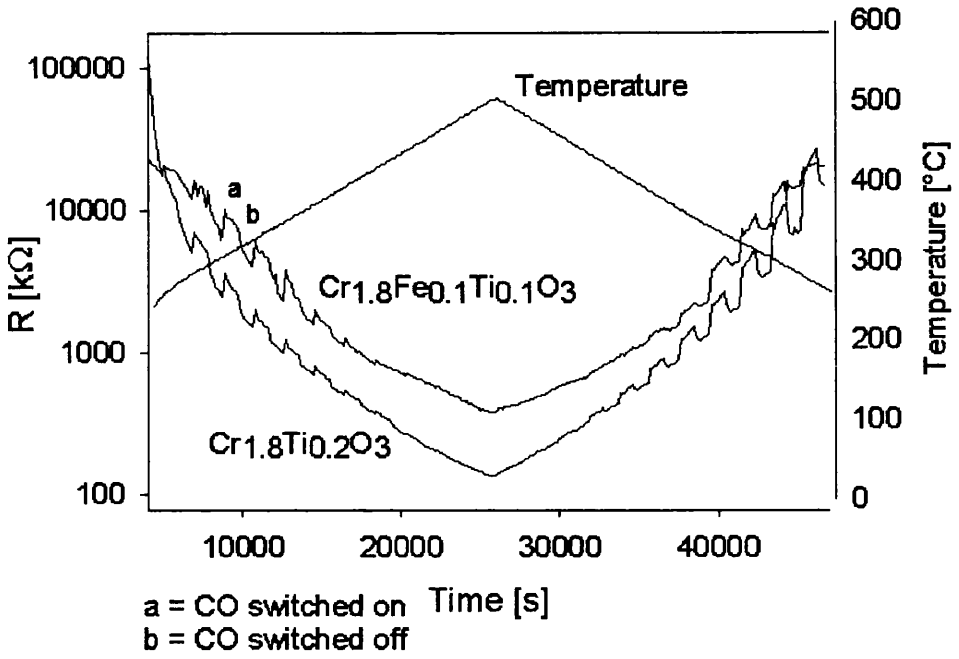

Figure 9.7 Ramp experiment

temperature for the same time. Meanwhile the samples were alternatively exposed to 500 ppm of carbon monoxide. Both materials showed an exponential decrease of resistivity with increasing temperature. The iron and manganese doped chromium titanium oxide showed a slightly higher resistivity than the material without addition of these elements.

The powders had a similar gas response to carbon monoxide. The variation of temperature with the gas response however was different of the different materials. As noted earlier, the gas response of chromium titanium oxide decreased linearly between 250 and 350°C. The maximum gas response was achieved in the second part of the experiment where the temperature was decreasing. This observation can be explained by the loss of water vapour from the surface during the first part of the experiment.

The strong variations of the gas response with temperature were not observed for the manganese doped chromium titanium oxide. Chromium titanium manganese oxide did not show any difference in gas response on both increasing and decreasing temperature.

In the second ramp experiment which was carried out in the same way chromium titanium iron oxide ($Cr_{1.8}Ti_{0.1}Fe_{0.1}O_3$) was tested (Figure 9.7). Chromium iron oxide also showed an increased resistivity in comparison with chromium titanium oxide. In the first part of the ramp experiment it can be observed that at about 350°C upwards the resistivity decrease with temperature was significantly reduced. This might be caused by the loss of water vapour from the surface. Like chromium titanium manganese oxide the gas response of the iron doped chromium titanium oxide had a maximum at 300°C and behaved differently to chromium titanium oxide.

The gas response of chromium titanium oxide decreased with increasing temperature, as seen in Figure 9.8. In the lower temperature region of 250 and 300°C chromium titanium oxide showed the best gas response of the three samples. Chromium titanium manganese oxide however achieved the best gas response between 300 and 350°C. The best gas response at 450°C was achieved by iron doped chromium titanium oxide.

The results of the gas response to water vapour are displayed in Figure 9.10. Neither the iron nor manganese doped chromium titanium oxide samples showed a gas response to water vapour. As a comparison the water vapour response of chromium titanium oxide is displayed as well. The maximum effect was achieved at 300°C. The apparent decrease of signal with further decrease of temperature could have been because the response became slow.

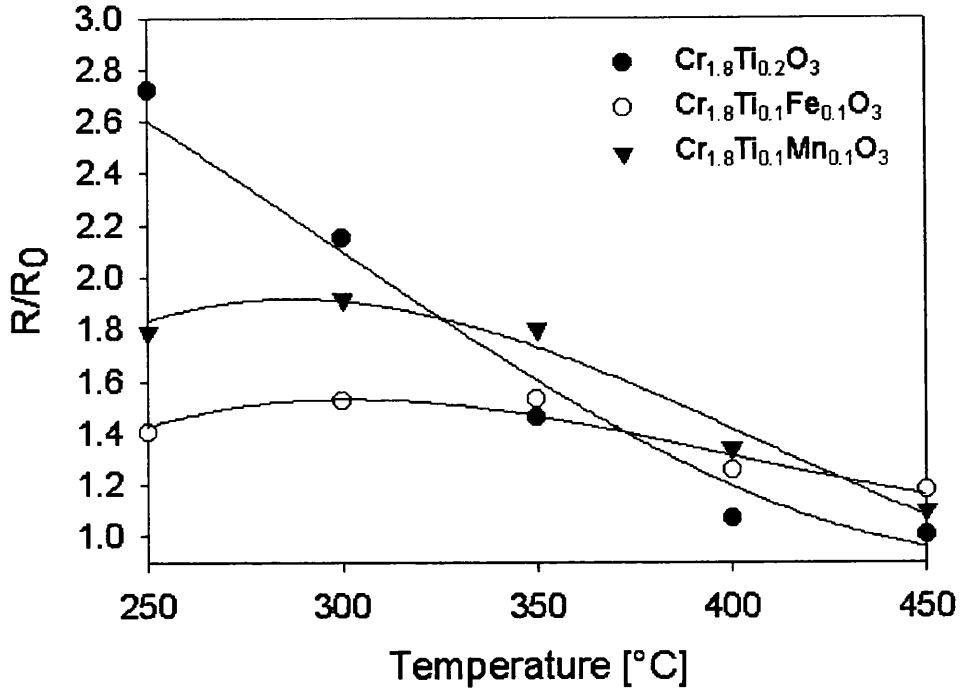

Figure 9.8 Response to 500 ppm of CO

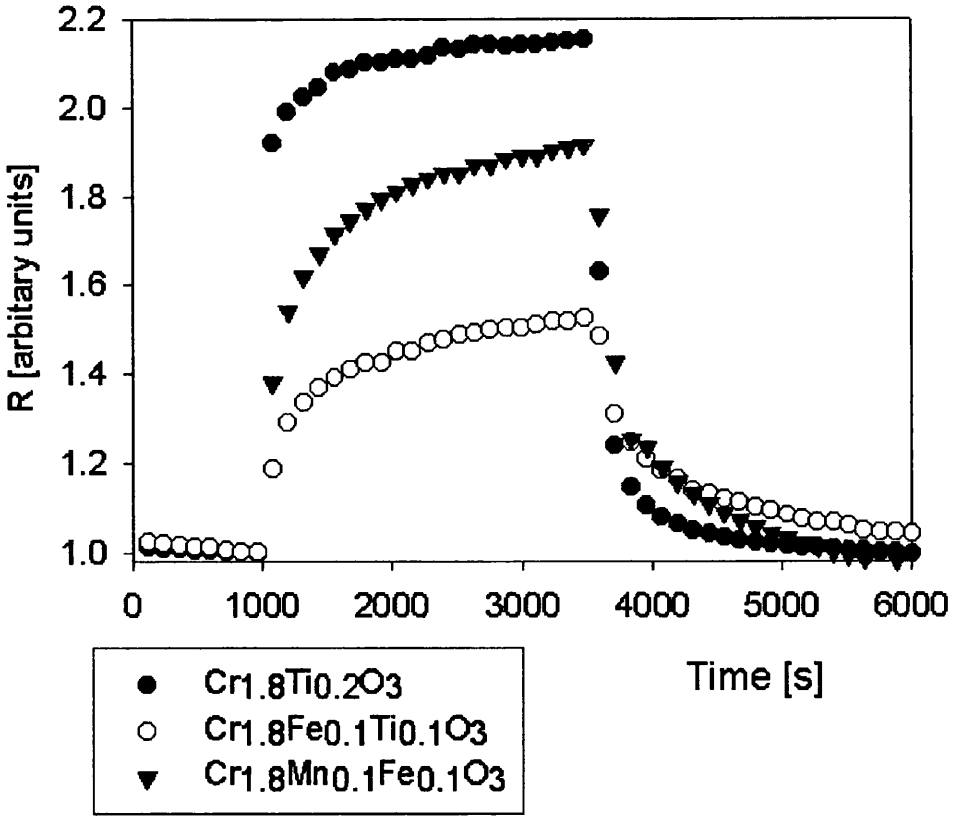

Figure 9.9 CO response at 350°C. Resistance over time

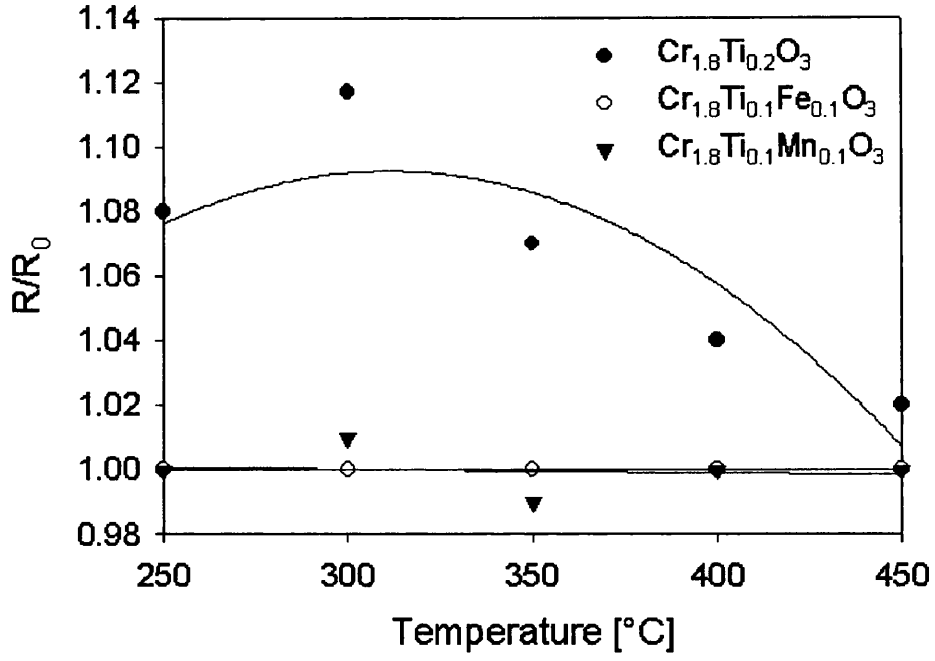

Figure 9.10 Response to 50% relative humidity at RT

The gas response is determined for varying concentrations of carbon monoxide, displayed in Figure 9.9. Both materials show the same square root dependence of the gas response against the concentration of carbon monoxide as was observed for the case of chromium titanium oxide. Hence it is concluded that the mechanism of gas response is not altered by the Mn /Fe dopants.

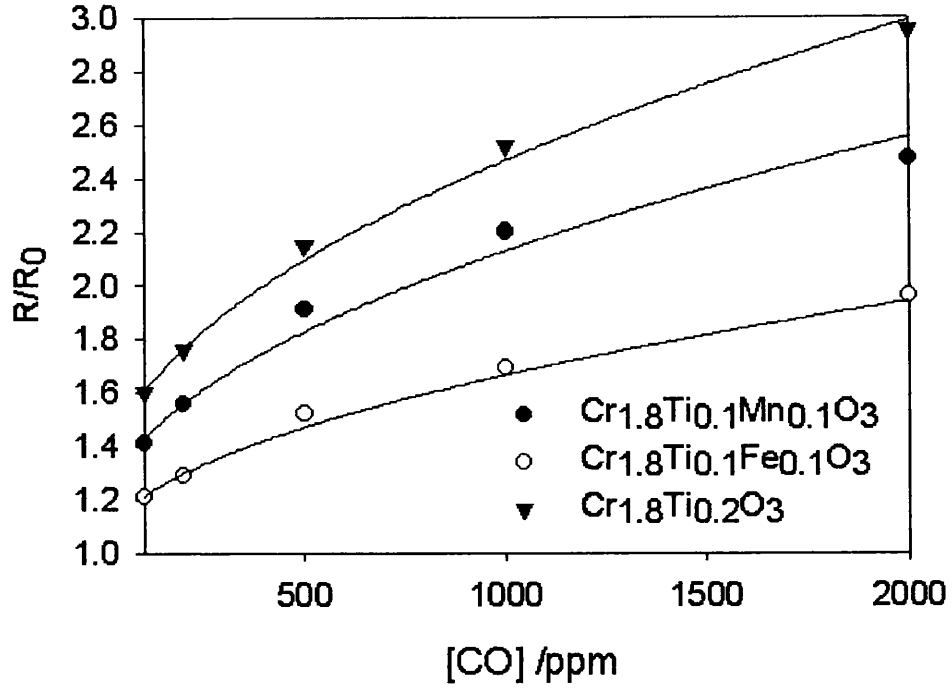

Figure 9.11 Gas response to carbon monoxide at 300°C, The fitted curves are $R/R_0 = 1 + a \quad P\ (CO)^{1/2}$

9.3.3 Variation of manganese and titanium concentration

Manganese and iron doped chromium titanium oxide powders with varying Mn and Ti ratios were prepared. The samples were investigated by XRD, displayed in Figure 9.1. The impurity peaks indicating the presence of $MnCr_2O_4$ were present in all diffraction patterns of the Mn containing samples. The gas response to 500 ppm of carbon monoxide was tested at different operation temperatures. The results are displayed in Figure 9.12 and 9.13.

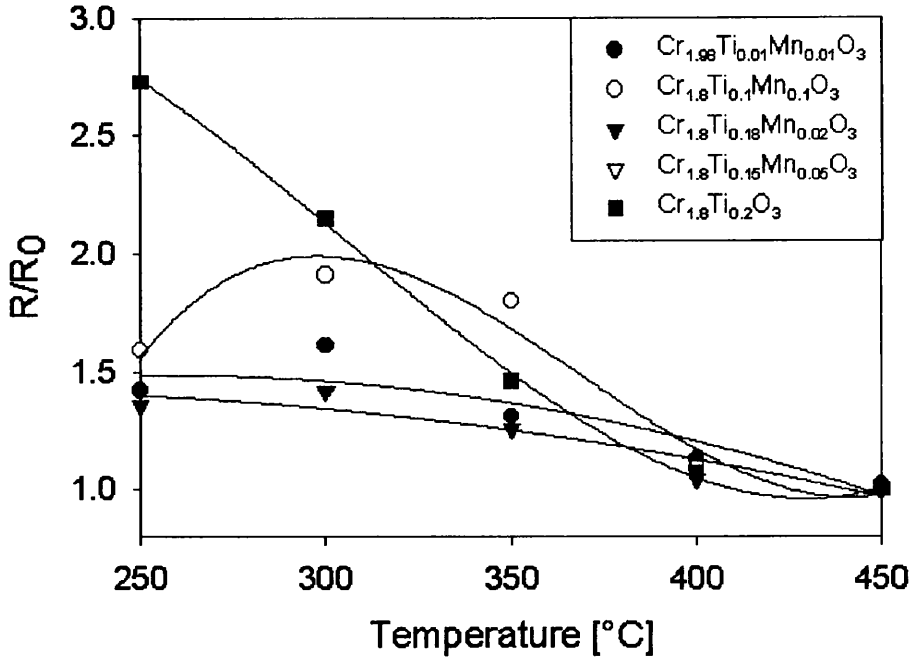

Figure 9.12 Gas response to 500 ppm of carbon monoxide

It can be observed that all manganese doped chromium titanium oxide samples behaved in the same way. A maximum gas response was achieved at 300°C, explained above. The powder compositions to show the best gas responses were $Cr_{1.8}Ti_{0.1}Mn_{0.1}O_3$ and $Cr_{1.8}Ti_{0.15}Mn_{0.05}O_3$. Figure 9.13 shows the gas response of $Cr_{1.8}Fe_{0.1}Ti_{0.1}O_3$ and $Cr_{1.8}Fe_{0.05}Ti_{0.15}O_3$ to 500 ppm of carbon monoxide. Like the manganese doped samples the maximum response to carbon monoxide was determined at 300°C. It is noted that the sample with the highest amount of Fe had the lowest gas response to carbon monoxide.

Chromium titanium manganese oxide was prepared by using much higher amount of manganese. Chromium titanium oxide containing 10% and 20% manganese was tested. It was observed that the resistivity was decreased by a factor of 100. Neither of these samples showed any gas response to CO or water.

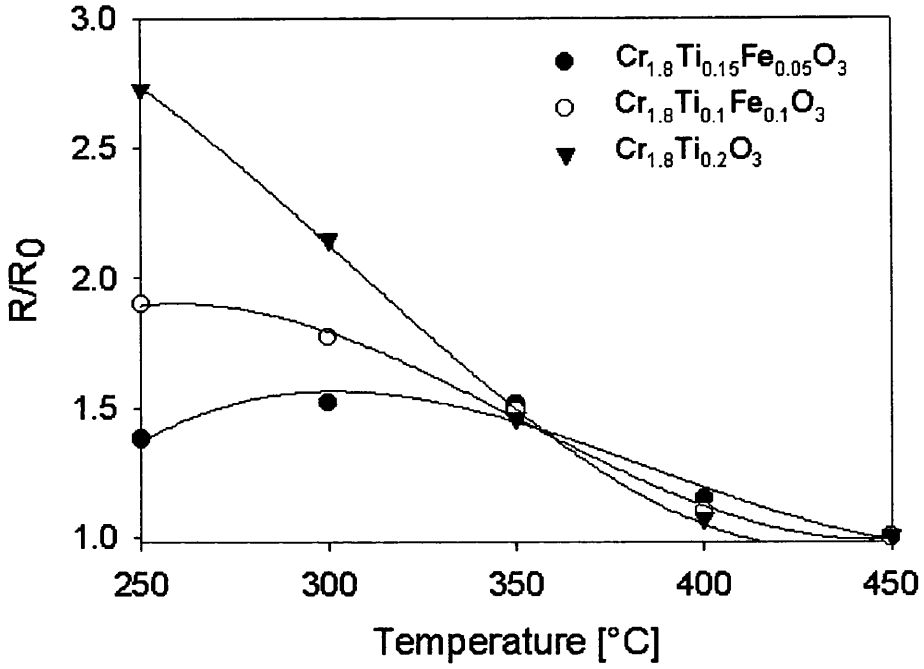

Figure 9.13 Gas response to 500 ppm of carbon monoxide

9.3.4 Gas response of Chromium titanium manganese oxide sensor devices

Sensor devices were fabricated from chromium titanium manganese oxide and compared to sensors fabricated from chromium titanium oxide in which the powders and inks have been made in the same way to minimise as far as possible the effects of variation of microstructure. The gas response to carbon monoxide in wet and dry conditions was tested. The results are displayed in Figure 9.14. The sensors were at first exposed to 50%rh and the gas response to 500 ppm of carbon monoxide was tested. After that the experiment was repeated in dry air. Subsequently the system was switched back to wet air. The results of the experiment described above are listed in Table 9.2

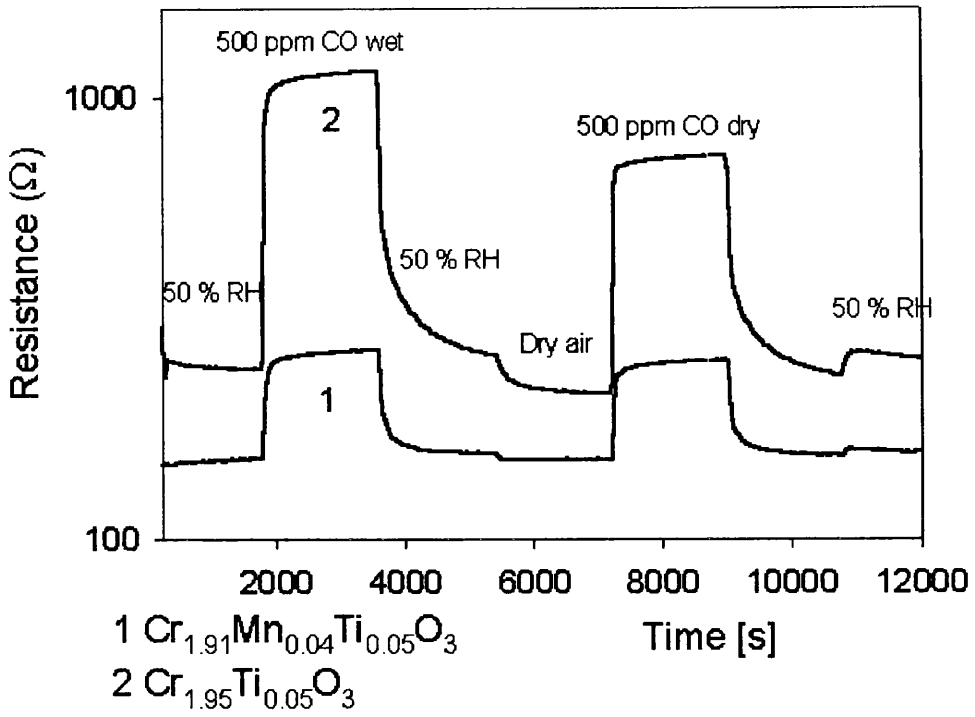

Figure 9.14 CO and H_2O response of sensor devices

Table 9.2 The gas response $S = (R/R_0)-1$ for the different gas sensors

	$S\frac{wetgas}{drygas}$	$S\frac{wetair}{dryair}$	$S\frac{drygas}{dryair}$
$Cr_{1.95}Ti_{0.05}O_3$	0.55	0.14	2.53
$Cr_{1,9}Ti_{0.05}Mn_{0.05}O_3$	0.05	0.01	0.65
Ratio	**10.21**	**10.5**	**3.88**

In the gas sensing experiment $Cr_{1.95}Ti_{0.05}O_3$ had a fourfold increased carbon monoxide gas response to $Cr_{1.91}Ti_{0.05}Mn_{0.04}O_3$ but a tenfold increased humidity response.

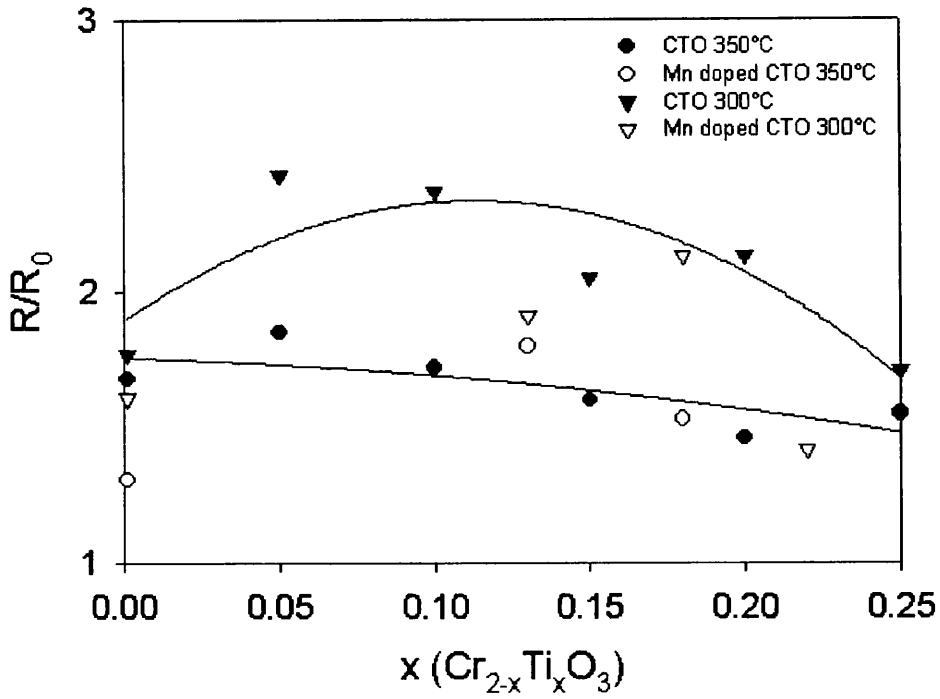

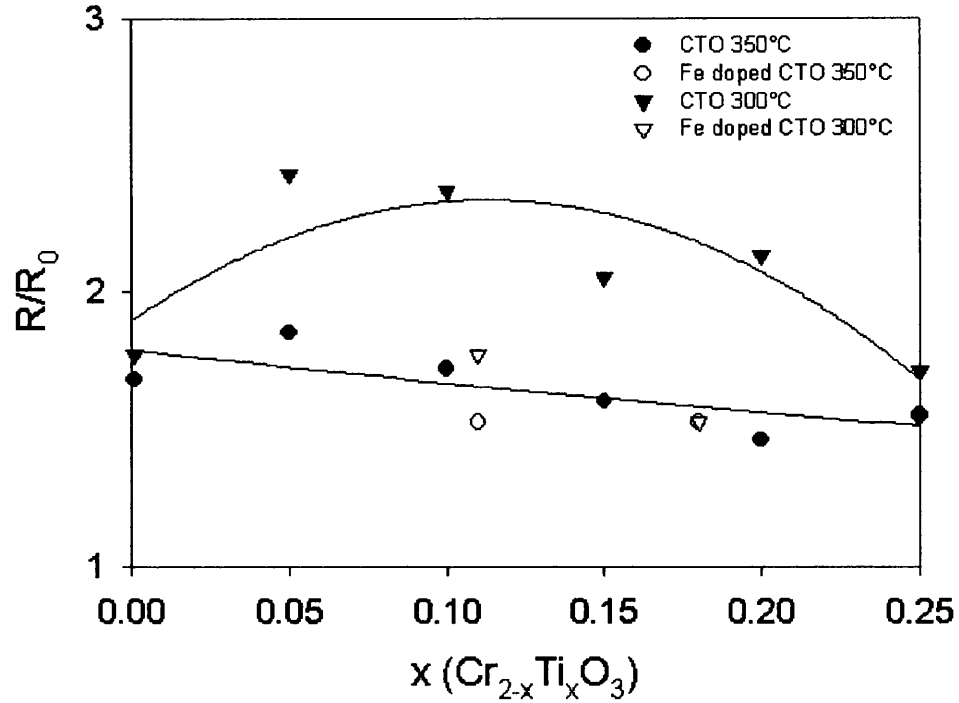

Figure 9.15 + 9.16. CO response at 300°C (filled symbols) and 350°C (unfilled symbols) over titanium bulk concentration.

The amount of titanium in the iron and manganese doped specimen is taken from Table 9.3.

9.4 Discussion

As observed in the experiment dopants of manganese and iron are able to affect the gas responding behaviour of chromium titanium oxide. It was established that Mn doping was able to reduce the water response significantly. Surface investigation confirmed an increased titanium surface concentration. In the bulk $MnCr_2O_4$ was found.

It is believed that due to calcination of the powder the following reaction has occurred.

$$MnO_2 + Cr_2O_3 \longrightarrow MnCr_2O_4 + \tfrac{1}{2} O_2 \quad (9.1)$$

MnO_2 is a good oxidising agent. By reduction of Mn^{4+} to Mn^{2+} molecular oxygen is released. It is noted that in the reaction described above a Mn ion removed 2 Cr ions out of the Cr_2O_3 system. As a consequence the relative amount of titanium in the lattice increased. The real bulk concentration of titanium in the lattice can now be calculated. The true bulk ratio of chromium to titanium can also be inferred from the measured surface composition, using the data for CTO reported in Figure 6.7. Then the gas responses of the appropriate $Cr_{2-x}Ti_xO_3$ could be compared. Figure 9.15 shows a good agreement.

Table 9.3 Corrected Cr to Ti ratio in $Cr_{2-x-y}Ti_xMn_yO_3$ and $Cr_{2-x-y}Ti_xMn_yO_3$

Initial concentration	Cr/Ti ratio from stoichiometry
$Cr_{1.98}Ti_{0.01}Mn_{0.01}O_3$	$Cr_{1.987}Ti_{0.013}O_3$
$Cr_{1.8}Ti_{0.18}Mn_{0.02}O_3$	$Cr_{1.785}Ti_{0.215}O_3$
$Cr_{1.8}Ti_{0.15}Mn_{0.05}O_3$	$Cr_{1.823}Ti_{0.177}O_3$
$Cr_{1.8}Ti_{0.1}Mn_{0.1}O_3$	$Cr_{1.875}Ti_{0.125}O_3$
$Cr_{1.8}Ti_{0.1}Fe_{0.1}O_3$	$Cr_{1.89}Ti_{0.11}O_3$
$Cr_{1.8}Ti_{0.15}Fe_{0.05}O_3$	$Cr_{1.84}Ti_{0.16}O_3$

The same was done for the iron doped CTO, assuming that $(Cr_{0.4}Fe_{0.6})_2O_3$ is formed on the impurity phase (Table 9.3). Figures 9.15 and 9.16 show that the CO response of the substituted materials can be explained in this way.

However, this effect does not explain the very low water vapour response of the manganese and iron doped samples. The effects might have some explanation in some subtle influence of change of microstructure. This and the slower gas response to carbon monoxide (Figure 9.9) indicate a more sintered powder. However, the bulk resistivity is increased. This might be a consequence of the presence of a small volume fraction of resistive impurity phases. It might also be a consequence of a small substitution of the additive into the CTO, also implied by the change in valence band structure and by the changes in the Cr 2p region in XPS. As remarked in the introduction to this chapter, there have been other indications that the binding sites for water vapour are different to those which mediate the response to CO and it intriguing to speculate that the water binding sites have been strongly affected by the small substitution of Fe and Mn into CTO.

9.5 Summary

Small amounts of manganese diminished the CO response and greatly diminished the water vapour response of CTO. A patent for this sensor material is pending. Experiments with pellets also showed a smaller temperature dependence and an increased gas response to carbon monoxide above 350°C. Iron doped CTO showed similar effects. This effect on CO response is attributed to the presence of impurity phases, which could be identified as $MnCr_2O_4$ and $(Fe_{0.6}Cr_{0.4})_2O_3$, which change the Cr:Ti ratio in the CTO. The effect in H_2O response may be due to a very small substitution of Fe or Mn into the CTO lattice.

10 Summary and conclusions

The gas sensing behaviour of $Cr_{2-x}Ti_xO_3$ is controlled by surface segregation of defect clusters. In the absence of Ti, one stable defect is a Cr^{VI} - $V_{Cr}^{///}$ pair, which is surface segregated and contributes to the relatively high conductivity shown by finely porous bodies of Cr_2O_3 at elevated temperature: the empty Cr 3d states act as electron acceptors, giving a p-type conductivity localised near the surface. The surface conductivity is dominated by the acceptor states associated with the high-valency Cr; any effect due to variation of the concentration of surface oxygen states, which is responsible for the gas sensing effect, is insignificant. With Ti addition, a stable defect, again surface segregated, is the complex $Ti^{iv}V_{Cr}^{//}$. The effect of Ti substitution, enhanced by its surface segregation, is to decrease the surface concentration of the high-valency Cr species that is to decrease the acceptor state density in the surface region. This is supported by the computational results, which suggest that the surface segregation of the Ti^{iv} $V_{Cr}^{//}$ complex is more thermodynamically favourable than segregation of the Cr^{VI}-$V_{Cr}^{///}$ defect pair. The consequence is a significant decrease in electrical conductivity, which reveals the effects of variation in surface concentration of oxygen states and hence results in gas-sensitive resistor behaviour. Distortion of the arrangement of surface oxygen above the Cr vacancy creates a potential binding site; the high-valency surface cation creates another. It is suggested that the two sites act in consort to promote the dissociation of oxygen and the surface reaction needed for gas sensing.

The Cr $2p_{3/2}$ states show a multiplet splitting, originating from local magnetic moments at the Cr site. The splitting showed a constant magnitude of about 1 eV for all investigated CTO samples. Distortion of the Cr environment by titanium caused blurring of the peak shape. However, the splitting was restored with further increasing titanium concentration. It is speculated that this is due to ordering of the surface.

The response of CTO to H_2S in nitrogen is considerable. Therefore, this new technique could be successfully applied to the monitoring of H_2S in oil pipes. A consistent and simple description of interaction of H_2S with the surface has been given and related also in some detail to the effect of the gas on the electrical resistivity of the material. The gas response to CO and ethanol varied significantly with oxygen partial pressure: The conductivity in the presence of carbon monoxide was fitted to $P_{(O2)}^{1/2}$. The baseline conductivity varied as $P_{(O2)}^{1/4}$ and the gas response, expressed as the ratio of resistance in the presence or absence of gas at a particular oxygen partial pressure, varied as $P_{(O2)}^{-1/4}$. A model has been developed, based on a reaction scheme given in Chapter 4, which explains the observations.

Titanium is the only substituent found to modify the surface structure of Cr_2O_3. It has been discovered that chromium iron oxide showed an acceptable gas response to small amounts of carbon monoxide in air at all operation temperatures. This gas response arises from decreased bulk conductivity. At 450 °C it had the highest gas response of all samples. Since chromium iron oxide showed a reduced gas response to water vapour further investigations might be recommended.

Small amounts of manganese diminished the CO response and greatly diminished the water vapour response of CTO. A patent for this sensor material is pending. Experiments with pellets also showed smaller temperature dependence and an increased gas response to carbon monoxide above 350°C. Iron doped CTO showed similar effects. This effect on CO response is attributed to the presence of impurity phases, that could be identified as $MnCr_2O_4$ and $(Fe_{0.6}Cr_{0.4})_2O_3$, which change the Cr:Ti ratio in the CTO. The effect in H_2O response may be due to a very small substitution of Fe or Mn into the CTO lattice.

11 References

[1] Penney, D. G., CARBON MONOXIDE TOXICITY, CRC Press, Jun 2000

[2] Brattain, W. H., and Bardeen, J., *Bell Systems Tech J* **32** (1953) 1

[3] Seijama, T., Kato, A., Fukiishi, K., and Nagatini, M., *Anal. Chem.* **34** (1962) 1502

[4] Capteur Sensors Ltd, Didcot, UK: *http://www.capteur.co.uk*

[5] Williams, D. E., *Solid State Gas Sensors*, Ed. Moseley, P. T. and Tofield, B. C., Adam Hilger, Bristol 1987

[6] Yamazoe, A. and Miura, N., *Chemical Sensor Technology, Vol 4'*, Ed Yamauchi, S., Kodansha, Tokyo, 1992

[7] Williams, D. E., and Pratt, K. F. E., *Sens. Actuators B*, **70** (2000) 214

[8] Williams, D. E. and Moseley, P. T., *J. Mater. Chem.*, **1** (1991) 809

[9] Moseley, P.T., and Williams, D. E., *Sens. Actuators B*, **1** (1990) 113

[10] Dawson, D. H., Henshaw, G. S. and Williams, D. E., *Sens. Actuators B*, **26** (1995) 76

[11] Shukri, K., Ph.D. thesis 1999 University College London

[12] Briggs, D. and Seah, M. P., *Practical Surface Analysis* 2nd ed. Volume 1 John Wiley & Sons Chichester 1990

[13] Wagner, C. D., Davis, L. E., Zeller, M. V. J., Al Taylor, R. Raymond, M. and Gale, L. H., *Surface Interface Anal.* **3** (1981) 211

[14] Gay, D. G. and Rohl, A. L., *J Chem Soc Faraday Trans*, **9**(1995) 925

[15] Parry, D. E., *Surf. Sci.*, **49** (1975), 433.

[16] Parry, D. E., *Surf. Sci.*, **54** (1976) 195.

[17] Dick, B. G., Overhauser, A. W. *Phys. Rev.* **112** (1958),90

[18] Gale, J. D., *J. Chem. Soc., Faraday Trans.*, **93** (1997) 629.

[19] Heyes, D. M., Varber, M., and. Clarke, J. H. R., *J. Chem. Soc. Faraday Trans.*, **73** (1977) 1485

[20] Press, W. H., Flannery, B. P., Teukolsky, S. A. and Vetterling, W. T., Numerical Recipes in C, Cambridge University Press, Cambridge, 1988

[21] Slater, B., Catlow, C. R. A., Gay, D. E., Williams, D. E., Dusastre, V. *Journal of Physical Chemistry B*, 10644

[22] Burwell, R. L., Haller, G. L., Taylor, K. C. and Read, J. F., *Adv Catal*, **20** (1969) 1

[23] Zecchina, A., Coluccia, S., Cerruti, L. and Borello, E., *J. Phys. Chem.* **75**, (1971) 2783

[24] Grzybowska, B., Grabowski, J. S¡oczynski, R., Wcis¡o, K., Koz¡owska, A., Stoch, J., and Zielinski, J., *J. Catal.*, (1998) 687

[25] Grzybowska, B., Grabowski, J., S¡oczynski, R., Wcis¡o, K., Koz¡owska, A. and Stoch, J., *Polish J. Chem.*, **72** (1998), 2159.

[26] Callister, W. D., Johnson, M. L, Butlaer, I. B. and Ure, R. W., Jr. *Journal of The American Ceramic Society* **62** (1979) 208

[27] Mars, P. and van Krevelen, D. W., *Chem Eng Sci*, **3** (1954) 41

[28] Over, H., Kim, Y. D., Seitsonen, A. P., Wendt S., Lundgren E., Schmid, M., Varga, P., Morgante, A. and Ertl, G., *Science*, **287** (2000) 1474

[29] Vedrine, J. C., Millet, J. M. M., and Volta, J.C., *Catal. Today* **32** (1996) 115

[30] Slater, B., Catlow, C. R. A., Williams, D. E. and Stoneham, A. M., *J Chem Soc Chem. Comm.* (2000) 1235

[31] Zaki, M. I., Hasan, M. A., Fouad, N. E., *Applied Catalysis A*, **171**(1998) 315

[32] Scarano, D., Zecchina, A., Bordiga, S., Ricchiardi, G. and Spoto, G. *Chem. Phys.* **177** (1993) 547

[33] Freund, H. J., *Angew. Chem. Int. Ed. Engl.* **36** (1997) 452

[34] Hemmerich, I., Rohr, F., Seifert, O., Dillmann, B., Freund, H.J., *Z. Phys. Chem.* **202** (1997) 31

[35] York, S. C., Abee, M. W., Cox, D. F., *Surf.Sci.* **437** (1999) 386

[36] Lawrence, P.J., and Parker, S.C., *J. Am. Cer. Soc.*, **71** (1988) C-389

[37] Grimes, R. W., *J. Am Ceram Soc.*, **71**(1994) 378

[38] Gale, J.D. *Chem Soc., Faraday Trans.*, **93** (1997) ,629

[39] Battle, P. D., Gibb, T. C., Nixon, S., Harrison,W. T. A., *Journal of Solid state Chem.* **75** (1988) 21

[40] Barker C.M., submitted

[41] Parasevka, T. Master thesis University College London 1999.

[42] Andersson, S., Sundholm, A. and Magneli, A., *Acta Chem. Scand.* **13** (1959) 989

[43] Somiya, S., Hirano, S. and Kamiya, A., *J Solid State Chem*, **25** (1978) 273

[44] McHale, A. E., (Ed) *Phase Diagrams for Ceramists*, Annual '91, National Institute for Standards and Technology, US Department of Commerce

[45] Henshaw, G.S., Dawson, D. H. and Williams, D. E., *J Mater. Chem.*, **5** (1995) 1791

[46] Jayaraman, V., Gnanasekar, K. I., Prabhu, E., Gnanasekaran, T. and Periaswami. G., *Sens Actuators B*, **55** (1999) 175

[47] Oyama, T., Imura, Y., Ishii, T. and Takeuchi, K., *Nippon Kagaku Kaishi*, 7 (1993) 825

[48] Holt, A. and Kofstad. P., *Solid State Ionics*, **117** (1999) 21

[49] Holt, A. and Kofstad, P., *Solid State Ionics*, **69** (1994) 127

[50] Holt, A. and Kofstad, P., *Solid State Ionics*, **69** (1994) 137

[51] Chabanis, G., Parkin, I. P. and Williams, D. E., *J. Mater. Chem.* **11** (2001) 1651

[52] Beattie, I. R. and Gilson, T. R., *J Chem Soc A*, (1969) 2322

[53] Campbell, J. A., Spectrochim Acta, **21** (1965) 1333

[54] Campbell, J. A., Spectrochim Acta, **21,** (1965) 851

[55] Smith, P., *Capteur Sensors Ltd.* Private Communication

[56] Williams, D. E. and Pratt, K. F. E., *J. Chem. Soc. Faraday Trans.*, **4** (1998) 3493

[57] Ikemoto, I., Ishii, K., Kinoshita, S., Kuroda, H., Alario Franco, M. A. and Thomas, J.M., *J. Sol. State Chem.* **17**, (1976) 425

[58] Allen, G. C. and Tucker, P. M., *Inorg. Chim. Acta* **16** (1976) 41

[59] Veal, B. W. and Paulikas, A. P., *Phys. Rev. B* **31**, (1985) 5399

[60] Rao, C. N. R. Sarma, D.D. Vasudevan, S. and Hegde, M. S., *Proc. R. Sot. Lond. A* **367** (1979) 239

[61] Tsurkan, V., Plogmann, S., Demeter, M., Hartmann, D., and Neumann, M., *Eur. Phys. J. B* **15** (2000) 401

[62] Frost, D. C, Mc Dowel C. A., and Woolsey, I. S., *Chem. Phys. Letters* **17** (1973) 320

[63] Plogmann, S., Schlatholter, T., Braun, J., Neumann, M., Yarmoshenko, Y. M., Yablonskikh, M. V., Shreder, E. I., Kurmaev, E. Z., Wrona A., Slebarski A., *Phys. Rev. B* **60** (1999) 6428

[64] Salvi, A. M., Desimonia E, Watts J F and Castleb J. E., *Applied Surface science **90*** (1995) 333

[65] Wagner, C. D., Davis, L. E., Zeller, M. V. J., Taylor, A., Raymond R. M. and Gale, L.H., *Surface Interface Anal.* **3** (1981) 211

[66] Stypula, B., Stoch, J., *Corrosion Science,* **36** (1994) 2159.

[67] Kaltsoyannis, N., Private communication

[68] Battaile, C. C., Najafabadi, R. and Srolovitz, D. J., *J. Amer. Ceram. Soc.*, **78** (1995) 3195

[69] Windishmann, H. and Mark, P., *J Electrochem. Soc* **126** (1979) 627

[70] Dusastre, V, Williams, D. E., *J. Phys. Chem. B,* **102** (1998) 6732

[71] Robinson, W. R., *Acta Crystallographica B* **24** (1986) 1985

[72] Music, S., Lenglet, M., Popovic, S., Hannoyer, B., Czako Nagy, I., Ristic, M., Balzar, D., Gashi, F., *J. Mater. Sci.* **(31)** (1996) 4067